nature portfolio

Peer Review File

Imaging-Guided Companion Diagnostics in Radiotherapy by Monitoring APE1 Activity with Afterglow and MRI Imaging

Reviewers' Comments:

Reviewer #1:
Remarks to the Author:
This manuscript reports an apurinic/apyrimidinic endonuclease 1 (APE1)-activated afterglow/MRI probe (APE1-probe) which consists of DNA modified ultrabright afterglow nanoparticles and ultrasmall FeMnOx nanoparticles. As a dual contrast agent for afterglow imaging and MRI, APE1-probe provides dynamic and sensitive imaging of APE1 activity with the LOD: 0.0092 U/mL in afterglow imaging and 0.16 U/mL in MRI. By monitoring APE1 levels, APE1-probe enable the evaluation of radio-resistance, providing early prediction of radiotherapy outcome, allowing for timely adjustments to treatment schemes. Moreover, APE1-probe demonstrated the potential to evaluate radiation-induced liver injury and accurately identify injury locations within the liver. Furthermore, the study demonstrated the capability of APE1-probe to detect radiation-induced bystander effects by imaging APE1 levels in neighboring non-irradiated tumors. The probe successfully visualized APE1 upregulation in non-irradiated tumors through MRI imaging, providing valuable insights into bystander effect and its potential for synergistic therapies. Overall, this article is well written, with experimental results supporting the author's claims. Therefore, I recommend the publication of this article after addressing the following minor issues.
1. The tumor cells intrinsically express APE1, is it an ideal biomarker for imaging or evaluation of the therapeutic resistance or outcome of radiotherapy? Please discuss this point.
2. For afterglow luminescence in vitro and in vivo, the author used white light source with a power density of 1 W/cm2, whether this power density was too high? Does the author optimize the afterglow luminescence with other power densities?
3. In figure caption, the authors should specify more details about test conditions, such as the concentrations of nanoparticles, laser irradiation conditions. There are two 25 in Figure 1c.
4. Are the NPs colloidally (such as TA NPs-DNA1, FeMnOx-DNA2 and APE1-probe) stable in buffer or serum medium over the time? In addition, more characterizations of FeMnOx can be added, such as XRD, XPS, HR-TEM or mapping.
5. For the afterglow performance of TA NPs such as brightness, emission wavelength, half-life, it will be better to list a table to compare with all previously reported organic afterglow agents. Some relevant and recent literatures about organic afterglow probes should be cited in the table or text.
6. The afterglow spectrum of TA NPs, core-satellite probe before and after APE1 activation can be supplemented.
7. What is the quenching efficiency after assembly of TA and FeMnOx? Can the nanoparticles recover the afterglow luminescence similar to TA NPs in saturated APE1?
8. Please provide un-cropped WB of Fig. 3n.
9. As illustrated in Fig. 6 and 7, the author evaluated that radiation-induced liver injury and upregulated APE1 by afterglow and MRI. However, the author should provide additional data to demonstrate liver injury with increased of radiation except for H&E staining, such as biochemical analysis.
Based on the limited therapy efficiency in Figure 5h, why the authors choose 6 Gy as the highest radiation dose?

Reviewer #2:
Remarks to the Author:
In this manuscript, the authors used APE1 as a potential biomarker for monitoring radiotherapy. They developed a core-satellite probe for imaging the activity of APE1 in living mice using afterglow luminescence and MRI imaging. The combination of MRI and afterglow of APE1-probe could offer both anatomical and functional imaging, enabling precise identification of APE1 location in deep-seated tissues. The authors demonstrated that the probe enables the monitoring of APE1 levels in living mice and the evaluation of radio-resistance and radiation-induced liver injury, providing early prediction of radiotherapy outcome. Overall, this work is interesting. Some concerns need to be addressed before publication.

(1) In previous work, spatially selective monitoring of subcellular APE1 dynamics in response to mitochondria-targeted photodynamic therapy has been reported, which indicated APE1 could be used as an indicator for real-time evaluation of PDT efficacy. This should be discussed in the Introduction with related reference cited.
(2) The author emphasized the symptoms of liver injury could overlap with those of other liver diseases. In fact, the up-regulation of APE1 amount is also present in these diseases, such as hepatitis. How do the probes distinguish radiation-induced liver injury from other liver diseases? Although the author provided a good correlation between radiation dose, ROS generation, DNA damage level, and APE1 level in the liver, the association between APE1 activity and liver injury is lacking.
(3) In Fig. 7f, anti-APE1 was used to corroborate whether APE1 levels in the liver increase in a radiation dose dependent manner. The results showed APE1 levels in the cytoplasm appeared to increase in a radiation dose-dependent manner. Since APE1 is primarily residing in the nucleus of cells, why was there no nuclear signal of APE1 in liver slice incubated with anti-APE1 antibodies?
(4) In the core-satellite nanoprobe, how many FeMnOx particles are assembled on the TA NPs?
(5) Aside from the afterglow/MRI measurements, gel shift experiment is essential to directly validate the responses of probes towards APE1.
(6) In Fig. 2d, the author claimed the limit of detection calculated by the probes was lower than most fluorescence probes used for APE1 detection. However, when calculating the detection limit, a lower concentration should be selected, not within the detection range (0-4 U/ml).
(7) Before the in vivo experiments, it is essential to evaluate the stability of the probes in serum. In addition, biodistribution study should be provided.
(8) In Fig.8, the probes could detect the upregulation of APE1 in tumors adjacent to radiation-treated tumors. To further confirm this result, the APE1 level in the non-irradiated left tumor should be testing via conventional immunohistofluorescence technique.
(9) In Fig. 3j, error bars are incomplete.

Reviewer #3:
Remarks to the Author:
The manuscript "Imaging-Guided Companion Diagnostics in Personalized Radiotherapy: Monitoring APE1 Activity with Afterglow and MRI Imaging" by Yue et al is an attempt to investigate the potential of the APE1-activated afterglow/MRI probe as a companion diagnostics tool for personalized radiotherapy. Even though, the study is well designed, it need to address following comments/queries:

Scientific Comments/Queries
1. Abstract, line 32: "…correlation of afterglow and MRI signals with APE1 expression, radiation dose, intratumor ROS" whether radiation dose delivered decided?
2. Abstract, line 36, "Moreover, MRI imaging evaluates the radiation-induced bystander effect," how?
3. Some of the terminologies like 'ultra-small' and 'ultrabright', is there any basis to use ultra as the size of NP and fluorescence signal appears to be within the range of any other study.
4. Introduction, line 74, "Until now, there have been rare reports on imaging APE1 activity in living animals (Table 2)." The major findings of these studies especially related to Cy5 fluorescence should be mentioned.
5. Scheme 1. APE activation, scheme is not able to clearly indicate how activation takes place and after activation how the structure of NP changes? It is not clear. Too much information is mentioned. The different aspects should be put in boxes to not getting mixed up.
6. Table 2, what is meaning of limits of detection and detection range. The conc mentioned shows what? Whether per mL blood or ?. These aspects need to be mentioned in Figure legend.
7. Introduction, line 85-87, "APE1 in deep-seated tissues in living animals for the first time and significantly boosted the afterglow imaging of APE1 detection range (0 - 4 U/mL) and detection sensitivity (limit of detection: 0.0092 U/mL)". At one place it is mentioned in deep seated tissue

and on the other hand detection limit in per mL. What is meaning of conc in which solution, blood or?
8. Introduction, line 91-95, "In this study, we designed ultra-small manganese-doped iron oxide nanoparticles (FeMnOx) as dual contrast agents in both T1 and T2 MRI models (31, 32), significantly amplifying the signal dynamic ranges, detection range, and detection sensitivity (limit of detection: 0.16 U/mL) for APE1 for the first time." The linkage of MRI, NP and APE 1 detection is not clear.
9. Introduction, line 106, how the APE1 cleavage is done, what enzyme and what happens to APE before and after is not clear. How, APE1 function and cleavage would be affected by radiation, DNA damage or ROS generation should be described.
10. Introduction, line 110, "APE1-responsive afterglow/MRI probe" concept should be elaborated for better understanding of as DNA damage sensor model.
11. Introduction, line 118, name of tumor model should be provided.
12. Fig 1a is not clear and confusing. Showing irradiation at both sides with almost similar information is confusing. Only one side scheme should be better. In Figure legend should be self-explanatory rather than to refer to manuscript text. Same way Fig 2a scheme is also confusing. What is cleaving agent for MRI? A separate scheme for better clarity for cleavage and after flow effects (Fig. 1a, Fig 2a) should be included.
13. For TEM and DLS size are with in same range of 32 nm. Ideally hydrodynamic size is generally bigger if some conjugation or coating is done? Authors should clarify the same.
14. A quantification of recycle of on/off at different cycle (Supp Fig 8) should be included to know the magnitude of effect of recycle.
15. A quantification of Supp Fig 17 should be included.
16. Line 227, why 12.5:1 ratio was chosen in Suppl Fig 17, signal is not visible. A rationale of selecting ratio should be mentioned in the text
17. Line 271, the significance and p value for detection limit should be mentioned out of multiple experiments
18. Fig 3j, cell number used is too high 0.5-2x107. Why so high concentration of cells was used? That shows poor sensitivity of materials in the cells. How much is the uptake and what is the uptake kinetics? The normal cell data should be also provided for comparison. Why there is increase with respect of cell number, where it is due to background signal. From control to irradiated, increase seems to be not statistically significant. Statistical significance should be provided. Same comment is applicable for Fig 3m
19. Fig 3o, statistical significance should be provided.
20. Without statistical significance, statement (line 394-395) "Especially, at cell number of 2 × 107, the afterglow signal intensity was increased by 2.0-fold for 6 Gray, 1.6-fold for 4 Gray, and 1.3-fold for 2 Gray, compared to 0 Gray." has no meaning.
21. A time kinetics for afterflow effect and expression of APE1 in HeLa cells after irradiation should be shown.
22. What is difference between Fig 4b and Fig 4c. Even Figure legend it is not clear.
23. For sham irradiated (0 Gy) targeting and non-targeting with or without AS1411 aptamer data provided for not for irradiated (Fig 4e,f,g). Non-targeted for irradiated groups should be also provided.
24. For APE1-activated afterglow/MRI imaging for cancer cells experiments, whether cells were collected by trypsinization? A data with or without washing should be shown.
25. A time kinetics of update of NP in cells and suitable control should be shown
26. How radiation treatment was given, which irradiator type of radiation, energy and dose rate should be mentioned. For local irradiation whether any shielding devise was used.
27. MEHPPV-based nanoparticles were used for comparison of formulation. What the rationale to select the same.
28. How the synthesis of NPs and conjugation of bonds at different steps were characterized?
29. Suppl Fig 17, quantification of images should be done and graphically represented. Whether Fig 1p is quantification of Suppl Fig 17. The ratio values shown in Suppl figure is different than Fig 1p. Clarify
30. Suppl Fig 23 Scheme the structure formed after programmed self-assembly is confusing. It is

not clear from structure that APE site is from TA-NPs-DNA1 or Fe2x-DNA2.
31. Results and discussion, line 244-247, What is basis of statement, is exp done or based on previous study ".. use of FeMnOx allows for an inverse change in contrast, facilitating the subtraction of the T1 MRI and T2 MRI intensity signal and providing larger dynamic ranges, compared to the use of iron oxide nanoparticles (FeOx)." Fig. 2a is scheme, however statement appears to stating result. " As a result, the sensitivity of the system was greatly enlarged, as depicted in Fig. 2a".
32. Suppl Fig 35, 36, statistical significance should be shown.
33. Line 529-530 and 569, the data shown Fig 5 is basically effect of radiation on afterglow effect and other parameters. Unless individual animals are monitored for these parameters and correlated with tumor growth and need of radiation dose needed, it is difficult to state its role in personalized dose description. It is too much claim!
34. Bystander effects are referred interaction from irradiated cells to neighboring cells. Since, in present study, effect was observed in distant tumors, which is systemic abscopal effect (Manuela et al, IJRB, Int J Radiat Biol. 2023;99(6):964-982. doi: 10.1080/09553002.2022.2078006). Hence, abscopal could be better terminology than bystander in the present manuscript. How much % of shielding was obtained compared to directly irradiated tumors.
35. In both tumor bearing legs after glow effect and its kinetics should be also monitored after radiation?
36. Conclusions should be limited to observations made in the study. Most of the points like personalized medicine, biomarker etc are too tall claim with respect to observations made.

Editorial Comments
1. Since all data in liver, in title Liver should be mentioned.
2. Abstract Table 2 mentioned. Not needed
3. Abstract full form of LOD
4. Table 2, 9, reference ACS Nano, 17,13792−13810 (2023) could not be found. Check the reference again.
5. Table 1 legend, 'tool' should be changed to 'studies'
6. Table legends should be more descriptive to cover major aspects of Table.
7. Fig 2 I inset image looks like blurred to show core and shell. A clearer image should be shown.
8. Line 285-286, facilitated to reduction should be facilitated to reduce
9. Line 287, The should be changed to the
10. Line 389 and many other places, Hela should be HeLa
11. Many places, liver organs mentioned, what it means, it is should be only liver.
12. Some places Gray is written as gray should be corrected.

Response Letter (NCOMMS-23-55361)

Reviewer #1:

This manuscript reports an apurinic/apyrimidinic endonuclease 1 (APE1)-activated afterglow/MRI probe (APE1-probe), which consists of DNA modified ultrabright afterglow nanoparticles and ultrasmall FeMnOx nanoparticles. As a dual contrast agent for afterglow imaging and MRI, APE1-probe provides dynamic and sensitive imaging of APE1 activity with the LOD: 0.0092 U/mL in afterglow imaging and 0.16 U/mL in MRI. By monitoring APE1 levels, APE1-probe enable the evaluation of radio-resistance, providing early prediction of radiotherapy outcome, allowing for timely adjustments to treatment schemes. Moreover, APE1-probe demonstrated the potential to evaluate radiation-induced liver injury and accurately identify injury locations within the liver. Furthermore, the study demonstrated the capability of APE1-probe to detect radiation-induced bystander effects by imaging APE1 levels in neighboring nonirradiated tumors. The probe successfully visualized APE1 upregulation in nonirradiated tumors through MRI imaging, providing valuable insights into bystander effect and its potential for synergistic therapies. Overall, this article is well written, with experimental results supporting the author's claims. Therefore, I recommend the publication of this article after addressing the following minor issues.

Response: Thank you for your thorough review and constructive comments on our manuscript. We are honored by your recommendation for publication and have taken great care to address the minor issues you've raised. The manuscript has been meticulously revised to incorporate your suggestions, which we believe have substantially improved the clarity and quality of our work. We are confident that these modifications have enhanced the manuscript and look forward to the improved version serving the scientific community.

1)*. The tumor cells intrinsically express APE1, is it an ideal biomarker for imaging or evaluation of the therapeutic resistance or outcome of radiotherapy? Please discuss this point.*

Response: We are grateful for your insightful inquiry about the potential of APE1 as a biomarker for both imaging and the assessment of therapeutic resistance or radiotherapy outcomes.

APE1's endogenous expression in tumor cells indeed plays a pivotal role in the repair of DNA damage induced by radiation through the base excision repair (BER) pathway. This intrinsic activity is a key contributor to the cellular response to radiotherapy, functioning both in the direct repair of DNA and as a modulator of the cellular redox state, affecting transcriptional regulation. These dual roles of APE1 are critical in influencing the radioresistant phenotype of tumor cells.

The correlation between elevated APE1 expression or activity and increased radioresistance has been extensively documented in pre-clinical studies. For example, research has shown that APE1 levels are augmented following irradiation and that attenuating APE1 expression through RNA interference can enhance the radiosensitivity of pancreatic cancer cells (*Cancer Biother. Radiopharm.* **2013**, 28, 169-76). APE1's ability to inhibit radiation-induced pyroptosis, particularly in lung adenocarcinoma, further exemplifies its role in conferring radioresistance (*Transl. Oncol.* **2023**, 36,101749). Moreover, APE1's enzymatic activity is predictive of radiotherapy outcomes, as seen in studies on pediatric ependymomas (*Int. J. Cancer.* **2011**, 129, 2370-9), and its contribution to the radioresistant nature of medulloblastoma cells has also been noted (*Clin. Cancer Res.* **2005**, 11, 7405–7414).

Based on this evidence, APE1 not only emerges as a valuable prognostic marker for cancer but also as a strategic target for gauging therapeutic resistance and forecasting radiotherapy outcomes. Our development of an APE1-activated afterglow/MRI probe harnesses the predictive power of this biomarker, enabling dynamic and precise imaging. This novel imaging tool has the potential to revolutionize the monitoring of radiotherapy efficacy, allowing for the fine-tuning of treatment plans and ultimately enhancing therapeutic outcomes.

2). *For afterglow luminescence in vitro and in vivo, the author used white light source with a power density of 1 W/cm^2, whether this power density was too high? Does the author optimize the afterglow luminescence with other power densities?*

Response: Thank you for bringing this to our attention. Upon reviewing our manuscript, we realized that there was an inadvertent error in the reported power density of the white light source; it is indeed 10 mW/cm^2, not 1 W/cm^2 as previously stated. We appreciate your vigilance in pointing out this discrepancy.

Prior to finalizing the conditions used in our experiments, we conducted an extensive optimization study to understand the relationship between various power densities and the resultant afterglow luminescence. We exposed our theranostic afterglow nanoparticles (TA NPs) at a concentration of 5 μg/mL to a range of power densities: 60 μW/cm^2, 5 − 27 mW/cm^2. Each exposure lasted for 10 seconds, followed by the measurement of the afterglow luminescence signal over a 60-second acquisition time.

The results, which are presented in **Supplementary Fig.6** of the supplementary materials, indicate that the TA NPs emitted a noticeable afterglow luminescence even at the ultra-low power density of 60 μW/cm^2. This finding highlights the exceptional brightness of our nanoparticles. Moreover, as we increased the power density, we observed a corresponding enhancement in the afterglow signal, confirming the scalability of luminescence with increasing energy input.

We have corrected the power density value in our manuscript and included the detailed findings of the optimization study to provide a comprehensive understanding of the afterglow luminescence characteristics of our TA NPs. We trust that these amendments address your concerns and improve the accuracy of our study.

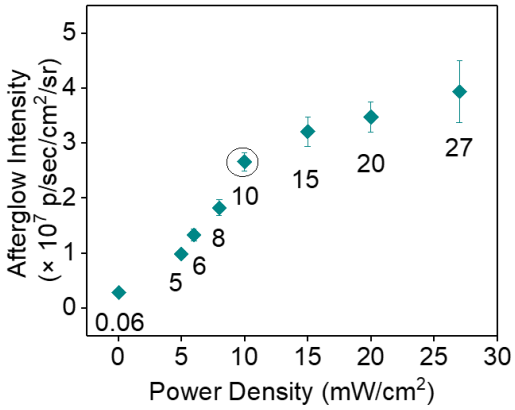

Supplementary Fig.6 Afterglow luminescence signal intensity of TA NPs (5 μg/mL) under different-power density irradiation (irradiation time: 10 s, acquisition time: 60 s, n = 6). Data are means ± SD

Related experimental methods:

Optimization of the afterglow luminescence with different irradiation power densities. To determine the power density of white light to activate TA NPs luminescence, we irradiated TA NPs (5 μg/mL) solution with various power densities (0.06, 5, 6, 8, 10, 15, 20, and 27 mW/cm^2, respectively) for 10 s, and immediately captured the afterglow signal with an acquisition time of 60 seconds using the IVIS Spectrum imaging system (Lumina XR) without excitation.

3)*. In figure caption, the authors should specify more details about test conditions, such as the concentrations of nanoparticles, laser irradiation conditions. There are two 25 in Figure 1c.*

Response: Thank you for your attentive observation regarding the information provided in the figure caption. In response to your comment, we have amended the figure captions to offer more comprehensive details about the experimental conditions. Specifically, we have included the concentrations of nanoparticles used in the experiments, the power density of the white light source, the duration of laser irradiation, and the acquisition time of the afterglow luminescence measurements. These additions are now clearly stated in the figure captions within both the main text and the supporting information, with the modifications distinctly outlined to facilitate easy identification.

Revised figure legends were as follows:

Fig. 1 Preparation and characterization of TA NPs-$FeMnO_x$ assembly (APE1-probe). a Schematic illustration for afterglow luminescent mechanisms of TA NPs and preparation of APE1-probe. b TEM images of TA NPs. c, d Afterglow images and signal attenuation of TA NPs after irradiation (30 μg/mL, n = 3). e, f Afterglow images and signal intensity of TA PNs under 10-recycle recharge (30 μg/mL, n = 6). g, h Afterglow images and signal intensity of TA NPs nanoparticle and MEHPPV-based nanoparticle (n = 3). i TEM images of $FeMnO_x$. j, k MRI images and signal intensity of various concentrations of FeMnOx@BHQ_3-N_3 (n = 3). l TEM images of TA NPs-$FeMnO_x$ assembly (APE1-probe). m Overlap of TA NPs-DNA1's afterglow luminescence spectrum and BHQ_3's absorption spectrum. n Schematic illustration for the afterglow resonance energy transfer (ARET) between TA NPs donor and BHQ_3 quencher. o Afterglow images and signal intensity of TA NPs-DNA1(20 μg/mL, n = 6) before and after assembling with $FeMnO_x$-DNA2. p Afterglow signal intensity of TA NPs-DNA1 (10 μg/mL, n = 6) assembling with various ratio of $FeMnO_x$-DNA2. All afterglow imaging were obtained with white light irradiation (10 mW/cm^2) time of 10 s and acquisition time of 60 s.

Fig. 2 APE1-activated afterglow and MRI in APE1-probe solution. a Scheme illustration for APE1-activated TA NPs-$FeMnO_x$ assembly (APE1-probe) for afterglow and MRI contrast comparison between TA NPs-Fe_3O_4 and TA NPs-$FeMnO_x$ (APE1-probe). b Hydrodynamic size distribution of APE1-probe before and after incubation with APE1 (10 U/mL). c − e Afterglow imaging of APE1-probe after incubating with various concentrations of APE1 (0 - 10 U/mL) (containing 5 μg/mL TA NPs, n = 6). c Afterglow images. d A near-liner curve between the afterglow signal and APE1 concentration. e Signal-to-noise ratio of afterglow signal. f – l Relaxation time and MRI measurement of APE1-probe (containing 5 μg/mL TA NPs, n = 3) treated with various concentrations of APE1. (f) $1/T_1$ and $1/T_2$ values. g T_1 MRI and T_2 MRI images. h Quantified T1 and T_2 MRI signal intensity from (g). i Relaxation time mapping images of different concentrations of APE1-probe before and after APE1 (10 U/mL) incubation. j MRI signal range (ΔT_1, ΔT_2, and ΔT_1 - ΔT_2 value) of APE1-probe treated with various concentrations of APE1. k Correlated curve between ΔT_1 - ΔT_2 value and APE1 concentration. l Corresponding limit of detection under MRI signal ranges from (j). m – o MRI images and quantification of TA NPs-FeOx treated with various concentration s of APE1(0 − 4 U/mL) (containing 5 μg/mL TA NPs, n = 3). m T_1 MRI and T_2 MRI images. n Quantified T_1 and T_2 MRI signals from (m). o ΔT_1 - ΔT_2 value calculated from (n). All afterglow imaging were obtained with white light irradiation (10 mW/cm^2) time of 10 s and an acquisition time of 60 s. Data are means ± SD. Statistical differences were analyzed by student's t test, *p<0.05, **p<0.01, ***p<0.001.

Fig. 3 APE1-activated afterglow/MRI imaging for monitoring radiation dose-dependent APE1 expression in cancer cells. a Scheme illustration and DNA sequences of irresponsive probe (APE1-ir-probe, no contain AP sites) and responsive probe (APE1-probe, containing AP sites). b, c APE1-ir-probe (containing 5 μg/mL TA NPs) incubated with APE1 (10 U/mL) or not (n = 6). b Afterglow images and quantified signal intensity. c T_1 and T_2 MRI images (n = 3). d Quantified MRI signal intensity from (c). e − g The HeLa cells incubated with APE1-ir-probe, APE1-probe, and APE1 inhibitor/APE1-probe respectively, for afterglow/ MRI imaging (4×10^7 cells/mL, n = 3). e Afterglow images and signal intensity. f T_1 and T_2 MRI images. g Quantified T_1 and T_2 MRI signal intensity. h Scheme illustration of dual-mode afterglow/MRI for monitoring radiation dose-dependent APE1 activity. i − m A various number of HeLa cells treated with various radiation doses (0, 2, 4, and 6 grays) and then incubated with APE1-probe, for afterglow/MRI imaging (n = 3). i Afterglow images. j Afterglow signal intensity. k T_1 MRI images. l T_2 MRI images. m Subtracted MRI signal intensity (ΔT_1 - ΔT_2 value). n, o Western bolting determination and quantified APE1 level of the HeLa cells at post-treatment of 2 hours under various radiation doses (n = 2). All afterglow imaging were obtained with white light irradiation (10 mW/cm^2) time of 10 s and acquisition time of 60 s. Data are means ± SD. Statistical differences were analyzed by student's t test, *p<0.05, **p<0.01, ***p<0.001.

Fig. 4 Afterglow/MRI imaging for monitoring radiation dose-dependent APE1 in tumor in vivo. a Scheme illustration of tumor-targeted imaging of APE1-probe (containing tumor-targeted AS1411 aptamer) or imaging of APE1-probe (no targeting, uncontaining AS1411 aptamer), and radiation dose-dependent afterglow/MRI imaging in vivo. b Afterglow imaging of mice i.v. injected with APE1-probe (no targeting) (n = 3). c Fluorescence images of mice i.v. injected with APE1-probe (no targeting) (n = 3). d − g Afterglow images of the mice treated with various doses of radiation (0 – 6 grays) and then intravenously injected with APE1-probe (n = 3). h Quantified afterglow signal intensity. i Signal-to-noise ratio of afterglow imaging and fluorescence imaging of the mice intravenously injected with APE1-probe (no targeting). j T_1 and T_2 MRI images of the mice intravenously injected with APE1-probe (no targeting) (n = 3). k – q The mice were treated with various radiation doses (0 - 6 gray) and then i.v. injecting APE1-probe

for afterglow and MRI imaging (n = 3). k – n T_1 and T_2 MRI images. o, p Quantified T_1 and T_2 MRI signal intensity from (j – n). q Subtracted ΔT_1 - ΔT_2 value of MRI signal intensity (ΔT_1: subtracted T_1 signal; ΔT_2: subtracted T_2 signal). r Scheme illustration and L&T-ESI images of mice with 6 gray radiation treatment and APE1-probe injection. s signal-to-noise ratio comparison of MRI images before or after L&T-ESI treatment. t, u L&T-ESI images and quantification of tumor with various radiation dose treatment. v, w L&T-ESI images and quantification of mice with 6 grays of radiation dose treatment at different time points. All afterglow imaging were obtained with white light irradiation (10 mW/cm^2) time of 10 s and acquisition time of 60 s. Fluorescence imaging was obtained with excitation wavelength of 605 nm and emission of Cy5.5 channel. Data are means ± SD. Statistical differences were analyzed by student's t test, *p<0.05, **p<0.01, ***p<0.001.

Fig. 5 Afterglow/MRI imaging for early prediction of tumor radiotherapy effects. a Scheme illustration. b – g Fluorescence confocal images and signal intensity for immunofluorescence of tumors slice with treatment various radiation does (0 – 6 gray) (n = 4 slice × 10). b, c Tumor slice staining with DCFH-DA for testing ROS yield. d, e Tumor slice incubating with H_2AX antibody and Cy3-labeled IgG for testing DNA damage (n = 4 slice × 10). f, g Tumor slice incubating with anti-APE antibody and Cy3-labeled IgG for testing APE1 level (n = 4 slice × 10). h, i Nude mic bearing subcutaneous HeLa xenograft tumors with various radiotherapy doses during the 12 days of observation (n = 5). h Tumor growth curves. i Tumor weight. j, k Representative images of H&E-stained and tunnel immunofluorescence of tumor slice treated with various radiotherapy doses. l Correlation between radiotherapy and afterglow/MRI signal intensity for early prediction of therapeutic outcome. Data are means ± SD. Statistical differences were analyzed by student's t test, *p<0.05, **p<0.01, ***p<0.001.

Fig. 6 Afterglow/MRI for evaluating radiation-induced liver organ injury. a Scheme illustration for APE1-activated afterglow/MRI imaging for evaluating radiation-induced liver injury. b − i Liver region of mice was treated with various radiation dose (0 − 6 grays), and then injected with APE1-probe (n = 3). b, c Afterglow luminescence images and increased signal intensity. d, e Afterglow images and signal intensity of in-vitro liver organ after injection of APE1-probe for 8 hours (n = 3). f T_1 MRI and T_2 MRI images of liver region of mice treated with various radiation dose (0 − 6 grays) (n = 3). g, h Increased T_1 MRI intensity and decreased T_2 MRI intensity. i Subtracted MRI signal intensity (ΔT_1 - ΔT_2 value). j L&T-SEI images of the liver region with various radiation treatment (at 2-hour post-monitoring). k Quantified signal intensity of L&T-SEI images (ΔT_1 - ΔT_2 value), data from (j). All afterglow imaging were obtained with white light irradiation (10 mW/cm^2) time of 10 s and an acquisition time of 60 s. Data are means ± SD. Statistical differences were analyzed by student's t test, *p<0.05, **p<0.01, ***p<0.001.

Fig. 7 Determination of radiation-induced liver organ injury. a Scheme illustration for APE1-activated afterglow/MRI imaging for evaluating radiation-induced liver organ injury. b, c Liver slice staining with DCFH-DA for testing ROS yield (n = 4 slices × 10). d, e liver slice incubating with H_2AX antibody and Cy3-labeled IgG for testing DNA damage (n = 4 slices × 10). f, g Liver organ slice incubating with anti-APE antibody and Cy3-labeled IgG for testing APE1 level (n = 4 slices × 10). h − k H&E staining analysis of liver treated with various radiation dose (0 − 6 grays) (n = 4 slices × 10). l Correlation between radiate on does, afterglow/MRI signal intensity, ROS generation, DNA damage level and APE1 level. Data are means ± SD. Statistical differences were analyzed by student's t test, ***p<0.001.

Fig. 8 Subtracted MRI imaging for evaluating radiation-induced abscopal effect. a Scheme illustration. b Scheme illustration of the Group 1 mice with radiation treatment only in right tumor and then intravenous injection of APE1-probe. c Scheme illustration of the Group 2 mice with intravenous injection of APE1-probe. d MRI images of the Group 1 mice with radiation treatment only in right tumor and then intravenous injection of APE1-probe (n = 3). e Increased T_1 MRI intensity and decreased T_2 MRI intensity for Group 1. f MRI images of the Group 2 mice with intravenous injection of APE1-probe (n = 3). g Increased T_1 MRI intensity and decreased T_2 MRI intensity for Group 2. h ΔT_1 - ΔT_2 signal value from (e and g). i L&T-SEI images from Group 1 and Group 2 at 2-hour post-monitoring. j Signal-to-noise ratio from (i). Data are means ± SD. Statistical differences were analyzed by student's t test, *p<0.05, **p<0.01, ***p<0.001.

Moreover, we have corrected the typographical error in **Fig.1c**. The duplicative "25" was a mistake, and we have updated this to "30" to accurately reflect the data presented. We appreciate your diligence in detecting these issues, and we trust that the revisions have enhanced the clarity and accuracy of our manuscript.

4). *Are the NPs colloidally (such as TA NPs-DNA1, FeMnOx-DNA2 and APE1-probe) stable in buffer or serum medium over the time. In addition, more characterizations of FeMnOx can be added, such as XRD, XPS, HR-TEM or mapping.*

Response: Thanks for your suggestion! Thank you for inquiring about the colloidal stability of our nanoparticles (NPs), including TA NPs-DNA1, $FeMnO_x$-DNA2, and APE1-probe, in various media. We have conducted thorough stability tests to assess the colloidal behavior of the NPs in different environments. The NPs were dispersed in DPBS, 1× Nebuffer, DMEM, and 10% serum (v/v) and were left to stand at room temperature for time points of 0, 2, 4, 6, and 12 hours. After each time interval, the hydrodynamic sizes of the NPs were measured using dynamic light scattering (DLS). The data, which are presented in **Supplementary Fig. 10c**, **14c, and 16c**, demonstrate that the NPs maintained consistent size profiles throughout the duration of the experiments across all tested media. The absence of significant size variation suggests that the TA NPs-DNA1, $FeMnO_x$-DNA2, and APE1-probe exhibit excellent colloidal stability in DPBS, 1× Nebuffer, DMEM, and serum over the observed time period.

We believe this stability is an indicator of the robustness of our NPs, making them suitable for further experimental applications where they could be exposed to a variety of biological environments.

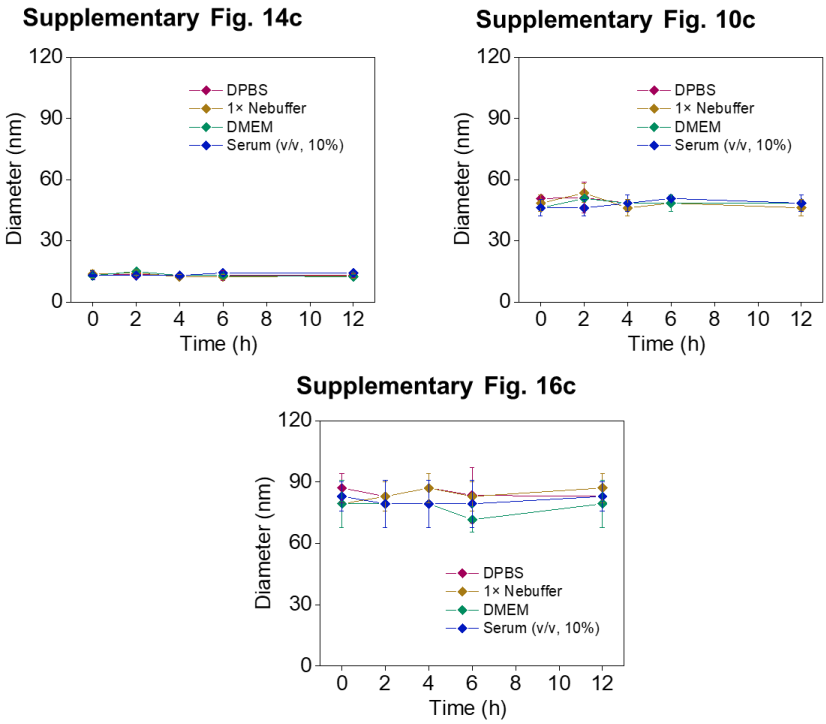

Supplementary Fig. 14c DLS measurement of $FeMnO_x$-DNA2 at different conditions (n = 3). **Supplementary Fig. 10c** DLS measurement of TA NPs-DNA1 at different conditions (n = 3). **Supplementary Fig. 16c**. DLS measurement of APE1-probe at different condition (n = 3). Data are means ± SD

Related experimental methods:

Determination of the stability of nanoparticles. To determine the stability of $FeMnO_x$-DNA2, TA NPs-DNA1 and APE1-probe, as-prepared $FeMnO_x$-DNA2, (0.1 mg/mL, Fe + Mn) TA NPs-DNA1 (containing 5μg/mL TA NPs) was incubated in 120 uL of different conditions (DPBS, 1 × NeBuffer, DMEM, and Serum (v_{serum}/V_{H2O}, 1:9), respectively) for different times (0, 2, 4, 6, and 12 hours, respectively), and then determined their DLS size using a Zetasizer Nano ZS90 (Malvern) with a 90° scattering angle and a He-Ne laser.

In addition, for characterizing and verifying as-synthesized $FeMnO_x$ nanoparticle, we analyzed the structure of $FeMnO_x$ using powder X-Ray Diffraction (XRD) patterns. From **Supplementary Fig.12b**, several obvious diffraction peaks can be showed and consistent with the peak position, in comparison with the standards (JCPDS 10-0319 for $MnFe_2O_4$), indicating the successful synthesis of manganese-doping iron oxide nanoparticle ($FeMnO_x$). Moreover, we determined the X-ray photoelectron spectroscopy (XPS) of the $FeMnO_x$, and the results showed the core level binding energies at 711.6 and 724.7 eV attributing to the characteristic doublets of Fe 2p3/2 and Fe 2p1/2 of Fe^{3+}, as well as the binding energies at 641.8 and 653.7 eV attributing to the characteristic doublets of Mn 2p3/2 and Mn 2p1/2 (**Supplementary Fig.12c and 12d**). All the peaks from the Fe 2p and Mn 2p spectra are in good agreement with previously reported values for Fe^{3+} and Mn^{2+} (*ACS Nano* **2017**, 11, 3614−3631, *Nat. Biomed. Eng*. **2023**, 7, 221-235). Furthermore, the result of Energy Dispersive X-ray (EDX) analysis further proved the existing Mn and Fe elements within the as-synthesized $FeMnO_x$ nanoparticle (**Supplementary Fig.12e**). These results indicated the successful preparation of $FeMnO_x$ nanoparticle.

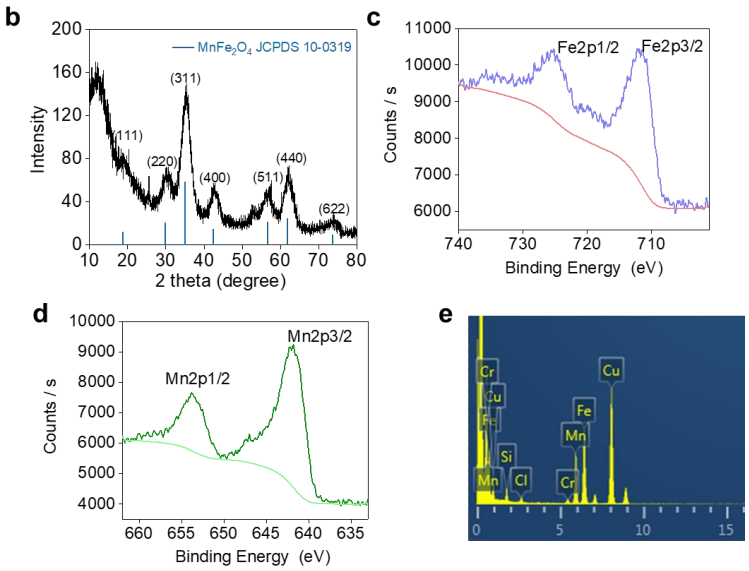

Supplementary Fig. 12. Characterization of $FeMnO_x$ nanoparticle. (b) Powder X-ray diffraction (XRD) patterns of the $FeMnO_x$ nanoparticle. **(c and d)** Fe 2p and Mn 2p X-ray photoelectron spectroscopy (XPS) of the $FeMnO_x$. **(e)** Energy dispersive X-ray analysis of $FeMnO_x$.

Related experimental methods:

Determination of powder X-ray diffraction (XRD). 5 mL of the sample (15 mg/mL) in a 50 mL centrifuge tube, add 10 mL of anhydrous ethanol, swirl and mix well, centrifuge at 9000 rpm for 10 min, and discard the upper liquid. The obtained black precipitate is blown dry under Ar gas. After drying, the sample is scraped off and ground into powder, and then tested in the XRD system.

Determination of X-ray photoelectron spectroscopy (XPS). 3 mL of the sample (15 mg/mL) in a 50 mL centrifuge tube, add 10 mL of anhydrous ethanol, swirl and mix well, centrifuge at 9000 rpm for 10 min, and discard the upper liquid. The obtained black precipitate is blown dry under Ar gas. After sufficiently drying, the sample is evenly dispersed on the conductive adhesive, and then tested in the **XPS** system.

Determination of energy dispersive X-ray analysis (EDX). 10 μL of $FeMnO_x$ nanoparticle (15 mg/mL) and add to 1.5 mL centrifuge tube, then add 50 μL hexane to dilute. After vortex mixing and ultrasonic treatment, 20 μL solution was dropped onto the copper net and repeated twice. After the liquid of the copper net evaporated, the copper net was folded with electron microscope tweezers and placed under transmission electron microscope for observation.

5). *For the afterglow performance of TA NPs such as brightness, emission wavelength, half-life, it will be better to list a table to compare with all previously reported organic afterglow agents. Some relevant and recent literatures about organic afterglow probes should be cited in the table or text.*

Response: Thank you for your constructive feedback regarding our manuscript. In response to your suggestion, we have compiled a comprehensive table that details the afterglow properties of previously reported organic afterglow agents. This table, which can be found as **Supplementary table 3** in the supplementary materials, includes critical parameters such as brightness, emission wavelength, and half-life, allowing for a direct comparison with our theranostic afterglow nanoparticles (TA NPs).

We have also updated our literature review to include relevant and recent studies on organic afterglow probes, ensuring that our citations are current and pertinent to the context of our work. These references have been duly incorporated into both the main text and the table to provide readers with a thorough understanding of how our TA NPs stand in relation to existing technologies.

Organic afterglow particle	Excitation source	Minimum excitation powder density in solution	Maximum emission wavelength or range	Emission lifetime	Afterglow intensity in solution and in vivo imaging	References
TA NPs	White light source	60 μW/cm^2	640 nm	$t_{1/2}$ ≈600 s	In 1×NeBuffer: ~1.6× 10^6 (p/s/cm^2 /sr)/(5 μg/mL) with white light irradiation (10 mW/cm^2) of 10 s and acquisition time of 60 s; In vivo imaging: ~1× 10^6 (p/s/cm^2 /sr)/(80 μg/mL, 120 μL) with white light irradiation (10 mW/cm^2) of 10 s and acquisition time of 60 s	This work
P1–P5 polymers	365 nm UV light	20 mW/cm^2	508 nm	$t_{1/2}$ ≈869 ms	None	*J. Am. Chem. Soc.* **2023**, 145, 13, 7343–7351
MAS-pH/AL/Cu/GSH	660 nm laser	0.5-1.0 W/cm^2	510-570 nm	$t_{1/2}$ ≈30 s	In PBS buffer: ~8× 10^5 (p/s/cm^2/sr)/(50 μg/mL) with 660 nm laser irradiation (0.5 W/cm^2) of 30 s, and acquisition time of 10 s; In vivo imaging: ~ 10^4 (p/s/cm^2/sr)/(100 μg/mL, 25 μL) with 660 nm laser irradiation (1.0 W/cm^2) of 30 s, and acquisition time of 30 s	*J. Am. Chem. Soc.* **2023**, 145, 24386-24400
MAP-pH /$O_2^{\bullet-}$ /LAP	660 nm laser	0.8-1.0 W/cm^2	510-570 nm	$t_{1/2}$ ≈60 s	In PBS buffer: ~2-6× 10^5 (p/s/cm^2/sr)/(50 μg/mL) with 660 nm laser irradiation (0.8 W/cm^2) of 30 s and acquisition time of 30 s; In vivo imaging: ~4 ×10^5 (p/s/cm^2/sr)/((50 μg/mL, 25 μL) with a 660 nm laser irradiation (1.0 W/cm^2) of 30 s and acquisition time of 30 s	*J. Am. Chem. Soc.* **2023**, 145, 9, 5134–5144
Chlorin Nanoparticle	Halogen lamp, 808 nm laser	0.1 W/cm^2 or 1 W/cm^2	660-680 nm	$t_{1/2}$ ≈1.5 h	In PBS buffer: ~1.5 × 10^6 (p/s/cm^2/sr)/(50 μM) with Halogen lamp irradiation of 60 s and acquisition time of 10 s; In vivo imaging:~3×10^3 (p/s/cm^2/sr)/(25 μg/mL, 50 μL) with Halogen lamp irradiation of 60 s and acquisition time of 10 s.	*J. Am. Chem. Soc.* **2022**, 144, 15, 6719
P-TNP	White LED lamp, xenon lamp	2 W/ cm^2	630 nm	$t_{1/2}$ ≈120 s	In H_2O solution: ~800 (cps/mm^2)/(100 mg/mL) with white LED lamp irradiation (2 W/cm^2) of 60 s, and acquisition time of 60 s; In vivo imaging:~1.5×10^4 (p/s/cm^2/sr)/(0.1 mg/mL, 200 μL) with white LED lamp irradiation (2 W/cm^2) of 120 s, and acquisition time of 60 s	*Chem. Sci.*,**2020**, 11, 419
Nat. Commun.,**2020**, 11, 446	808 nm laser	1 W/cm^2	775 nm	$t_{1/2}$ ≈396 s	In PBS buffer: ~6×10^6 (p/s/cm^2/sr)/(58/28/2.2 μg/mL F12*(BF^{4-})$_2$/MEH-PPV/NIR775) with 808 nm laser irradiation (1W/cm^2) of 60 s, and acquisition time of 60 s; In vivo imaging: ~3×10^5 (p/s/cm^2/sr)/(211/100/8 μg F12*(BF^{4-})$_2$/MEH-PPV/NIR775, 200 μL) with 808 nm laser irradiation (1W/cm^2) of 60 s, and acquisition time of 60 s.	*Nat. Commun.*,**2020**, 11, 446
OSN1-T	365 nm UV light	10 mW/cm^2	530 nm and 570 nm	$t_{1/2}$ ≈10s	In PBS buffer: ~6×10^{10} (p/s/cm^2/sr)/(1.6 μM) with handheld UV lamp irradiation (12 W) of 60 s, and acquisition time of 10 s; In vivo imaging:~1.5×10^4 (p/s/cm^2/sr)/(16 μM)with UV light irradiation (18 mW/cm^2) of 60 s, and acquisition time of 10 s	*Adv. Mater.* **2017,** 29, 1606665
SPN-NCBS; SPN-thiol	808 nm laser	1 W/cm^2	780 nm	$t_{1/2}$ ≈396 s	In water: ~1×10^6 (p/s/cm^2/sr)/(1.25 μg/mL) with 808 nm laser irradiation (1 W/cm^2) of 60 s, and acquisition time of 30 s; In vivo imaging:~5.7×10^5 (p/s/cm^2/sr)/(μg/mL), 0.25 mg/mL, 2 μL) with 808 nm laser irradiation (0.5 W/cm^2) of 60 s, and acquisition time of 180 s	*Nat. Biotechnol.* **2017**, 35, 1102-1110
APtN	808 nm laser	0.25 W/cm^2	550 nm	$t_{1/2}$ ≈960 s	In PBS buffer: ~1.5×10^6 (p/s/cm^2/sr)/(1 mg/mL) with 808 nm laser irradiation (0.25 W/cm^2) of 10 s, and acquisition time of 60 s; In vivo imaging:~1.5×10^4 (p/s/cm^2/sr)/(400 μg/mL, 200 μL) with 808 nm laser irradiation (0.25 W/cm^2) of 20 s, and acquisition time of 60 s	*Adv. Mater.* **2019,** 31, 1902672
mTPA-N	365 nm UV light	95 mW/cm^2	515 – 640 nm	$t_{1/2}$ ≈13 ms	In aqueous solution: ~7×10^4 (p/s/cm^2/sr)/(300 μg/mL) with UV irradiation (95 mW/cm^2) of 5 s and exposure time of 5 s; In vivo imaging:~9×10^5 (p/s/cm^2/sr)/(600 μg/mL, 50 μL) with UV irradiation (95 mW/cm^2) of 5 s, and exposure time of 5 s	*Adv. Mater.* **2020,** 32, 2006752
Q-SNAP	Ultrasound	1.5 W/cm^2	780 nm	$t_{1/2}$ ≈ 90 s	In PBS buffer:~2×10^6 (p/s/cm^2/sr)/(10 μg/mL) with ultrasound irradiation (1.5 W/cm^2) of 30 s, and acquisition time of 1 s; In vivo imaging: ~7×10^4 (p/s/cm^2/sr)/(2 mg/kg mice) with ultrasound irradiation (1.5 W/cm^2) of 30 s and acquisition time of 10 s	*Adv. Mater.* **2023**, *35*, 2211651
TPP-DO	Halogen lamp	50 mW/cm^2	650 nm	$t_{1/2}$ ≈120 s	In PBS buffer:~4.5×10^8 (p/s/cm^2/sr)/(125 μM) with halogen lamp irradiation (50 mW/cm^2) of 10 s, and acquisition time of 5 s; In vivo imaging: ~7×10^4 (p/s/cm^2/sr)/(200 μg/mL, 2000 μL) with halogen lamp irradiation (50 mW/cm^2) of 10 s, and acquisition time of 10 s;	*Angew. Chem. Int. Ed.* **2024,** 63, e202313117

Supplementary Table 3. Luminescence characterization comparison of reported organic afterglow materials.

6). *The afterglow spectrum of TA NPs, core-satellite probe before and after APE1 activation can be supplemented*

Response: We appreciate your suggestion to include the afterglow spectrum of TA NPs and the core-satellite probe both before and after APE1 activation. Following your advice, we have now obtained the afterglow spectra using a fluorophotometer, with the parameters set to no excitation and a slit width of 20 nm, after a 10-second white light irradiation at a power density of 10 mW/cm^2. As indicated in the **Fig. 1m**, the TA NPs demonstrated a prominent luminescence peak at 650 nm.

To acquire the afterglow spectra of the APE1-probe with and without APE1 activation, we incubated the APE1-probe with APE1. In contrast, we employed identical conditions without APE1 as a control. After incubation, we performed afterglow imaging of the

samples using the IVIS Spectrum imaging system (Lumina XR), again with no excitation but with an irradiation time of 10 seconds and an acquisition time of 60 seconds.

The results, presented in **Supplementary Fig. 18**, revealed that the APE1-probe without APE1 incubation displayed negligible afterglow signal intensity across all channels, thus confirming the low background signal due to the presence of afterglow resonance energy transfer (ARET). In contrast, upon APE1 activation, a significant increase in signal intensity was observed specifically in the DsRed channel, aligning with the peak wavelength observed in **Figure 1m**. These findings substantiate the APE1-activated afterglow luminescence within the 570-650 nm range, attributable to the disruption of ARET between TA NPs and $FeMnO_x$@BHQ_3.

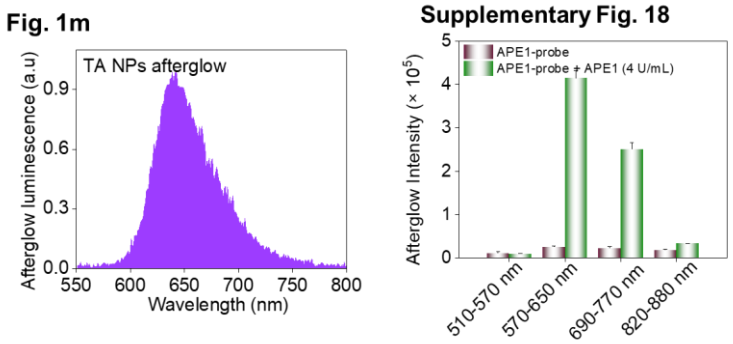

Fig. 1m the afterglow spectrum of TA NPs (1 mL, 100 μg/ml, 10 mW/cm^2, irradiation time: 10 s, fluorophotometer： no excitation and slit width = 20 nm). **Supplementary Fig. 18.** Total afterglow signal intensity of APE1-probe before and after APE1 activation in different channel (100 μL, 5 μg/ml, 10 mW/cm^2, irradiation time: 10 s, acquisition time: 60 s, n = 3). Data are means ± SD

Related experimental methods:

Afterglow spectra analysis of the APE1-probe before and after activation. To acquire the afterglow spectra of the APE1-probe with and without APE1 activation, we incubated the APE1-probe at a concentration of 5 μg/mL with APE1 (4 U/mL) in 1 × Nebuffer, resulting in a total volume of 100 μL. We employed identical conditions without APE1 as a control. Post-incubation at 37 °C for 2 hours, we performed afterglow imaging of the samples using the IVIS Spectrum imaging system (Lumina XR), again with no excitation but with an irradiation time of 10 seconds and an acquisition time of 60 seconds. The emission channels were varied (GFP: 510-570 nm, DsRed: 570-650 nm, Cy5.5: 690-770 nm, and ICG: 820-880 nm).

7). What is the quenching efficiency after assembly of TA and FeMnOx? Can the nanoparticles recover the afterglow luminescence similar to TA NPs in saturated APE1?

Response: Thank you for addressing the inquiry about quenching efficiency and luminescence recovery. In response to your question about the quenching efficiency following the assembly of TA NPs with $FeMnO_x$-BHQ, we conducted a series of controlled experiments. The afterglow luminescence intensity of both TA NPs-DNA1 and APE1-probe was measured using the IVIS Spectrum imaging system (Lumina XR), with an irradiation time of 10 seconds and an acquisition time of 60 seconds. Our findings showed that the $FeMnO_x$-BHQ quenched the afterglow luminescence of the TA NPs within the APE1-probe complex by 95.0 ± 3.0 % (**Fig.1o**). This high level of quenching efficiency can be attributed to the effective afterglow resonance energy transfer between the components.

Regarding the recovery of afterglow luminescence, we first established a baseline by recording the afterglow imaging of TA NPs-DNA1 in 1× Nebuffer solution. Subsequently, we incubated the APE1-probe with APE1 enzyme (4 U/mL) in the same buffer. After a 2-hour incubation period, we performed afterglow imaging again under identical conditions. The comparative analysis revealed that the luminescence recovery rate in the APE1-probe solution post-APE1 activation was 28 ± 2% (**Supplementary Fig. 20**). This data indicates that while there is a notable recovery of luminescence upon APE1 activation, the luminescence does not

return to the full original intensity of the TA NPs. This partial recovery is likely due to the specific interactions and efficiency of the APE1 enzyme in cleaving the DNA strands in the probe, thus disrupting the quenching mechanisms and allowing for the return of some, but not all, of the afterglow signal.

Fig. 1o **Supplementary Fig. 20**

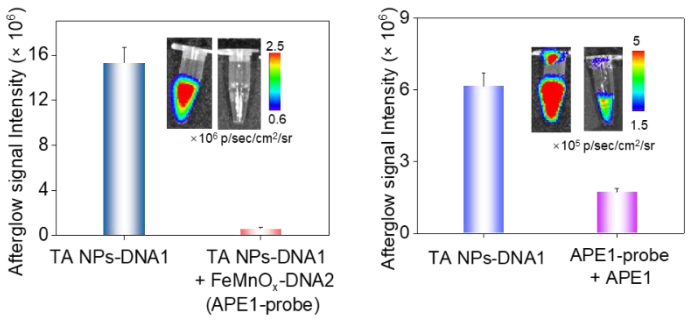

Fig. 1o The afterglow luminescence intensities of TA NPs-DNA1 and TA NPs -DNA1 assembled with $FeMnO_x$-DNA2 (APE1-probe) in DPBS buffer (100 μL, 5 μg/ml, 10 mW/cm^2, irradiation time: 10 s, acquisition time: 60 s, n = 6), as well as the data of quenching rate of $FeMnO_x$-DNA2 to TA NPs-DNA1 (quenching efficiency= 95.0 ± 3.0%). **Supplementary Fig. 20**. the afterglow luminescence intensities of TA NPs -DNA1 and APE1-probe incubated with APE1 (4 U/mL) in 1 × Nebuffer (100 μL, 5 μg/ml, 10 mW/cm^2, irradiation: 10 s, acquisition time: 60 s, n = 6), as well as the data of recovery rate of APE1-probe after incubation with APE1 (recovery rate = 28 ± 2%). Data are means ± SD

Related experimental methods:

The calculation of quenching efficiency after assembly of TA and $FeMnO_x$. TA NPs-DNA1 (5 μg/mL) and APE1-probe (5 μg/mL) in DPBS was measured for afterglow imaigng using the IVIS Spectrum imaging system (Lumina XR), with an irradiation (10 mW/cm^2) time of 10 seconds and an acquisition time of 60 seconds.

The calculation of afterglow **luminescence recovery of APE1-probe after activation.** We determined the afterglow imaging of TA NPs-DNA1 in a 1× Nebuffer solution for establishing a baseline. Subsequently, we incubated the APE1-probe (100 μL, 5 μg/mL,) with APE1 enzyme (4 U/mL) in the same buffer. After a 2-hour incubation period, we performed afterglow imaging again under identical conditions using

8). *Please provide un-cropped WB of Fig. 3n*

Response: In response to your suggestion, we have included the uncropped Western Blot (WB) images in the supplementary materials. These images present the full scope of the blots, detailing both the APE1 levels and tubulin, which serves as a loading control. We trust that this additional information will facilitate a more comprehensive understanding of the results and ensure the transparency of our experimental process.

Fig. 3n Un-cropped WB images of APE1 expression level and tubulin expression level from Fig. 3n

9)*. As illustrated in Fig. 6 and 7, the author evaluated that radiation-induced liver injury and upregulated APE1 by afterglow and MRI. However, the author should provide additional data to demonstrate liver injury with increased of radiation except for H&E staining, such as biochemical analysis.*

Response: Thank you for the reviewer's constructive feedback regarding the evaluation of radiation-induced liver injury and the upregulation of APE1. In response to your suggestion, we have expanded our investigation to include biochemical assays to quantitatively assess liver function post-radiation. After anesthesia, we irradiated mice without xenograft tumors at varying doses (0, 2, 4, and 6 gray) directed specifically to the liver region, using a lead shield to protect the head and abdomen of mice. Each radiation group included five mice. Blood samples were collected 24 hours post-irradiation and submitted for a comprehensive blood biochemistry panel conducted by Wuhan Service bio Technology, which included key liver function tests.

As noted, Alanine aminotransferase (ALT) is a sensitive marker for liver damage. Moreover, Aspartate aminotransferase (AST) is another critical marker for liver injury; when evaluated in conjunction with ALT, it can provide insights into whether the damage is liver-specific or involves other organs. Total bilirubin (TBIL) is a fundamental liver function test, with deviations from normal levels indicating hepatic injury. Total bile acids (TBA) are particularly reflective of excretory organ function and are thus considered a superior early marker for liver injury.

Our biochemical assay results revealed a dose-dependent increase in ALT, AST, TBIL, and TBA levels, correlating with the administered radiation doses (**Supplementary Fig. 45**). These biochemical changes confirm the induction of liver injury by radiation. This data further substantiates the notion that radiation exposure can lead to significant hepatic dysfunction, and underscores the utility of our APE1-probe in detecting and quantifying this injury.

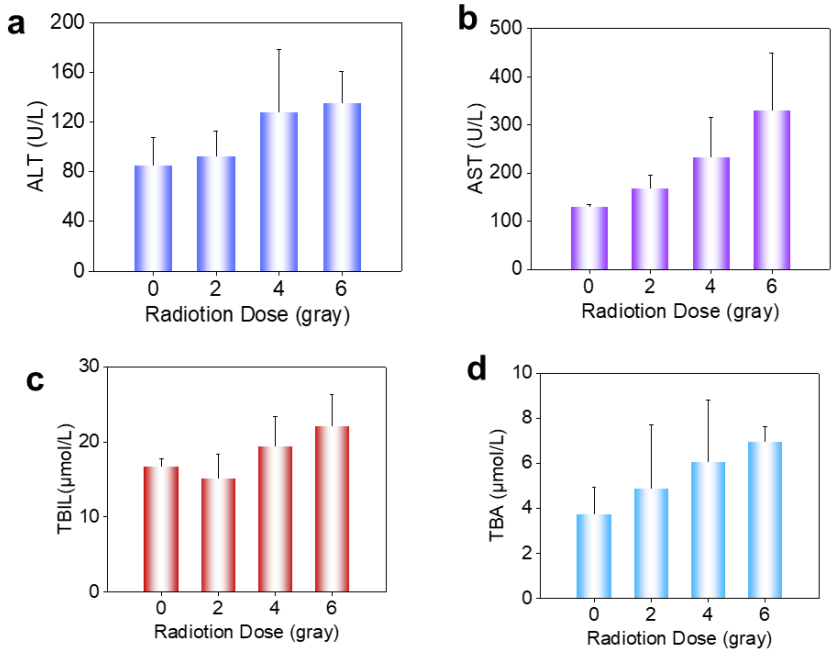

Supplementary Fig. 45 The determination of liver function index of the mice treated with various radiation dose (n = 5). (a) Alanine aminotransferase (ALT). (b) Aspartate aminotransferase (AST). (c) Total bilirubin (TBIL). (d) Total bile acids (TBA). Data are means ± SD.

Related experimental methods:

Hematology analysis. After anesthesia, we irradiated mice (n = 5) without xenograft tumors at varying doses (0, 2, 4, and 6 grays) directed specifically to the liver region, using a lead shield to protect the head and abdomen of mice. Those mice were sacrificed at

24 hours post-irradiation and the blood samples were collected for blood biochemistry assay by Wuhan Service bio Technology, which included key liver function tests.

***10)**. Based on the limited therapy efficiency in Figure 5h, why the authors choose 6 Gy as the highest radiation dose?*

Response: Thank you for your inquiry regarding our choice of radiation dosages in the study presented in **Fig.5h**. In our experiment, we aimed to evaluate the efficacy of the afterglow/MRI imaging capabilities of the APE1-probe in monitoring tumor response to various radiation doses. To achieve this, we administered a range of radiation doses (0, 2, 4, and 6 grays) to mice bearing HeLa tumors. The use of these specific doses was within this range of commonly employed doses, which aimed to balance therapeutic efficacy against potential toxicity.

Following irradiation, we introduced the APE1-probe to the treated mice and performed afterglow/MRI imaging. The imaging results successfully demonstrated a clear and sensitive correlation between the administered radiation dose and subsequent APE1 expression within the tumors.

Further analysis involved observing the progression of tumor growth for 12 days after radiation exposure. The data, depicted in **Fig. 5h** and further detailed in **Supplementary Fig. 43**, showed that a 2 grays dose was capable of partially inhibiting tumor growth when compared to the non-irradiated control. At a 4 grays dose, we noted a more pronounced inhibition, while the 6 grays dose achieved a significant suppression of tumor growth, as evidenced by the tumor growth curves and the final tumor weights measured at the end of the observation period.

While higher doses of radiation could potentially lead to greater therapeutic efficacy, the 6 grays dose was selected as the upper limit for this study to avoid excessive toxicity. This dose was sufficient to demonstrate the therapeutic effect of radiation and the diagnostic potential of the APE1-probe. We believe that our findings contribute valuable insights into the optimization of radiation therapy regimens and the utility of innovative imaging probes in the assessment of treatment response.

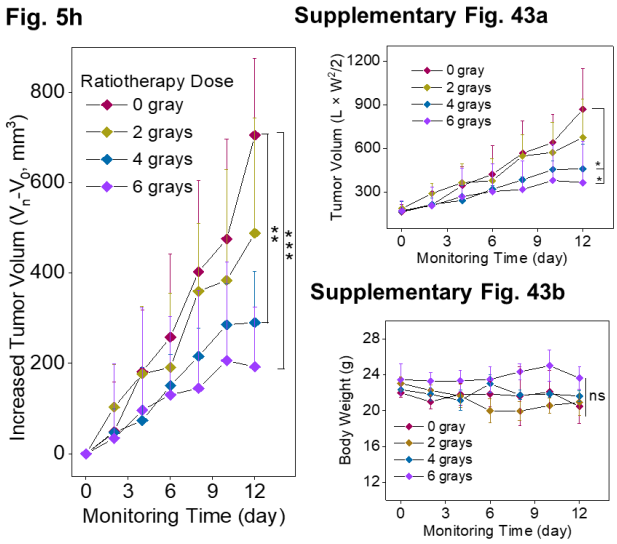

Fig. 5h Increased tumor growth curves (n = 5). **Supplementary Fig. 43a** Tumor growth curve (n = 5). **Supplementary Fig. 43b** Body weight (n = 5). Data are means ± SD. Statistical differences were analyzed by student's t test, **p* < 0.05, ***p* < 0.01, ****p* < 0.001, ns: no statistically significant difference.

Reviewer #2:

Comments: In this manuscript, the authors used APE1 as a potential biomarker for monitoring radiotherapy. They developed a core-satellite probe for imaging the activity of APE1 in living mice using afterglow luminescence and MRI imaging. The combination of MRI and afterglow of APE1-probe could offer both anatomical and functional imaging, enabling precise identification of APE1 location in deep-seated tissues. The authors demonstrated that the probe enables the monitoring of APE1 levels in living mice and

the evaluation of radio-resistance and radiation-induced liver injury, providing early prediction of radiotherapy outcome. Overall, this work is interesting. Some concerns need to be addressed before publication.

Response: Thank you for your assessment and the recommendation regarding our manuscript. We are appreciative of the time you have invested in reviewing our work and are grateful for the constructive critique that has provided us with an opportunity to refine our study. In response to your comments, we have conducted a thorough revision of our manuscript to address the concerns raised. We have made a concerted effort to ensure that our findings are presented with greater clarity and that the manuscript as a whole meets the high standards required for publication.

1). *In previous work, spatially selective monitoring of subcellular APE1 dynamics in response to mitochondria-targeted photodynamic therapy has been reported, which indicated APE1 could be used as an indicator for real-time evaluation of PDT efficacy. This should be discussed in the Introduction with related reference cited.*

Response: Thank you for the reviewer's constructive comment regarding the role of APE1 in evaluating photodynamic therapy (PDT) efficacy. We have revised the introduction to incorporate this important aspect of APE1's application and to reference the pertinent study.

In the revised introduction, we now discuss the significance of APE1 in the cellular response to PDT. Previous studies have demonstrated that APE1 dynamics within subcellular compartments, particularly the mitochondria, can serve as real-time indicators of PDT efficacy. This is due to the enzyme's role in repairing oxidative DNA damage, which is a primary effect of the cytotoxic reactive oxygen species (ROS) generated during PDT.

We have cited the relevant work that explores the spatially selective monitoring of APE1 as a method to assess the progression and effectiveness of PDT. This addition underscores the versatility of APE1 as a biomarker beyond the scope of radiotherapy, highlighting its potential in the broader context of cancer treatment modalities. The citation provides readers with direct access to the study, enriching the background against which our APE1-probe is presented.

The specific text added to the introduction is as follows: " Recently, spatially selective monitoring of APE1 level in mitochondria in cancer cells through fluorescence imaging has been employed to evaluate the outcome of photodynamic therapy" This statement, along with the accompanying citation (*Angew. Chem. Int. Ed. Engl.* **2023**, 62, e202217702, *Angew. Chem. Int. Ed. Engl.* **2022**, 61, e202203238, *Angew. Chem. Int. Ed. Engl.* **2021**, 60, 8923-8931), offers a comprehensive perspective on the multifaceted role of APE1 in cancer therapy assessment.

2). *The author emphasized the symptoms of liver injury could overlap with those of other liver diseases. In fact, the up-regulation of APE1 amount is also present in these diseases, such as hepatitis. How do the probes distinguish radiation-induced liver injury from other liver diseases? Although the author provided a good correlation between radiation dose, ROS generation, DNA damage level, and APE1 level in the liver, the association between APE1 activity and liver injury is lacking.*

Response: Thank you for your insightful comment on our manuscript. We acknowledge the complexity of liver disease symptoms and the challenge of distinguishing radiation-induced liver injury from other liver pathologies using APE1 as a biomarker, given its upregulation in various conditions such as hepatitis.

In our study, to specifically correlate APE1 activity with radiation-induced liver injury, we carefully designed our experiments to control for variables that could confound our observations. The mice used in our experiments were subjected to precise doses of X-ray radiation strictly localized to the liver region, followed by the administration of the APE1-probe. Subsequent imaging (**Fig. 6d, 6e, and 6k**), including afterglow and MRI, demonstrated a dose-dependent increase in signal intensity directly associated with the radiation dose.

To reinforce these findings, we employed histological and biochemical analyses. The confocal imaging of liver sections stained with DCFH-DA and H_2AX antibody confirmed increased ROS generation and DNA damage respectively, in a radiation dose-dependent manner (**Fig. 7b-e**). Additionally, fluorescence confocal images verified a corresponding increase in APE1 levels in the liver (**Fig. 7f, g**). To provide a quantitative assessment of liver injury, we performed biochemical analyses measuring liver function

indices such as ALT, AST, and TBIL (**Supplementary Fig 45**). These indices provided a clear indication of liver injury severity corresponding to the radiation doses administering.

It is essential to note that the experimental design of our study, involving mice treated solely with varying radiation doses, established a controlled setting that allowed for the isolation of radiation effects on liver injury. This approach ensured that the observed elevations in APE1 levels and the associated afterglow/MRI signals were directly attributable to the radiation exposure rather than other liver diseases.

While we recognize that APE1 upregulation is a response seen in diverse liver conditions, the stringent control of experimental variables in our study enabled us to confidently attribute the monitored liver injury to radiation treatment alone. This clarity in the causal relationship allows us to assert the utility of the APE1-probe in specifically evaluating radiation-induced liver organ injury, thus underscoring the value of our findings in the context of radiotherapy monitoring.

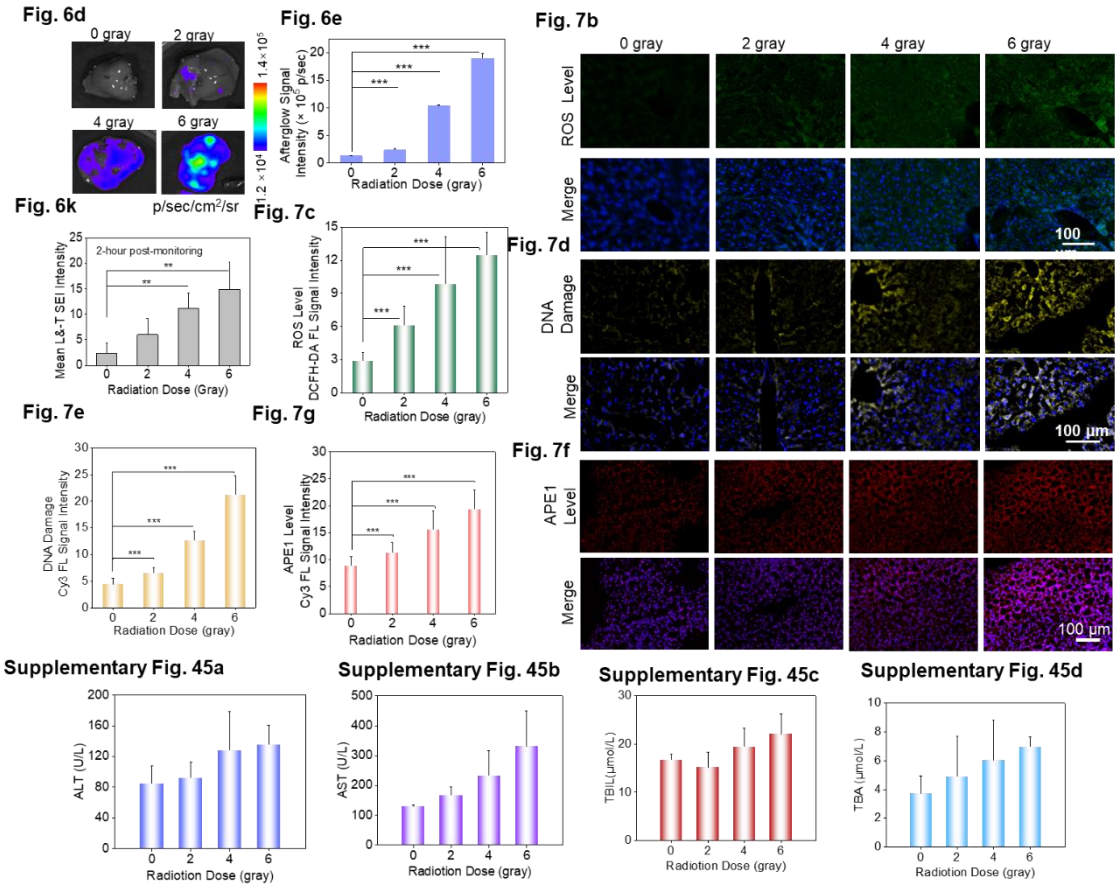

Fig. 6d and 6e Afterglow images and signal intensity of in-vitro liver organ after injection of APE1-probe for 8 hours (n = 3). **Fig. 6k** Quantified signal intensity of L&T-SEI MRI images (ΔT_1 - ΔT_2 value). **Fig. 7b and 7c** Liver organ slice staining with DCFH-DA for testing ROS yield (n = 4 slices × 10). **Fig. 7d and 7e** Liver organ slice incubating with H_2AX antibody and Cy3-labeled IgG for testing DNA damage (n = 4 slices × 10). **Fig. 7f and 7g** Liver organ slice incubating with anti-APE antibody and Cy3-labeled IgG for testing APE1 level (n = 4 slices × 10). **Supplementary Fig.45a-45d** The determination of liver function index of the mice treated with various radiation dose (n = 5) (ALT: alanine aminotransferase; AST: aspartate aminotransferase; TBIL: total bilirubin; TBA: total bile acids). Data are means ± SD. Statistical differences were analyzed by student's t test, $^{**}p<0.01$, $^{***}p<0.001$.

Related experimental methods:

Hematology analysis. After anesthesia, we irradiated mice (n = 5) without xenograft tumors at varying doses (0, 2, 4, and 6 gray) directed specifically to the liver region, using a lead shield to protect the head and abdomen of mice. Those mice were sacrificed at 24 hours post-irradiation and the blood samples were collected for blood biochemistry assay by Wuhan Service bio Technology,

which included key liver function tests.

3)*. In Fig. 7f, anti-APE1 was used to corroborate whether APE1 levels in the liver increase in a radiation dose dependent manner. The results showed APE1 levels in the cytoplasm appeared to increase in a radiation dose-dependent manner. Since APE1 is primarily residing in the nucleus of cells, why was there no nuclear signal of APE1 in liver slice incubated with anti-APE1 antibodies?*

Response: Thank you for addressing the reviewer's question regarding the localization of APE1 in liver cells following radiation treatment. In response to your observation, we have carefully re-examined the imaging data and adjusted the contrast and brightness settings to better reveal the subcellular localization of APE1. These revised images are now presented in **Fig.7f**. Upon closer inspection of the enhanced images, it is evident that APE1 is present within the nucleus of the liver cells, consistent with its known nuclear localization in untreated cells. Furthermore, as the radiation dose increase, we observe an augmented fluorescence signal not only in the cytoplasm but also within the nucleus. This indicates that APE1 is translocated to the cytoplasm in response to radiation-induced liver organ injury, while also remaining present in the nucleus. These findings suggest a dynamic redistribution of APE1 in liver cells undergoing radiation-induced stress, reflecting its role in responding to DNA damage both within the nucleus and the cytoplasm. This nuanced understanding of APE1's behavior in injured liver cells adds an important layer of insight to our study and may have implications for the interpretation of APE1 as a biomarker for liver organ injury.

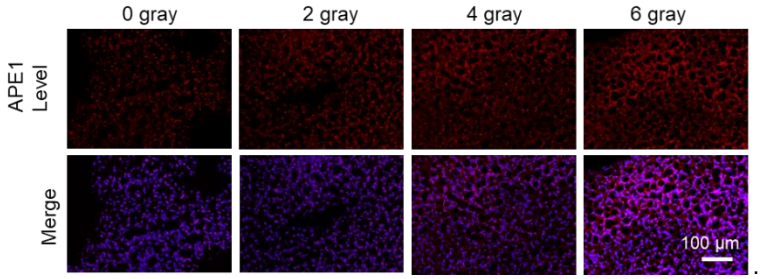

Fig. 7f Liver organ slice incubating with anti-APE antibody and Cy3-labeled IgG for testing APE1 level

4)*. In the core-satellite nanoprobe, how many FeMnOx particles are assembled on the TA NPs?*

Response: Thank you for the reviewer's question regarding the composition of our core-satellite nanoprobe. In response to your query about the number of $FeMnO_x$ particles associated with each TA nanoparticle (NP), we have analyzed transmission electron microscopy (TEM) images to estimate the number. By meticulously examining both the TEM images and the higher magnification TEM images, we have conducted a manual count of the $FeMnO_x$ particles that are assembled around individual TA NPs. Based on this count, we estimate that there is an average of approximately 53 ± 7 $FeMnO_x$ particles surrounding each TA NP.

We have taken care to ensure that this count is as accurate as possible by reviewing multiple images and averaging our counts to account for any variability in particle assembly. This detailed analysis has provided us with a confident estimate of the number of $FeMnO_x$ particles per TA NP, which we believe is an important detail for understanding the structure and functionality of our core-satellite nanoprobe.

5)*. Aside from the afterglow/MRI measurements, gel shift experiment is essential to directly validate the responses of probes towards APE1.*

Response: Thank you for your suggestion regarding the validation of the APE1-probe response to APE1. In addition to the afterglow/MRI experiments previously described, we recognize the importance of directly observing the interaction of the probe with APE1. To this end, we have expanded our experimental approach to include a gel shift assay, which is a direct and established method to visualize the cleavage of DNA by nucleases such as APE1.

In the initial experiments described in our manuscript:

We observed a significant decrease in the hydrodynamic size of the APE1-probe upon incubation with APE1, as measured by dynamic light scattering (DLS), indicating disassembly of the probe due to APE1 cleaving the abasic sites (**Fig. 2b**).

We demonstrated an APE1-concentration-dependent recovery of the afterglow signal, showing enhancing luminescence with increasing amounts of enzyme, which suggests successful activation of the APE1-probe by APE1-mediated cleavage (**Fig. 2c**).

We monitored the corresponding changes in MRI relaxation times, revealing a decrease in both T_1 and T_2 as a function of APE1 concentration, which translates into an enhanced MRI signal (**Supplementary Fig. 21 and Fig. 2f**).

We acquired MRI images that displayed an increase in signal intensity and positive contrast enhancement upon treatment with varying concentrations of APE1, confirming the probe's responsiveness (**Fig. 2g, h**).

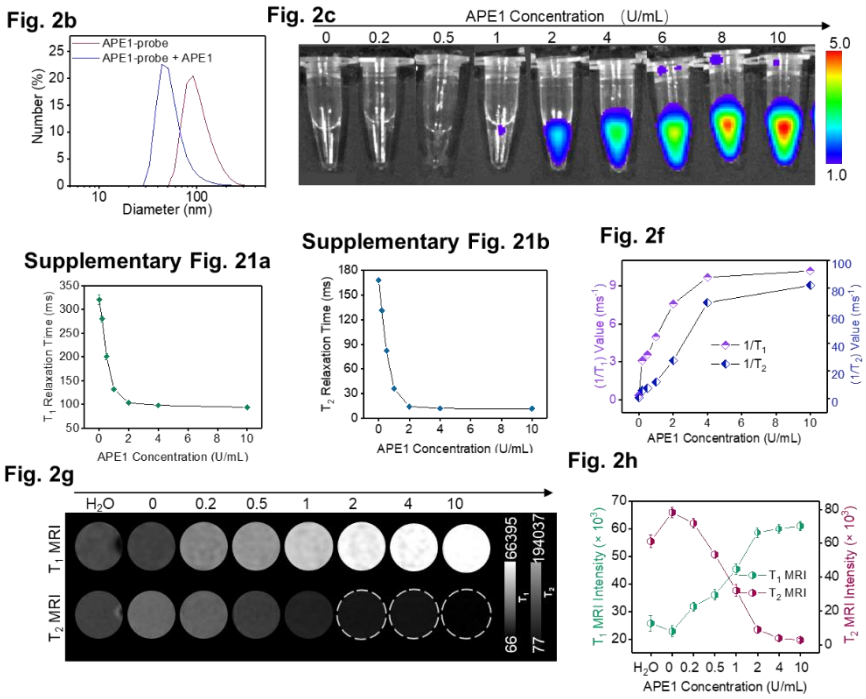

Fig. 2b Hydrodynamic size distribution of APE1-probe before and after incubation with APE1 (10 U/mL). **Fig. 2c** Afterglow images and signal intensity of APE1-probe after incubating with various concentrations of APE1 (0 - 10 U/mL) (containing 5 μg/mL TA NPs, 10 mW/cm^2, irradiation time: 10 s, acquisition time: 60 s). **Supplementary Fig. 21a and 21b** Relaxation time determination of APE1-probe after incubating with various concentrations of APE1 (0 – 10 U/mL) (n = 3). **(Fig. 2f – 2h)** Relaxation time and MRI measurement of APE1-probe (containing 5 μg/mL TA NPs, n = 3) treated with various concentrations of APE1. **Fig. 2f** $1/T_1$ and $1/T_2$ values. **Fig. 2g** T_1 MRI and T_2 MRI images. **Fig. 2h** Quantified T_1 and T_2 MRI signal intensity from (Fig. 2g). Data are means ± SD.

In the revised manuscript, we have further substantiated the probe's specificity and response to APE1 by:

(1) Conducting selectivity experiments that demonstrate the APE1-probe's higher specificity towards APE1 over other potential interferences, underscoring the selectivity of our probe's response.

We incubated APE1-probe with various types of enzymes including DNase I, BSA, MMP-2, and APE1 respectively. Then arranging them for afterglow and MRI imaging. From afterglow imaging (**Supplementary Fig. 24a and 24b**), no obvious afterglow was detected in other enzymes (BSA, DNase I, and MMP-2) incubation. While APE1-treated APE1-probe showed bright afterglow luminescence. Besides, according to T_1 and T_2 MRI imaging, they showed no notable signal change among other enzyme treatments. In contrast, APE1-incubated APE1-probe presented T_1 signal enhancement and T_2 signal descent (**Supplementary Fig.24c-e**). Overall, these results indicated the specific activation of APE1-probe for APE1, and high anti-interference of APE1-probe to other enzymes.

(2) Performing a gel shift assay where we observed effective cleavage of the DNA component of the probe by APE1, providing direct evidence of the enzymatic activity.

To validate the responses of probes towards APE1, we directly incubated DNA1-DNA2 double-strands with APE1 and analyzed the cleaved effect through polyacrylamide gel electrophoresis (PAGE), in contrast, free DNA1 -DNA2 double strands was used as controls. Form PAGE analysis results, DNA1-DNA2 double strands could be cleaved by APE1 enzyme to fragment.

The collective data from these diverse experimental approaches provide robust confirmation of the APE1-probe's activation by APE1, which is key for its application in afterglow signal recovery and MRI signal enhancement. This comprehensive set of results underscores the probe's potential for accurate and sensitive imaging of APE1 activity in vivo.

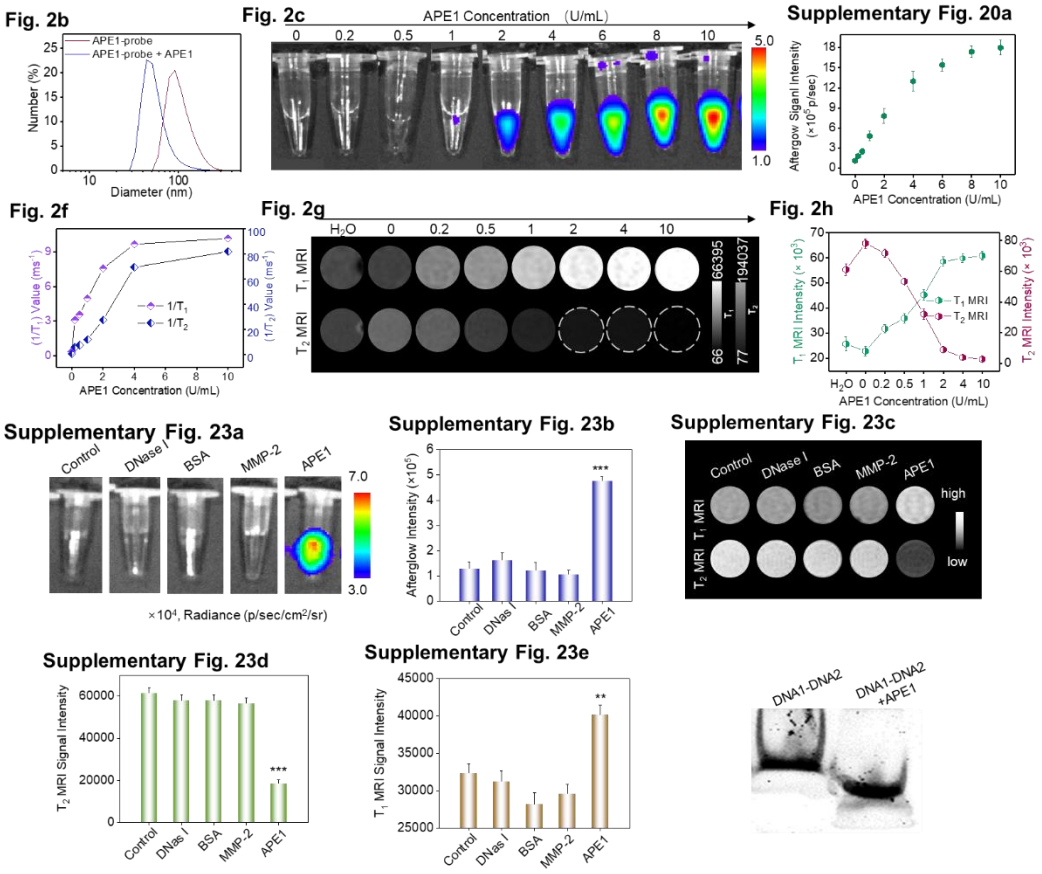

Fig. 2b Hydrodynamic size distribution of APE1-probe before and after incubation with APE1 (10 U/mL). **Fig. 2c and Supplementary Fig. 20a** Afterglow images and signal intensity of of APE1-probe after incubating with various concentrations of APE1 (0 - 10 U/mL) (containing 5 μg/mL TA NPs, 10 mW/cm^2, irradiation time: 10 s, acquisition time: 60 s). **Fig. 2f – 2h** Relaxation time and MRI measurement of APE1-probe (containing 5 μg/mL TA NPs, n = 3) treated with various concentrations of APE1. **Fig. 2f** $1/T_1$ and $1/T_2$ values. **Fig. 2g** T_1 MRI and T_2 MRI images. **Fig. 2h** Quantified T_1 and T_2 MRI signal intensity from (Fig. 2g). **Supplementary Fig. 23a and 23b** Afterglow images and signal intensity of APE1-probe (5 μg/mL) incubated with DNase I (5 U/mL), BSA (500 ng/mL), MMP-2 (500 ng/mL), and APE1 (4 U/mL), respectively (n = 6). Data are means ± SD. Statistical differences were analyzed by student's t test, ***p*<0.01. **Supplementary Fig. 23c** T_1 and T_2 MRI images of APE1-probe (5 μg/mL) incubated with DNase I (5 U/mL), BSA (500 ng/mL), MMP-2 (500 ng/mL), and APE1 (4 U/mL), respectively. **Supplementary Fig. 23d and 23e** quantification of T_1 and T_2 MRI signal intensity from (23 c) (n = 3). Data are means ± SD. Statistical differences were analyzed by student's t test, ***p*<0.01, ****p*<0.001. Polyacrylamide gel electrophoresis (PAGE) of various DNA samples.

6)*. In Fig. 2d, the author claimed the limit of detection calculated by the probes was lower than most fluorescence probes used for APE1 detection. However, when calculating the detection limit, a lower concentration should be selected, not within the detection range (0-4 U/ml).*

Response: Thank you for your constructive feedback on our methods for calculating the limit of detection (LOD). In accordance with your recommendation, we have revised our approach and recalculated the LOD for the APE1-probe with APE1. We focused on a lower concentration range, specifically from 0 to 1 U/mL, to ensure the LOD is reflective of the probe's sensitivity at minimal detectable concentrations. The updated data, presented in **Supplementary Fig. 19b**, illustrates a nearly linear correlation between the afterglow signal intensity and APE1 concentration within this lower range. Utilizing the formula LOD = 3σ/k, where σ is the standard deviation of the response and k is the slope of the calibration curve, we have determined a new LOD for APE1 at 0.0081 U/mL. This updated calculation confirms the high sensitivity of our APE1-probe and supports our claim that it has a lower detection limit when compared to most fluorescence probes currently used for APE1 detection.

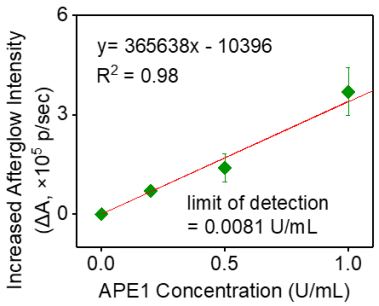

Supplementary Fig. 19b. A linear correlation between the afterglow signal and APE1 concentration (0 - 1 U/mL) (n = 6). Data are means ± SD.

7). *Before the in vivo experiments, it is essential to evaluate the stability of the probes in serum. In addition, biodistribution study should be provided.*

Response: Thank you for your recommendations regarding the assessment of the APE1-probe's stability in serum and its biodistribution in vivo. We have taken your suggestions into consideration and performed the necessary experiments to address these critical aspects.

We evaluated the colloidal stability of the APE1-probe by incubating it in various buffers, including DPBS, 1× Nebuffer, DMEM, and 10% serum, for durations of 0, 2, 4, 6, and 12 hours. The hydrodynamic sizes of the probes were measured using dynamic light scattering (DLS). As depicted in **Supplementary Fig. 16c**, the probes exhibited no significant changes in size across different media, indicating they possess excellent colloidal stability in serum condition.

Furthermore, we conducted a biodistribution study to understand how the APE1-probe distributes throughout the body post-administration. Mice bearing HeLa xenograft tumors were exposed to varying radiation doses (0, 2, 4, and 6 grays). Two hours post-radiation, we administered the APE1-probe intravenously and utilized the IVIS Spectrum imaging system for afterglow imaging. Eight hours following the probe injection, we harvested tumors and major organs for ex vivo afterglow imaging.

The results, which are presented in **Supplementary Fig. 38**, demonstrate a higher afterglow signal within the tumors, with minimal signal detected in the heart, spleen, and kidneys, and only a slight signal in the liver and lungs. This suggests that the APE1-probe is specifically activated within the tumor tissue after radiotherapy. Additionally, a positive correlation was observed between the radiation dose and the afterglow signal intensity in the tumors, implying that higher radiation doses led to increased APE1 expression, which in turn activated the APE1-probe, resulting in a brighter afterglow luminescence signal from tumor. This finding not only supports the probe's specificity for APE1 but also its potential for monitoring radiation-induced changes in APE1 expression within tumors.

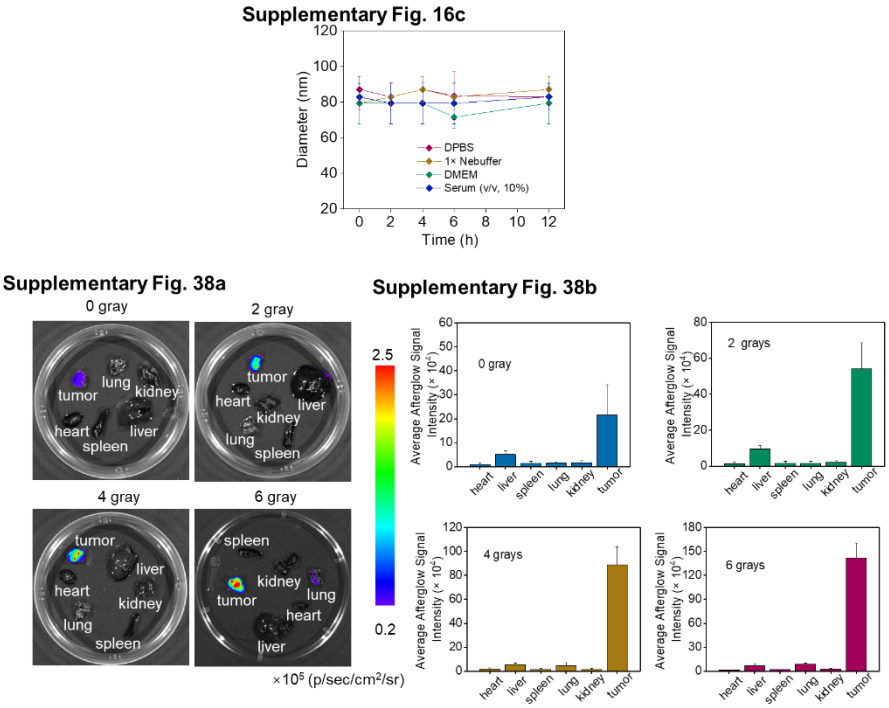

Supplementary Fig. 16c. DLS measurement of APE1-probe under different condition (n = 3). **Supplementary Fig. 38a** Afterglow images of organs and tumors harvested from mice at 8 hours post intravenous injection of APE1-probe (at 10-hour post-radiation treatment). **Supplementary Fig. 38b** Quantified afterglow signal intensity from (**Supplementary Fig. 38a**). Data are means ± SD.

8)*. In Fig.8, the probes could detect the upregulation of APE1 in tumors adjacent to radiation-treated tumors. To further confirm this result, the APE1 level in the non-irradiated left tumor should be testing via conventional immunohistofluorescence technique.*

Response: Thank you for the suggestion. In response to your recommendation, we conducted a comparative immunohistochemical analysis of APE1 levels in non-irradiated tumors, abscopal tumors, and irradiated tumors.

For this study, we utilized a mouse model with two subcutaneous HeLa tumors, selectively irradiating the right tumor with 6 gray (right tumor of Group 1, +X ray) while shielding the left tumor from X-ray irradiation (left tumor of Group 1, -X ray). At four hours post-irradiation, we harvested the tumors to prepare frozen tissue sections. The tumor sections were then subjected to immunostaining with an APE1-specific antibody, followed by incubation with Cy3-conjugated secondary antibodies and counterstaining with DAPI. Fluorescence imaging was acquired using a confocal laser scanning microscope set to the appropriate excitation and emission wavelengths for Cy3 detection.

Following X-ray exposure of the right tumor (Group 1), we noted an increase in fluorescence intensity in both the irradiated right tumor and the non-irradiated left tumor (**Supplementary Fig. 49**).

These findings from the IHC analysis corroborate the imaging results obtained with the APE1-probe, providing strong evidence for the upregulation of APE1 in non-irradiated abscopal tumors.

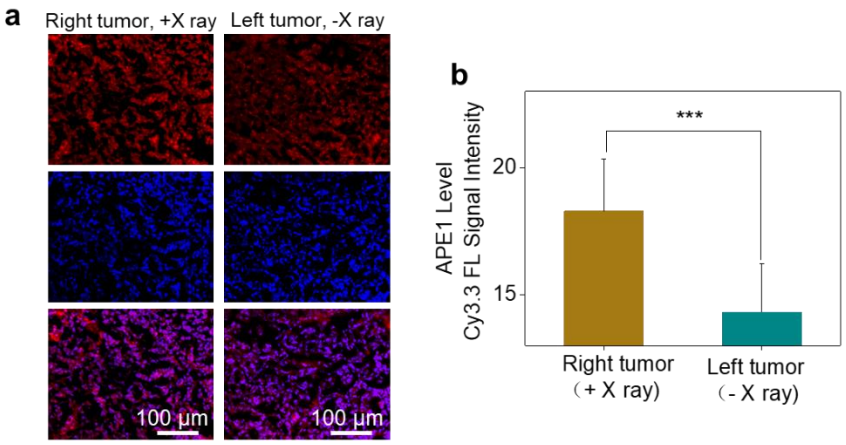

Supplementary Fig. 49 Tumor slice incubating with anti-APE1 antibody and Cy3-labeled IgG for testing APE1 level in Group1 mice (right tumor with X ray radiation, left tumor without X ray radiation). Data are means ± SD.

9). *In Fig. 3j, error bars are incomplete.*

Response: Thank you for pointing out the discrepancy in **Fig. 3j** regarding the error bars. Upon revisiting the figure, we have ensured that all error bars are now complete and accurately represent the variability in our data. We appreciate your attention to detail, and we apologize for any confusion this may have caused.

Reviewer #3:

The manuscript "Imaging-Guided Companion Diagnostics in Personalized Radiotherapy: Monitoring APE1 Activity with Afterglow and MRI Imaging" by Yue et al is an attempt to investigate the potential of the APE1-activated afterglow/MRI probe as a companion diagnostics tool for personalized radiotherapy. Even though, the study is well designed, it need to address following comments/queries:

Response: We are grateful for the opportunity to refine our manuscript and enhance its contribution to the field of personalized radiotherapy. In response to your comments and queries, we have conducted a thorough revision of our manuscript. These revisions include detailed clarifications and additional data where necessary to ensure that our findings are presented with the utmost rigor and transparency. We believe these revisions have strengthened the validation of our APE1-activated afterglow/MRI probe as a companion diagnostic tool and we hope that our manuscript now effectively addresses your concerns.

1)*. Abstract, line 32: "…correlation of afterglow and MRI signals with APE1 expression, radiation dose, intratumor ROS" whether radiation dose delivered decided?*

Response: Thank you for addressing the reviewer's question regarding the correlation between afterglow/MRI signals and APE1 expression in relation to the radiation dose and intratumor ROS levels.

In response to your comment, we have clarified the methodology used to deliver and verify the radiation doses in our study. The radiation dose administered to the tumors was precisely controlled using a radiation dosimeter, ensuring accurate exposure levels. Post-radiation, our immunofluorescence analysis revealed a dose-dependent increase in ROS generation and DNA damage within the tumors. This supports the premise that higher radiation doses correlate with increased cytotoxic ROS production and consequent DNA damage, which in turn stimulates APE1 upregulation.

The APE1 levels quantified through immunofluorescence analysis confirmed this radiation dose-dependent upregulation. To further validate the relationship between radiation dose and APE1 expression, we administered the APE1-probe intravenously and performed afterglow and MRI imaging. The imaging results demonstrated that increased radiation doses led to more pronounced activation of the APE1-probe in the tumors, as evidenced by the amplified afterglow and MRI signals. This directly establishes the

correlation of imaging signals with both the radiation dose and the biological responses it elicits, namely ROS generation and DNA damage, within the tumor microenvironment.

Therefore, we can conclude that the APE1-probe's ability to provide afterglow and MRI signals within the tumor is indeed reflective of the radiation dose-dependent APE1 expression, intratumor ROS, and DNA damage. This correlation underscores the probe's potential as a precise and dynamic imaging tool for assessing the biological impact of radiotherapy.

2). *Abstract, line 36, "Moreover, MRI imaging evaluates the radiation-induced bystander effect," how?*

Response: Thank you for your query regarding the evaluation of the radiation-induced abscopal effect using MRI imaging in our study.

Radiation therapy is known to not only impact targeted cancer cells but also to instigate oxidative stress and DNA damage in adjacent, non-irradiated cells and tissues—this is known as the "radiation-induced abscopal effect." Such an effect broadens the scope of radiation damage, potentially leading to complications in surrounding healthy tissues, such as fibrosis, inflammation, and DNA damage. Given the established link between reactive oxygen species (ROS), DNA damage, and the bystander effect in tumors, APE1 expression is a promising biomarker for this phenomenon.

In our study, we harnessed the APE1-probe to explore the bystander effect. We utilized a murine model with dual subcutaneous HeLa tumors, selectively irradiating one tumor while protecting the other from exposure (**Fig. 8b**). The APE1-probe was then intravenously administered for MRI imaging. As a baseline, a control group with bilateral tumors received no radiation, but were also administered the APE1-probe (Fig. 8c).

Our analysis focused on the signal-to-noise ratio (tumor vs. normal tissue) as shown in Figure 8j. Remarkably, we observed that radiation not only increased the APE1 level in the irradiated tumor but also in the adjacent, non-irradiated tumor within the same animal. This contrasted with the control group's tumors, which displayed lower and consistent APE1 levels in the absence of radiation. This finding implies that the APE1-probe can sensitively detect APE1 upregulation in non-irradiated tumors adjacent to irradiated ones, thus effectively identifying the abscopal effect.

MRI imaging with the APE1-probe offers a non-invasive and high-resolution approach to dynamically visualize the entire body, capturing real-time microstructural changes in APE1 expression. These capabilities are crucial for detecting and quantifying the bystander effect. By monitoring changes in both directly irradiated and abscopal cells, our imaging probe provides insights into the mechanisms at play and aids in the development of strategies to minimize radiation's adverse effects. Moreover, it facilitates the optimization of radiation and immunotherapy protocols by informing decisions on the sequencing, timing, and dosing to enhance the synergy and efficacy of treatment.

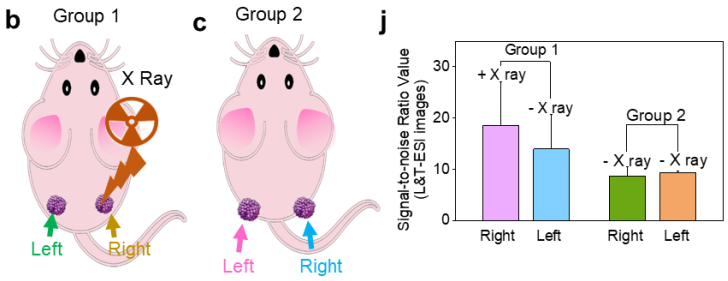

Fig. 8b Scheme illustration of the Group 1 mice with radiation treatment only in right tumor and then intravenous injection of APE1-probe. **Fig. 8c** Scheme illustration of the Group 2 mice with intravenous injection of APE1-probe. **Fig. 8j** Signal-to-noise ratio from subtracted MRI image (n = 3). Data are means ± SD.

3)*. Some of the terminologies like 'ultra-small' and 'ultrabright', is there any basis to use ultra as the size of NP and fluorescence signal appears to be within the range of any other study.*

Response: Thank you for your comment on the use of the terms 'ultrasmall' and 'ultrabright' within our manuscript. The term 'ultrasmall' is employed in the literature to describe nanoparticles with a diameter less than 5 nm (*ACS Nano* **2017**, 11, 3614−3631.

Adv Mater. **2023**, 35, e2301283; *Chem.* **2022**, 8,1956-1981). In our study, the $FeMnO_x$ nanoparticles synthesized through thermal decomposition measured 3.4 ± 0.9 nm in diameter according to TEM images, and displayed a hydrodynamic size of 3.2 ± 0.6 nm in $CHCl_3$ as determined by DLS, justifying the use of 'ultrasmall'.

For 'ultrabright', we acknowledge that the afterglow intensity of nanoparticles can be influenced by several experimental parameters, such as power density, excitation wavelength and duration, acquisition time, emission wavelength, and particle concentration. To objectively assess the brightness of our TA NPs, we compared them to MEHPPV-based nanoparticles (*Nat. Biotechnol.* **2017**, 35, 1102-1110; *Chem. Soc. Rev.* **2019**, 48, 38-71; *Nat. Commun.* **2020**, 11, 446), which have similar absorption and fluorescence properties. As demonstrated in **Fig.1g and 1h**, our TA NPs showed an afterglow luminescence intensity approximately 150 times greater than that of MEHPPV-based nanoparticles at a concentration of 10 μg/mL. This significant enhancement in afterglow intensity supports the characterization of our TA NPs as 'ultrabright'. We have provided these comparisons and details to ensure that our terminology accurately reflects the properties of the nanoparticles studied (**Supplementary table 3**).

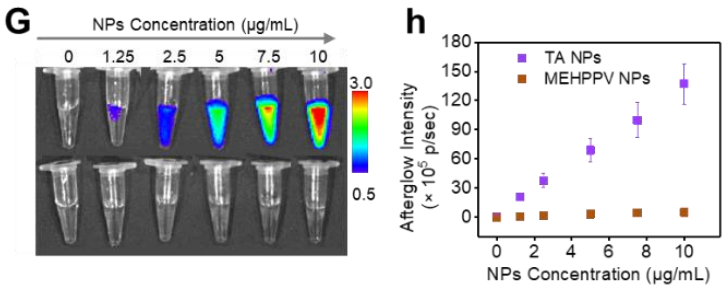

Fig. 1g and 1h Afterglow images and signal intensity of TA NPs nanoparticle and MEHPPV-based nanoparticle (n = 3). All afterglow imaging were obtained with a white light irradiation (10 mW/cm^2) time of 10 s and an acquisition time of 60 s. Data are means ± SD.

Organic afterglow particle	Excitation source	Minimum excitation powder density in solution	Maximum emission wavelength or range	Emission lifetime	Afterglow intensity in solution and in vivo imaging	References
TA NPs	White light source	60 μW/cm^2	640 nm	$t_{1/2}$ ≈600 s	In 1×NeBuffer: ~1.6× 10^6 (p/s/cm^2 /sr)/(5 μg/mL) with white light irradiation (10 mW/cm^2) of 10 s and acquisition time of 60 s; In vivo imaging: ~1× 10^6 (p/s/cm^2 /sr)/(80 μg/mL, 120 μL) with white light irradiation (10 mW/cm^2) of 10 s and acquisition time of 60 s	This work
P1–P5 polymers	365 nm UV light	20 mW/cm^2	508 nm	$t_{1/2}$ ≈869 ms	None	*J. Am. Chem. Soc.* **2023**, 145, 13, 7343–7351
MAS-pH/AL/Cu/GSH	660 nm laser	0.5-1.0 W/cm^2	510-570 nm	$t_{1/2}$ ≈30 s	In PBS buffer: ~8× 10^5 (p/s/cm^2/sr)/(50 μg/mL) with 660 nm laser irradiation (0.5 W/cm^2) of 30 s, and acquisition time of 10 s; In vivo imaging: ~ 10^4 (p/s/cm^2/sr)/(100 μg/mL, 25 μL) with 660 nm laser irradiation (1.0 W/cm^2) of 30 s, and acquisition time of 30 s	*J. Am. Chem. Soc.* **2023**, 145, 24386-24400
MAP-pH /$O_2^{\bullet-}$ /LAP	660 nm laser	0.8-1.0 W/cm^2	510-570 nm	$t_{1/2}$ ≈60 s	In PBS buffer: ~2-6× 10^5 (p/s/cm^2/sr)/(50 μg/mL) with 660 nm laser irradiation (0.8 W/cm^2) of 30 s and acquisition time of 30 s; In vivo imaging: ~4 ×10^5 (p/s/cm^2/sr)/((50 μg/mL, 25 μL) with a 660 nm laser irradiation (1.0 W/cm^2) of 30 s and acquisition time of 30 s	*J. Am. Chem. Soc.* **2023**, 145, 9, 5134–5144
Chlorin Nanoparticle	Halogen lamp, 808 nm laser	0.1 W/cm^2 or 1 W/cm^2	660-680 nm	$t_{1/2}$ ≈1.5 h	In PBS buffer: ~1.5 × 10^6 (p/s/cm^2/sr)/(50 μM) with Halogen lamp irradiation of 60 s and acquisition time of 10 s; In vivo imaging:~3×10^3 (p/s/cm^2/sr)/(25 μg/mL, 50 μL) with Halogen lamp irradiation of 60 s and acquisition time of 10 s.	*J. Am. Chem. Soc.* **2022**, 144, 15, 6719
P-TNP	White LED lamp, xenon lamp	2 W/ cm^2	630 nm	$t_{1/2}$ ≈120 s	In H_2O solution: ~800 (cps/mm^2)/(100 mg/mL) with white LED lamp irradiation (2 W/cm^2) of 60 s, and acquisition time of 60 s; In vivo imaging:~1.5×10^4 (p/s/cm^2/sr)/(0.1 mg/mL, 200 μL) with white LED lamp irradiation (2 W/cm^2) of 120 s, and acquisition time of 60 s	*Chem. Sci.*,**2020**, 11, 419
Nat. Commun.,**2020**, 11, 446	808 nm laser	1 W/cm^2	775 nm	$t_{1/2}$ ≈396 s	In PBS buffer: ~6×10^6 (p/s/cm^2/sr)/(58/28/2.2 μg/mL $F12^*(BF^{4-})_2$/MEH-PPV/NIR775) with 808 nm laser irradiation (1W/cm^2) of 60 s, and acquisition time of 60 s; In vivo imaging: ~3×10^5 (p/s/cm^2/sr)/(211/100/8 μg $F12^*(BF^{4-})_2$/MEH-PPV/NIR775, 200 μL) with 808 nm laser irradiation (1W/cm^2) of 60 s, and acquisition time of 60 s.	*Nat. Commun.*,**2020**, 11, 446
OSN1-T	365 nm UV light	10 mW/cm^2	530 nm and 570 nm	$t_{1/2}$ ≈10s	In PBS buffer: ~6×10^{10} (p/s/cm^2/sr)/(1.6 μM) with handheld UV lamp irradiation (12 W) of 60 s, and acquisition time of 10 s; In vivo imaging:~1.5×10^4 (p/s/cm^2/sr)/(16 μM)with UV light irradiation (18 mW/cm^2) of 60 s, and acquisition time of 10 s	*Adv. Mater.* **2017,** 29, 1606665
SPN-NCBS; SPN-thiol	808 nm laser	1 W/cm^2	780 nm	$t_{1/2}$ ≈396 s	In water: ~1×10^6 (p/s/cm^2/sr)/(1.25 μg/mL) with 808 nm laser irradiation (1 W/cm^2) of 60 s, and acquisition time of 30 s; In vivo imaging:~5.7×10^5 (p/s/cm^2/sr)/(μg/mL), 0.25 mg/mL, 2 μL) with 808 nm laser irradiation (0.5 W/cm^2) of 60 s, and acquisition time of 180 s	*Nat. Biotechnol.* **2017**, 35, 1102-1110
APtN	808 nm laser	0.25 W/cm^2	550 nm	$t_{1/2}$ ≈960 s	In PBS buffer: ~1.5×10^6 (p/s/cm^2/sr)/(1 mg/mL) with 808 nm laser irradiation (0.25 W/cm^2) of 10 s, and acquisition time of 60 s; In vivo imaging:~1.5×10^4 (p/s/cm^2/sr)/(400 μg/mL, 200 μL) with 808 nm laser irradiation (0.25 W/cm^2) of 20 s, and acquisition time of 60 s	*Adv. Mater.* **2019,** 31, 1902672
mTPA-N	365 nm UV light	95 mW/cm^2	515 – 640 nm	$t_{1/2}$ ≈13 ms	In aqueous solution: ~7×10^4 (p/s/cm^2/sr)/(300 μg/mL) with UV irradiation (95 mW/cm^2) of 5 s and exposure time of 5 s; In vivo imaging:~9×10^5 (p/s/cm^2/sr)/(600 μg/mL, 50 μL) with UV irradiation (95 mW/cm^2) of 5 s, and exposure time of 5 s	*Adv. Mater.* **2020,** 32, 2006752
Q-SNAP	Ultrasound	1.5 W/cm^2	780 nm	$t_{1/2}$ ≈ 90 s	In PBS buffer:~2×10^6 (p/s/cm^2/sr)/(10 μg/mL) with ultrasound irradiation (1.5 W/cm^2) of 30 s, and acquisition time of 1 s; In vivo imaging: ~7×10^4 (p/s/cm^2/sr)/(2 mg/kg mice) with ultrasound irradiation (1.5 W/cm^2) of 30 s and acquisition time of 10 s	*Adv. Mater.* **2023**, 35, 2211651
TPP-DO	Halogen lamp	50 mW/cm^2	650 nm	$t_{1/2}$ ≈120 s	In PBS buffer:~4.5×10^8 (p/s/cm^2/sr)/(125 μM) with halogen lamp irradiation (50 mW/cm^2) of 10 s, and acquisition time of 5 s; In vivo imaging: ~7×10^4 (p/s/cm^2/sr)/(200 μg/mL, 2000 μL) with halogen lamp irradiation (50 mW/cm^2) of 10 s, and acquisition time of 10 s;	*Angew. Chem. Int. Ed.* **2024,** 63, e202313117

Supplementary table 3. Luminescence characterization comparison of reported organic afterglow materials.

4). *Introduction, line 74, "Until now, there have been rare reports on imaging APE1 activity in living animals (Table 2)." The major findings of these studies especially related to Cy5 fluorescence should be mentioned.*

Response: Thank you for your suggestion regarding the need to include details about the studies involving imaging APE1 activity in living animals. In response to your comment, we have updated the introduction to provide a more in-depth discussion of the fluorescence imaging techniques used to monitor APE1 activity in vivo, with a particular focus on studies utilizing Cyanine-labeled probes.

The revised text is as follows: "Fluorescence probes that labelled with Cyanine have also been used for real-time imaging of APE1 in cancer cells, but they suffer from limitations including autofluorescence interference and inadequate imaging depth. Until now, there have been rare reports on imaging APE1 activity in living animals (**Supplementary table 2**)".

The revised text now includes an overview of the major findings from these studies, elucidating how the Cy5 fluorescence has contributed to our understanding of APE1's role in various biological processes and disease states. We have also taken care to reference Table 3, which presents a summary of these reports for the reader's convenience.

This expansion of the introduction ensures that the context in which our APE1-probe is situated is both comprehensive and informative, setting the stage for the novel contributions of our work to the field of in vivo APE1 activity imaging.

Signal type	Limit of detection and medium	Design strategy	Detection range	In-vivo imaging	Background interference	Reference
Ultrastrong afterglow luminescence	0.0092 U/mL in 1× NeBuffer 4	No amplification	0 ~ 4 U/mL	Yes	No	This work
Subtraction-enhanced MRI	0.16 U/mL in 1× NeBuffer 4		0 ~ 2 U/mL			
Cy3 fluorescence	0.139 U/mL	No amplification	0 ~ 2.24 U/mL	No		*Chem. Sci.*, **10**, 5959–5966 (2019)
Cy5 fluorescence	3.34×10^{-5} U/mL In 1 × NEBuffer 4	DNA chain hybridization amplification	0 ~ 0.1 U/μL	No		*Chem. Sci*, **14**, 2318 (2023)
Cy5 fluorescence	0.23 U/mL in 1× NeBuffer 4	No amplification	0.5 ~ 100 U/mL	No		*Anal. Chem.*, **95**, 3551−3555 (2023)
FAM fluorescence	0.007 U/ mL unmentioned medium	Toehold-mediated strand displacement	0 ~1 U/mL	No		*Angew. Chem. Int. Ed.*, **62**, e202213884 (2023)
Cy5 fluorescence	0.01 U/mL in 1×Nebuffer 1.1	Catalytic hairpin assembly	0.2 ~1 U/mL	No		*Chem. Sci.*, **11**, 10361–10366 (2020)
FAM and TAMRA fluorescence	7.8×10^{-5} U/ mL in APE1 buffer	Hybridization chain reaction and catalytic hairpin assembly	0.0001 ~ 1.0 U/ mL	No		*Small*, **19**, 2207736 (2023)
Cy5.5 fluorescence	0.22 U/mL in 1× NeBuffer 4	No amplification	0 ~ 2 U/mL	Yes	Autofluorescence	ACS Nano, **14**, 13792−13810 (2023)
Cy3 fluorescence	0.078 U/mL in Tris-acetate buffer	No amplification	0 ~ 1 U/mL	Yes	Autofluorescence	ACS Appl. Mater. Interfaces **15**, 22, 26316–26327 (2023)
Cy5 fluorescence	0.01 U/mL In Tris-HCl buffer	No amplification	0 ~ 0.1 U/mL	Yes	Autofluorescence	Angew. Chem. Int. Ed. **60**,14887 -14891 (2021)

Supplementary table 2. Characterization comparison of representative probe for APE1 detection.

5)*. Scheme 1. APE activation, scheme is not able to clearly indicate how activation takes place and after activation how the structure of NP changes? It is not clear. Too much information is mentioned. The different aspects should be put in boxes to not getting mixed up.*

Response: Thanks for your suggestion! We have outlined the APE-activated site within probe in scheme 1, and integrated the same aspects for clearing different aspects.

Thank you for your feedback on **Scheme 1.** In response to your suggestion, we have revised Scheme 1 to better delineate the activation mechanism. We have achieved this by:

(1) Highlighting the APE1 activation site on the nanoprobe to clearly indicate where the activation occurs.

(2) Simplifying the diagram by reducing unnecessary details to focus on the key stages of activation and structural transformation.

(3) Using distinct visual elements such as boxes or color coding to separate different components and steps within the scheme, ensuring that each aspect is clearly defined and not confounded with others.

These revisions are intended to enhance the readability and comprehension of the activation process by providing a more streamlined and segregated representation of the events that occur upon activation of the nanoprobe by APE1.

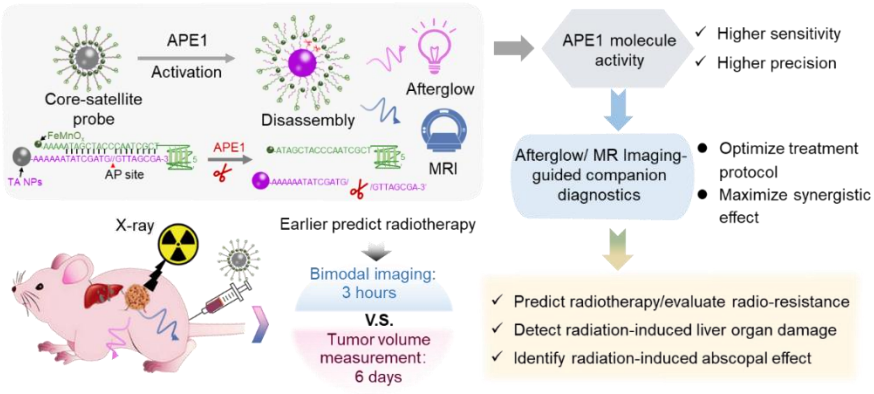

Scheme 1. APE1-responsive afterglow/MRI probe, performed as a companion diagnostics tool for early monitoring of tumor response and toxicity during radiotherapy.

6)*. Table 2, what is meaning of limits of detection and detection range. The conc mentioned shows what? Whether per mL blood or? These aspects need to be mentioned in Figure legend.*

Response: Thank you for your suggestion regarding the clarity of **Supplementary table 2** in our manuscript. The "limit of detection" (LOD) signifies the smallest concentration of an analyte that the method can reliably distinguish from an absence of that analyte (or the background level), albeit not necessarily at a level that is quantifiable. This parameter is a critical metric for assessing the sensitivity of the analytical approach. Utilizing the formula LOD = 3σ/k, where σ is the standard deviation of the response and k is the slope of the calibration curve, we have determined a LOD for APE1 at 0.0092 U/mL (Fig. 2d).

The "detection range," on the other hand, encompasses the span of analyte concentrations over which the method can not only detect but also provide an accurate and reproducible quantification. This range is bounded at the upper end by the highest concentration that the method can accurately measure, which is often limited by the signal becoming non-linear or by saturation of the detection system.

The concentrations reported in **Supplementary table 2** (previous Table 2), expressed in units of activity per milliliter (U/mL), refer specifically to the enzymatic activity of APE1 in the tested samples. This is an important distinction, as it directly relates to the functional capacity of the APE1 enzyme rather than its mass or volume concentration.

We have now included additional details in **Supplementary table 2** to specify the medium of the samples—whether it is blood, a specific buffer solution, or any other relevant condition under which the measurements were taken.

Signal type	Limit of detection and medium	Design strategy	Detection range	In-vivo imaging	Background interference	Reference
Ultrastrong afterglow luminescence	0.0092 U/mL in 1× NeBuffer 4	No amplification	0 ~ 4 U/mL	Yes	No	This work
Subtraction-enhanced MRI	0.16 U/mL in 1× NeBuffer 4		0 ~ 2 U/mL			
Cy3 fluorescence	0.139 U/mL	No amplification	0 ~ 2.24 U/mL	No		*Chem. Sci.*, **10**, 5959–5966 (2019)
Cy5 fluorescence	3.34×10^{-5} U/mL In 1 × NEBuffer 4	DNA chain hybridization amplification	0 ~ 0.1 U/μL	No		*Chem. Sci*, **14**, 2318 (2023)
Cy5 fluorescence	0.23 U/mL in 1× NeBuffer 4	No amplification	0.5 ~ 100 U/mL	No		*Anal. Chem.*, **95**, 3551−3555 (2023)
FAM fluorescence	0.007 U/ mL unmentioned medium	Toehold-mediated strand displacement	0 ~1 U/mL	No		*Angew. Chem. Int. Ed.*, **62**, e202213884 (2023)
Cy5 fluorescence	0.01 U/mL in 1×Nebuffer 1.1	Catalytic hairpin assembly	0.2 ~1 U/mL	No		*Chem. Sci.*, **11**, 10361–10366 (2020)
FAM and TAMRA fluorescence	7.8×10^{-5} U/ mL in buffer	Hybridization chain reaction and catalytic hairpin assembly	0.0001 ~ 1.0 U/ mL	No		*Small*, **19**, 2207736 (2023)
Cy5.5 fluorescence	0.22 U/mL in 1× NeBuffer 4	No amplification	0 ~ 2 U/mL	Yes	Autofluorescence	ACS Nano, **14**, 13792−13810 (2023)
Cy3 fluorescence	0.078 U/mL in Tris-acetate buffer	No amplification	0 ~ 1 U/mL	Yes	Autofluorescence	ACS Appl. Mater. Interfaces **15**, 22, 26316–26327 (2023)
Cy5 fluorescence	0.01 U/mL In Tris-HCl buffer	No amplification	0 ~ 0.1 U/mL	Yes	Autofluorescence	Angew. Chem. Int. Ed. **60**,14887 -14891 (2021)

Supplementary table 2, Characterization comparison of representative probe for APE1 detection.

7). *Introduction, line 85-87, "APE1 in deep-seated tissues in living animals for the first time and significantly boosted the afterglow imaging of APE1 detection range (0 - 4 U/mL) and detection sensitivity (limit of detection: 0.0092 U/mL)". At one place it is mentioned in deep seated tissue and on the other hand detection limit in per mL. What is meaning of conc in which solution, blood or?*

Response: Thank you for the opportunity to clarify the details regarding the detection range and limit of detection for APE1 as stated in the introduction. The line in question indeed seems to juxtapose the concept of imaging APE1 in deep-seated tissues with a detection limit expressed in units per milliliter, which could lead to confusion. The detection limit mentioned refers to the concentration of APE1 that our afterglow nanoparticle system can accurately identify in a buffered solution (1 × NeBuffer 4) during in vitro testing.

To enhance the clarity of this statement and avoid potential confusion, we have amended the sentence as follows:

" Herein, we have developed an ultrabright afterglow nanoparticle, marking the first reported capability of imaging APE1 activity within deep-seated tissues of living animals. Additionally, in a buffered solution environment, our system significantly extends the detectable range of APE1 concentration to 0 - 4 U/mL and improves the detection sensitivity with a limit of detection of 0.0092 U/mL."

This revised sentence aims to distinctly differentiate between the in vivo imaging capabilities and in solution detection parameters of our nanoparticle system, ensuring that the context of each measurement.

8). *Introduction, line 91-95, "In this study, we designed ultra-small manganese-doped iron oxide nanoparticles ($FeMnO_x$) as dual contrast agents in both T_1 and T_2 MRI models (31, 32), significantly amplifying the signal dynamic ranges, detection range, and detection sensitivity (limit of detection: 0.16 U/mL) for APE1 for the first time." The linkage of MRI, NP and APE 1 detection is not clear.*

Response: Thank you for your constructive comment highlighting the need for a clearer explanation of the interplay between MRI, our manganese-doped iron oxide nanoparticles ($FeMnO_x$), and APE1 detection.

The novel aspect of our study is the integration of ultra-small $FeMnO_x$ nanoparticles into a core-satellite nanoprobe system for the sensitive detection of APE1 activity via both T_1 and T_2 MRI modalities. Specifically, the $FeMnO_x$ nanoparticles serve a dual

purpose. They enhance the MRI contrast, thereby improving the detection sensitivity (with a limit of detection of 0.16 U/mL for APE1), and also function as the satellite of our nanoprobe, around which the DNA strands are organized.

Upon interaction with APE1, the APE1-cleavable apurinic/apyrimidinic (AP) sites within the DNA sequence are specifically targeted by the enzyme. These AP sites are strategically located on the DNA strands that extend outward from the core-satellite structure of our APE1-probe. The enzymatic action of APE1 on these sites results in the cleavage of DNA1, which in turn triggers the release of FeMnOx@BHQ_3 from the probe structure.

The release of $FeMnO_x$ nanoparticles upon APE1 activity is a crucial step that leads to a change in the MRI signal. Dispersed $FeMnO_x$ nanoparticles induce a positive contrast in T_1-weighted MRI (increased signal brightness) while contributing to a negative contrast in T_2-weighted MRI (signal darkening). This dual-contrast response enables the precise detection and localization of APE1 activity in vivo.

We hope this revised explanation elucidates the mechanism by which our $FeMnO_x$-based nanoprobe detects APE1 and contributes to the MRI contrast changes.

9). *Introduction, line 106, how the APE1 cleavage is done, what enzyme and what happens to APE before and after is not clear. How, APE1 function and cleavage would be affected by radiation, DNA damage or ROS generation should be described.*

Response: Thank you for your suggestion regarding the need for clarity on the mechanism of APE1 cleavage and its functional implications in the context of radiotherapy.

APE1 functions as a critical enzyme in the DNA repair process known as the base excision repair (BER) pathway. It recognizes and excises apurinic/apyrimidinic (AP) sites, which are frequent lesions in DNA that lack a base. In our APE1-probe design, we incorporated these cleavable AP sites within the DNA sequence attached to the probe's nanoparticles. To facilitate efficient access of APE1 to these sites and enhance enzymatic cleavage, we ensured that the AP sites were strategically positioned away from the core-satellite structure, thus reducing steric hindrance. Upon interaction with APE1, the enzyme cleaves the DNA at the AP sites, leading to the release of $FeMnO_x$@BHQ_3. This release disrupts the afterglow resonance energy transfer (ARET) between the TA nanoparticles and $FeMnO_x$@BHQ_3, resulting in a rapid recovery of the afterglow signal. Simultaneously, this cleavage also allows $FeMnO_x$ nanoparticles to disperse, enhancing the T_1 MRI signal (increased brightness) while diminishing the T_2 MRI signal (increased darkness).

In the context of radiotherapy, X ray irradiation is employed to inflict DNA damage and generate reactive oxygen species (ROS) as part of cancer treatment. The severity of DNA damage and oxidative stress correlates with the radiation dose applied. Notably, cancer cells respond to X ray exposure by upregulating APE1 expression, which is implicated in both the repair of radiation-induced DNA damage and the modulation of the cellular redox environment. This upregulation of APE1 aids in the survival and proliferation of tumor cells, contributing to increased tumor burden and decreased radiosensitivity.

Given these insights, APE1 emerges as a valuable biomarker for assessing the efficacy of radiotherapy and potential radiation-induced toxicity. By leveraging our dual-mode APE1-probe, which combines afterglow luminescence and MRI, we aim to dynamically track the radiotherapy-induced upregulation of APE1 expression, providing a novel approach for real-time monitoring of therapeutic response and facilitating the optimization of treatment strategies.

10). *Introduction, line 110, "APE1-responsive afterglow/MRI probe" concept should be elaborated for better understanding of as DNA damage sensor model.*

Response: We appreciate your suggestion to clarify the "APE1-responsive afterglow/MRI probe" concept. APE1 is an essential enzyme in the DNA base excision repair (BER) pathway, where it identifies and processes apurinic/apyrimidinic (AP) sites—common DNA lesions that occur when a base is missing from the sugar-phosphate DNA backbone. In constructing our APE1-responsive probe, we have engineered a DNA sequence containing AP sites that can be specifically recognized and cleaved by APE1. When APE1 engages with the probe, it cleaves the DNA at these sites. This enzymatic action triggers the dissociation of $FeMnO_x$@BHQ_3 from the probe, interrupting the afterglow resonance energy transfer (ARET) mechanism between the TA nanoparticles and FeMnOx@BHQ_3. This interruption leads to a measurable recovery of afterglow luminescence. Concurrently, the

cleavage permits $FeMnO_x$ nanoparticles to disperse, which enhances the MRI T_1 signal (indicating brighter areas) and reduces the T_2 signal (indicating darker areas).

This probe's relevance is particularly pronounced in the setting of radiotherapy. During treatment, X rays induce DNA damage and generate reactive oxygen species (ROS) to combat cancer cells. The extent of this damage—and the cell's oxidative stress response is proportional to the radiation dose delivered. In response to radiation, cancer cells often upregulate APE1, which not only assists in repairing DNA damage but also modulates the intracellular redox state, aiding cell survival and potentially leading to greater radioresistance.

Therefore, APE1 serves as a crucial biomarker for evaluating the success of radiotherapy and the potential for radiation-induced side effects. Our unique APE1-responsive afterglow/MRI probe, by providing dual-mode imaging capabilities, serves as an innovative tool for the real-time monitoring of APE1 expression following radiotherapy. This approach promises to enhance our ability to assess therapeutic efficacy promptly and adjust treatment protocols as needed to optimize patient outcomes.

11). *Introduction, line 118, name of tumor model should be provided.*

Response: Thank you for bringing this to our attention. We have updated the introduction to include the specific tumor model (mice bearing subcutaneous HeLa xenograft tumors) used in our study.

12)*. Fig 1a is not clear and confusing. Showing irradiation at both sides with almost similar information is confusing. Only one side scheme should be better. In Figure legend should be self-explanatory rather than to refer to manuscript text. Same way Fig 2a scheme is also confusing. What is cleaving agent for MRI? A separate scheme for better clarity for cleavage and after flow effects (Fig. 1a, Fig 2a) should be included.*

Response: Thank you for your feedback regarding Fig.1a and 2a. We have taken your suggestions into account and have made the following revisions for clarity:

For **Fig. 1a**, we have simplified the irradiation scheme to display it on one side only, eliminating any redundancy and potential confusion. This adjustment ensures that the focus is on the key elements of the luminescence mechanism, making the figure more straightforward and easier to understand.

In the figure legend for **Fig. 1a,** we have incorporated a more detailed explanation that is self-contained, allowing the reader to grasp the concept without needing to refer back to the manuscript text. This should enhance the figure's standalone explanatory power.

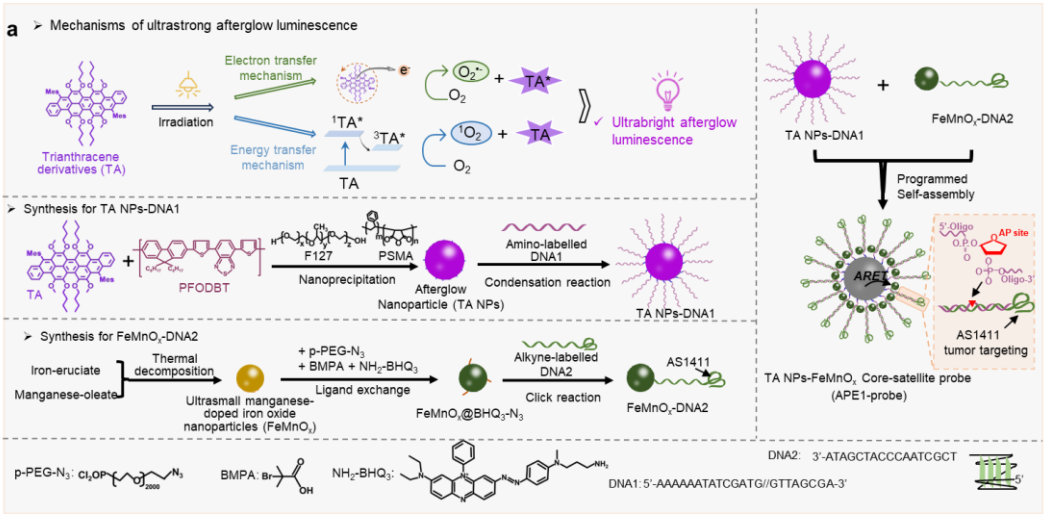

Fig. 1a. Schematic illustration for enhancing afterglow luminescent mechanisms with electron transfer and energy transfer for TA NPs and preparation of APE1-probe.

Regarding **Fig. 2a**, we have now included a distinct and clear depiction of the APE1 cleavage site on the APE1-probe. Additionally, we have provided a separate schematic that delineates the cleavage process and the resulting afterglow effects. This visual aid will offer readers a more intuitive understanding of how the APE1-probe is activated and its subsequent impact on the imaging readouts.

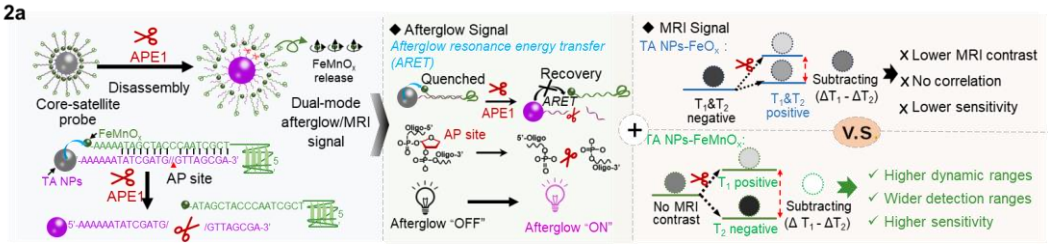

Fig. 2a Scheme illustration for APE1-activated TA NPs-$FeMnO_x$ assembly (APE1-probe) for afterglow and MRI contrast comparison between TA NPs-FeO_X and TA NPs-$FeMnO_x$ (APE1-probe).

13). *For TEM and DLS size are within same range of 32 nm. Ideally hydrodynamic size is generally bigger if some conjugation or coating is done? Authors should clarify the same.*

Response: Thank you for your comment regarding the size discrepancy between transmission electron microscopy (TEM) and dynamic light scattering (DLS) measurements.

In response to your observation, we would like to clarify the apparent discrepancy between TEM and DLS measurements for our nanoparticles. TEM provides us with the actual size of the nanoparticle core by direct visualization, which, for $FeMnO_x$ nanoparticles, was measured to be 3.4 ± 0.9 nm. Upon modification with p-PEG-N_3 and BMPA, the hydrodynamic size, as measured by DLS, increased to 9.6 ± 0.8 nm due to the addition of these molecular layers, which extend beyond the core visualized by TEM.

When FeMnOx@BHQ_3-N_3 was conjugated with alkyne-labeled DNA2, the hydrodynamic size further increased to 12.9 ± 1.1 nm, as detected by DLS. This increase is expected as the conjugation of DNA strands adds to the physical dimensions of the nanoparticle complex in solution, which is what DLS measures — the size of the entire particle including any molecules on its surface.

Similarly, for the TA NPs, the TEM-measured core diameter was 34 ± 8 nm. DLS measurements showed a slightly larger average hydrodynamic size of 37.6 ± 3.1 nm for the unmodified TA NPs in water. After DNA modification, the DLS size increased to 49.1 ± 3.7 nm, again, due to the additional molecular dimensions provided by the attached DNA strands.

Finally, the core-satellite structure of the APE1-probe (TEM size: 53.9 ± 1.4 nm), with TA NPs as the core and $FeMnO_x$ as the satellites, showed a mean hydrodynamic diameter of 83.0 ± 7.2 nm by DLS, which is reflective of the overall size of the assembled structure including the DNA linkers and the satellite particles.

In summary, the hydrodynamic size measured by DLS is larger than the core size measured by TEM due to the presence of surface modifications and molecular conjugations that extend beyond the nanoparticle core. These results are consistent with the expected increases in size upon each conjugation step and illustrate the successful synthesis and functionalization of our nanoparticles.

14)*. A quantification of recycle of on/off at different cycle (Supp Fig 8) should be included to know the magnitude of effect of recycle.*

Response: Thank you for the reviewer's suggestion regarding the quantification of the recycling efficiency of TA NPs' afterglow luminescence. In response to your comment, we have indeed performed a quantitative analysis of the signal intensity of TA NPs

from the afterglow images presented in **Supplementary Fig. 8**. This analysis aimed to assess the stability and reproducibility of the afterglow signal through successive on/off cycles.

The results of this quantification are displayed in **Fig. 1f** of the main text. Here, we have provided a clear representation of the afterglow luminescence recycling rate, demonstrating the magnitude of effect across different cycles.

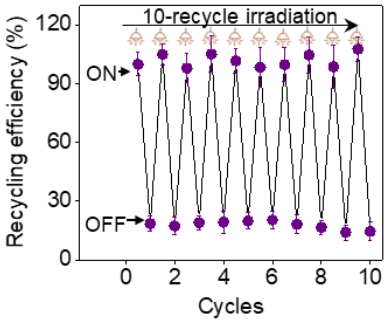

Fig. 1f. Afterglow signal intensity of TA PNs under 10-recycle recharge (20 μg/mL, n = 6). All afterglow images were obtained with a white light irradiation (10 mW/cm^2) time of 10 s and an acquisition time of 60 s. Data are means ± SD.

15)*. A quantification of Supp Fig 17 should be included*

Response: Thank you for your suggestion regarding the quantification of Supplementary Fig. 17. We have indeed provided the quantification data, and it can be found in **Fig.1p** of the main text, as initially presented in the manuscript. In the revised manuscript, we have made sure to enhance the description surrounding **Supplementary Fig. 17** to clearly direct readers to **Fig.1p** for the detailed quantification.

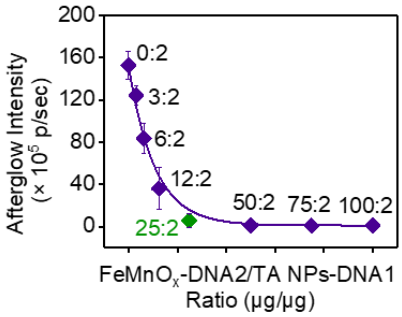

Fig. 1p. Afterglow signal intensity of TA NPs-DNA1 (10 μg/mL, n = 6) assembling with various ratio of FeMnO$_x$-DNA2. All afterglow imaging were obtained with a whit light irradiation (10 mW/cm^2) time of 10 s and an acquisition time of 60 s. Data are means ± SD.

16)*. Line 227, why 12.5:1 ratio was chosen in Suppl Fig 17, signal is not visible. A rationale of selecting ratio should be mentioned in the text.*

Response: Thank you for addressing the concern regarding the choice of the 12.5:1 (25:2) ratio of FeMnOx-DNA2 to TA NPs-DNA1 in **Supplementary Fig.17** and the lack of signal visibility.

In our revised manuscript, we have clarified the rationale behind selecting this specific assembly ratio. The choice was primarily guided by the spectral overlap between the absorption of FeMnO$_x$@BHQ$_3$ and the afterglow luminescence emission of TA NPs, as depicted in **Fig. 1m**. The proximity of FeMnO$_x$ to the TA NPs facilitates the quenching of the afterglow signal through afterglow resonance energy transfer (ARET) with the BHQ$_3$ molecules (**Fig. 1n**). To elucidate this quenching effect, we investigated the afterglow signal intensity of TA NPs-DNA1 both before and after the addition of FeMnO$_x$-DNA2. The results showed a substantial quenching of the TA NPs' afterglow luminescence by approximately 95.0 ± 3.0 % due to the BHQ3 molecules (**Fig. 1o**).

Importantly, this quenching is advantageous as it minimizes the initial afterglow signal, thereby enhancing the signal-to-noise ratio and extending the dynamic range of detection. We conducted a systematic optimization to identify the ideal assembly ratio that

would yield the most significant quenching while still allowing for effective signal recovery upon APE1 activation. The optimization process, as shown in F**ig.1p** and **Supplementary Fig. 17**, indicated that increasing the ratio of $FeMnO_x$-DNA2 to TA NPs-DNA1 led to a decrease in the afterglow signal. No obvious afterglow signal (at 25 μg $FeMnO_x$-DNA2 /2 μg TA NPs-DNA1ratio) indicated the most significant quenching. Based on these observations, we selected the 25 μg $FeMnO_x$-DNA2 /2 μg TA NPs-DNA1ratio ratio of FeMnOx-DNA2 to TA NPs-DNA1 for the preparation of the APE1-probe used in subsequent experiments.

We have now included a detailed explanation of this optimization process in the text and highlighted the necessary information to ensure that the selection of the assembly ratio is transparent and justified.

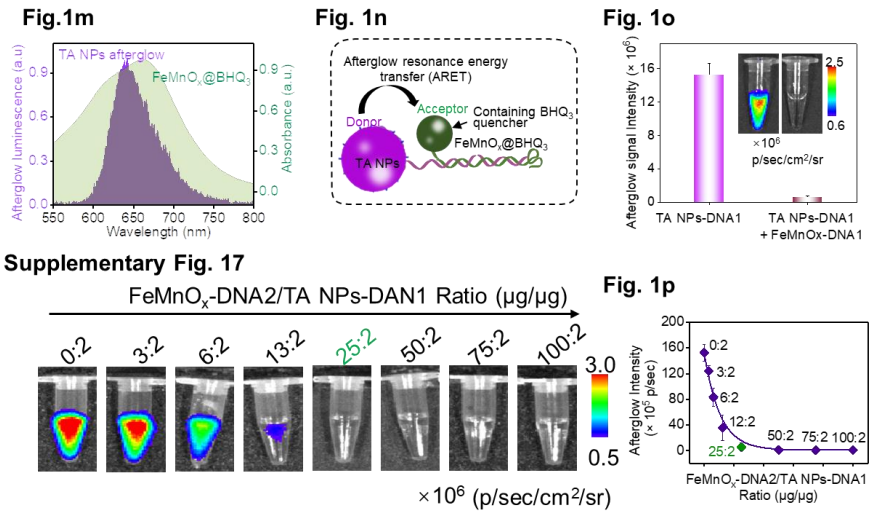

Fig. 1m Overlap of TA NPs-DNA1's afterglow luminescence spectrum and BHQ_3's absorption spectrum. **Fig. 1n** Schematic illustration for the afterglow resonance energy transfer (ARET) between TA NPs donor and BHQ_3 quencher. **Fig. 1o** Afterglow images and signal intensity of TA NPs-DNA1(20 μg/mL) before and after assembling with $FeMnO_x$-DNA2 (10 mW/cm^2, irradiation time of 10s, acquisition time of 60 s, n = 3). **Supplementary Fig. 17 and Fig. 1p.** Afterglow images and afterglow signal intensity of TA NPs-DNA1 (10 μg/mL) assembling with various ratio of $FeMnO_x$-DNA2 (10 mW/cm^2, irradiation time of 10 s, acquisition time of 60 s, n = 6). Data are means ± SD

17)*. Line 271, the significance and p value for detection limit should be mentioned out of multiple experiments;*

Response: Thank you for your attention to detail and for emphasizing the importance of statistical validation in our findings. In response to your suggestion, we have performed the necessary statistical analyses to determine the p-values associated with the detection limits obtained from our experiments. These p-values provide the statistical significance of our detection limits, reinforcing the robustness of our assay.

We have now incorporated these p-values into the main text where the detection limits are discussed. Moreover, we have meticulously reviewed the entire manuscript to ensure that all key experimental outcomes are accompanied by their respective p-values. This additional layer of statistical information has been carefully calculated and is now clearly presented within the relevant sections of the manuscript, with the changes distinctly highlighted for easy reference.

18). *Fig 3j, cell number used is too high 0.5-2 ×10^7. Why so high concentration of cells was used? That shows poor sensitivity of materials in the cells. How much is the uptake and what is the uptake kinetics? The normal cell data should be also provided for comparison. Why there is increase with respect of cell number, where it is due to background signal. From control to irradiated, increase seems to be not statistically significant. Statistical significance should be provided. Same comment is applicable for Fig 3m.*

Response: Thank you for your insightful comments. The choice of cell concentration in our experiments was indeed higher than typically used for such assays. The rationale behind using a cell number ranging from 0.5 to 2 × 10^7/cells/mL was to ensure

detectable afterglow and MRI signals at the low APE1-probe concentration of 10 μg/mL. This approach was adopted to reflect a more conservative and potentially relevant probe concentration while ensuring adequate signal for detection.

In response to your queries about uptake and uptake kinetics, we conducted a detailed analysis. HeLa cells were exposed to a 6 gray dose of radiation and subsequently incubated with the APE1-probe. The cells were prepared for ICP-MS analysis at various time points to quantify $FeMnO_x$ uptake. As depicted in **Supplementary Fig. 31**, the intracellular concentration of the APE1-probe increased over time, which indicates a rapid uptake rate and suggests a promising cellular internalization capability for the APE1-probe.

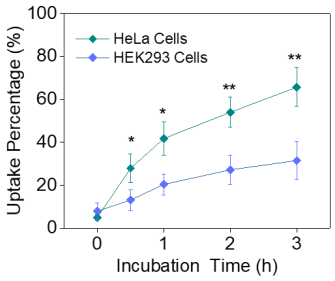

Supplementary Fig. 31 Quantification of uptake percentage of APE1-probe into two types of cells (HeLa cells and HEK293 cells) after radiation (6 grays). Afterglow imaging was obtained with white light irradiation (10 mW/cm^2) time of 10 s and acquisition time of 60 s. Data are means ± SD. Statistical differences were analyzed by student's t test, *p < 0.05, **p < 0.01, n = 3.

We conducted additional experiments using HEK-293 cells as a non-cancerous cell line control. These cells were also subjected to varying doses of radiation and treated with the APE1-probe. The subsequent afterglow imaging revealed that the signal intensity from radiation-treated cells from cancer cells was higher compared to normal cells (**Supplementary Fig. 29**), which suggests that the observed signal is not merely background noise but correlates with radiation-induced APE1 expression.

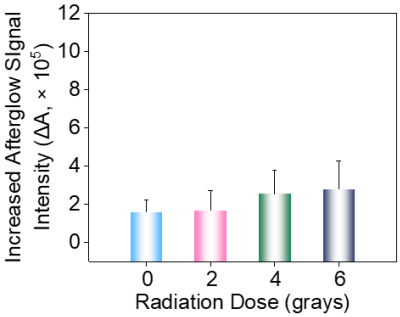

Supplementary Fig. 29. Afterglow intensity of HEK293 cell (1 ×10^7 cell/mL) incubated with APE1-probe (10 μg/mL) for 4 hours after radiation treatment (0, 2, 4, and 6 grays, respectively, n = 4). Afterglow imaging was obtained with a white light irradiation (10 mW/cm^2) time of 10 s and an acquisition time of 60 s. Data are means ± SD.

Regarding statistical significance, we have now included statistical analysis for **Fig. 3j** and **3m**. These analyses confirm that the differences observed are statistically significant, providing robust support for the conclusions drawn from the data.

Fig. 3j **Fig3m**

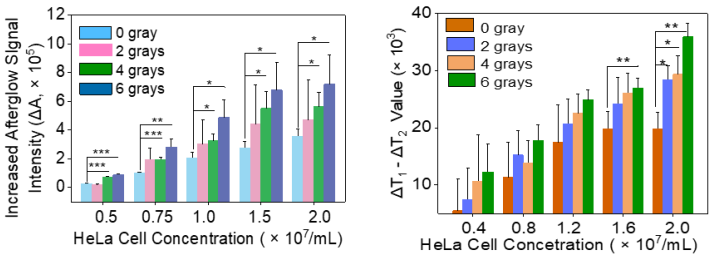

Fig. 3j Afterglow signal intensity of a various number of HeLa cells treated with various doses of radiation (0, 2, 4, and 6 grays) and then incubated with APE1-probe (n = 3). **Fig. 3m** Subtracted MRI signal intensity (ΔT_1 - ΔT_2 value) of a various number of HeLa cells treated with various doses of radiation (0, 2, 4, and 6 gray) and then incubated with APE1-probe, for afterglow/ MRI imaging (n = 3). All afterglow images were obtained with a whit light irradiation (10 mW/cm^2) time of 10 s and an acquisition time of 60 s. Data are means ± SD. Statistical differences were analyzed by student's t test, *p<0.05, **p<0.01, ***p<0.001.

19). *Fig 3o, statistical significance should be provided.*

Response: Thank you for your recommendation regarding the inclusion of statistical significance in **Fig.3o**. In response to your suggestion, we have now incorporated the statistical analysis into **Fig. 3o.** The p-values derived from appropriate statistical tests have been added to the figure to quantify the significance of the observed differences. Furthermore, we have conducted a comprehensive review of the entire manuscript and have ensured that all relevant figures now contain the statistical significance data where necessary.

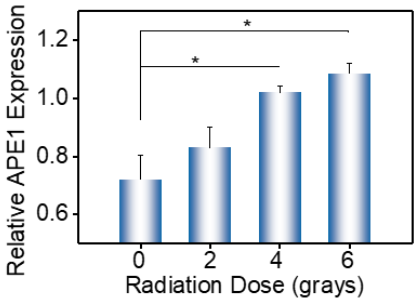

Fig. 3o Western bolting determination and quantified APE1 level of the Hela cells at post-treatment of 2 hours under various radiation doses (n = 2). Afterglow imaging was obtained with white light irradiation (10 mW/cm^2) time of 10 s and acquisition time of 60 s. Data are means ± SD. Statistical differences were analyzed by student's t test, *p<0.05.

20)*. Without statistical significance, statement (line 394-395) "Especially, at cell number of 2 × 10^7, the afterglow signal intensity was increased by 2.0-fold for 6 Gray, 1.6-fold for 4 Gray, and 1.3-fold for 2 Gray, compared to 0 Gray." has no meaning.*

Response: Thank you for your comment on the need for statistical significance in the interpretation of our results. We have taken your suggestion into consideration and performed a statistical analysis on the data presented in **Fig. 3j**. The results now include p-values calculated using appropriate statistical tests to establish the significance of the differences in afterglow signal intensity observed at varying cell numbers and radiation doses. These p-values have been added to the figure to provide a quantitative measure of significance.

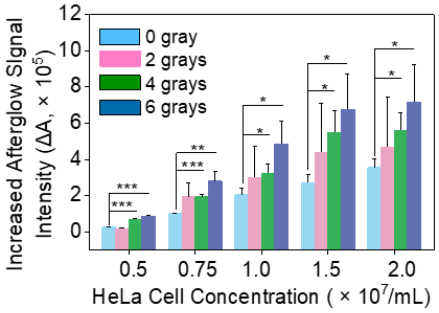

Fig. 3j Afterglow signal intensity of various number of Hela cells treated with various doses of radiation (0, 2, 4, and 6 grays) and then incubated with APE1-probe (n = 3). Afterglow imaging was obtained with a white light irradiation (10 mW/cm^2) time of 10 s and an acquisition time of 60 s. Data are means ± SD. Statistical differences were analyzed by student's t test, **p* < 0.05, ***p* < 0.01, ****p* < 0.001.

21)*. A time kinetics for afterglow effect and expression of APE1 in HeLa cells after irradiation should be shown.*

Response: Thank you for your suggestion regarding the need for kinetic data on the afterglow effect and APE1 expression in HeLa cells post-irradiation. In response to your recommendation, we have conducted a time-course study to investigate the afterglow effect and APE1 expression dynamics following radiation exposure. HeLa cells were cultured in a 6-well plate for 24 hours and subsequently exposed to a 6 gray radiation dose. After a 2-hour post-irradiation period, the cells were treated with the APE1-probe at a concentration of 10 μg/mL TA NPs for varying durations: 0.5, 1, 2, 4, and 6 hours. Post-treatment, the cells were harvested, accurately counted, and resuspended to a uniform concentration of 1.0 × 10^7 cells/mL for afterglow imaging. As a control, cells that did not receive radiation but were processed using the same protocol were also imaged.

The results, which are presented in the **Supplementary Fig.30**, show that the afterglow luminescence signal in the radiation-treated cells increased from 0.5 to 4 h. This observation suggests that the APE1-probe is effectively activated by intracellular APE1 in the radiation-treated cells. This finding indicates that radiation exposure leads to an upregulation of intracellular APE1 expression, validating the potential of our APE1-probe for use in monitoring cellular responses to radiation therapy.

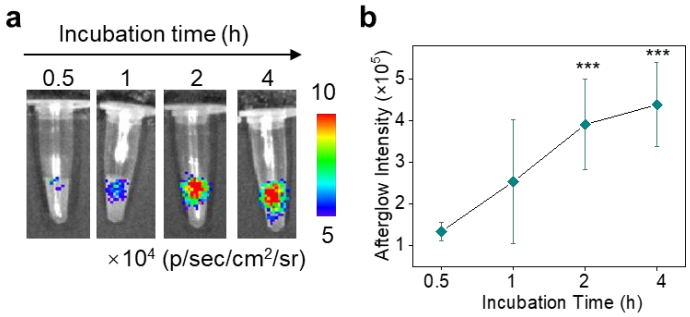

Supplementary Fig 30. Afterglow imaging of the HeLa cell with radiation treatment (6 grays) and then incubated with APE1-probe for various time. (a) Afterglow images. (b) Quantification of afterglow signal intensity (a) (n = 6). Afterglow imaging was obtained with a white light irradiation (10 mW/cm^2) time of 10 s and an acquisition time of 60 s. Data are means ± SD. Statistical differences were analyzed by student's t test, ****p* < 0.001.

Related experimental methods:

Determination of time-dependent afterglow imaging of HeLa cells. To detect the time-dependent afterglow imaging, HeLa cells were seeded into a 6-well plate for 24 hours, and then the cells were treated with 6 grays of radiation. After 2 hours, the treated cells were incubated with APE1-probe (containing 10 μg/mL TA NPs) for various time (0.5, 1, 2 4, and 6 hours). The cells from different time were collected after DPBS washing, counted, and diluted to specific concentrations (1.0 × 10^7 cells/mL) for afterglow imaging (10 mW/cm^2, irradiation time: 10 s, and acquisition time: 60 s).

22). *What is difference between Fig 4b and Fig 4c. Even Figure legend it is not clear.*

Response: Thank you for the opportunity to clarify the distinction between **Fig. 4b** and **Fig. 4c** in our manuscript. We have revised the figure legends to better delineate the differences between the two images. **Fig. 4b** presents the afterglow imaging of mice following an intravenous injection of the non-targeted APE1-probe, while **Fig. 4c** displays the corresponding fluorescence imaging under similar conditions.

To elucidate the signal-to-noise ratio between the afterglow and fluorescence imaging modalities, we administered the non-targeted APE1-probe, which lacks the tumor-targeting AS1411 aptamer, to mice bearing subcutaneous HeLa xenograft tumors. As indicated in both **Fig. 4b and Fig. 4c**, there was an observable increase in signal at the tumor sites, validating the tumor-targeted imaging capability of the APE1-probe. A comparative analysis between the afterglow and fluorescence images (as shown in **Fig. 4b, c,** and **Supplementary Fig. 33a, 35a**) revealed that the afterglow imaging modality demonstrated a superior signal-to-noise ratio (Fig. 4i). This comparison underscores the advantage of afterglow imaging in providing clearer visualization with less background interference, thereby highlighting its potential utility in biomedical imaging applications.

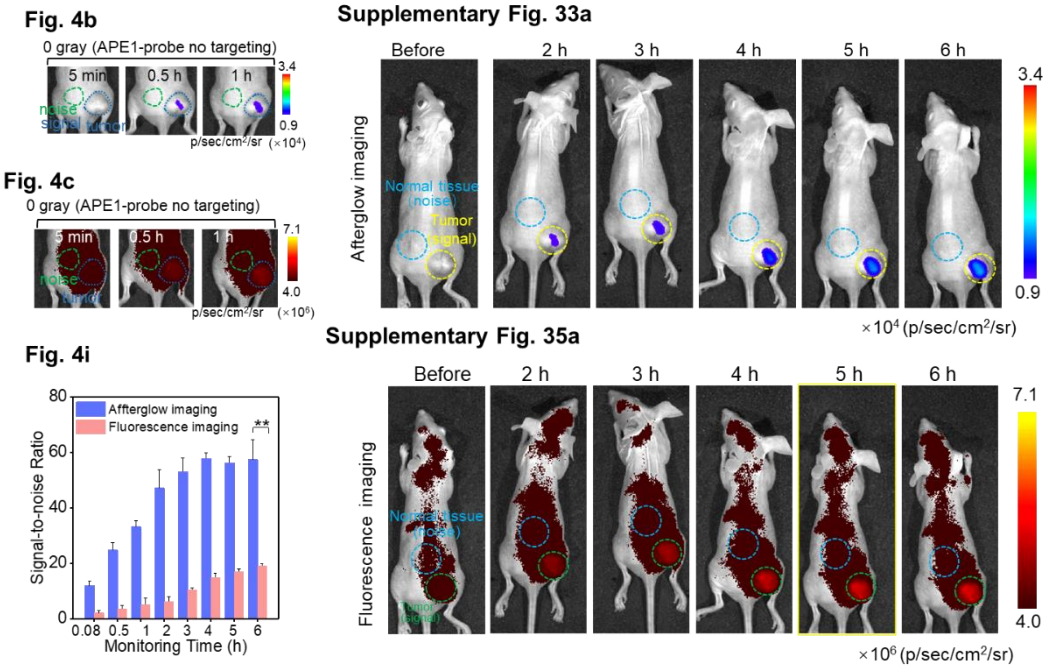

Fig. 4b and Supplementary Fig. 33a Afterglow imaging of mice without any radiation treatment (0 gray) and with intravenously injection of APE1-probe (no targeting) (120 μL, 80 μg/mL) at different periods (10 mW/cm^2, irradiation time of 10 s, acquisition time of 60 s). **Fig. 4c** and **Supplementary Fig. 35a** Fluorescence images of mice without any radiation treatment (0 gray) and with intravenously injection of APE1-probe (no targeting) (120 μL, 80 μg/mL) at different periods (excitation wavelength of 605 nm; emission in Cy5.5 channel, n = 3). **Fig. 4i** Signal-to-noise ratio of afterglow imaging and fluorescence imaging of the mice intravenously injected with APE1-probe (no targeting). All afterglow imaging were obtained with white light irradiation (10 mW/cm^2) time of 10 s and acquisition time of 60 s. Fluorescence imaging was obtained with excitation wavelength of 605 nm and emission of Cy5.5 channel. Data are means ± SD. Statistical differences were analyzed by student's t test, **p<0.01.

23)*. For sham irradiated (0 Gy) targeting and non-targeting with or without AS1411 aptamer data provided for not for irradiated (Fig 4e,f,g). Non-targeted for irradiated groups should be also provided.*

Response: Thank you for the suggestion to include data for non-targeted APE1-probe in irradiated groups. We have conducted an additional set of experiments to ensure our study comprehensively covers the imaging effects of both targeted and non-targeted APE1-probe on mice with subcutaneous HeLa xenograft tumors that underwent in-situ radiation treatment with a dose of 6 gray.

Following the radiation treatment, we administered the non-targeted APE1-probe intravenously (120 μL at a concentration of 80 μg/mL TA NPs) to the irradiated mice. We then employed the IVIS Spectrum imaging system (Lumina XR) to perform afterglow imaging under the conditions of no excitation wavelength, 10 seconds of light irradiation, and 60 seconds of acquisition time.

The resulting afterglow images, which have been added to **Supplementary Fig. 36** in our manuscript, display a discernible increase in afterglow luminescence at the tumor sites post-injection with both the non-targeted and targeted APE1-probe. A comparative analysis of the afterglow images reveals that tumors administered with the targeted APE1-probe exhibited higher afterglow luminescence intensity than those receiving the non-targeted probe at various time points post-injection (**Supplementary Fig. 34e and 34e**). These results clearly demonstrate the tumor-targeting capabilities of the APE1-probe and enhance the robustness of our findings by showing the differential imaging effects of targeted versus non-targeted probes in irradiated tumor models.

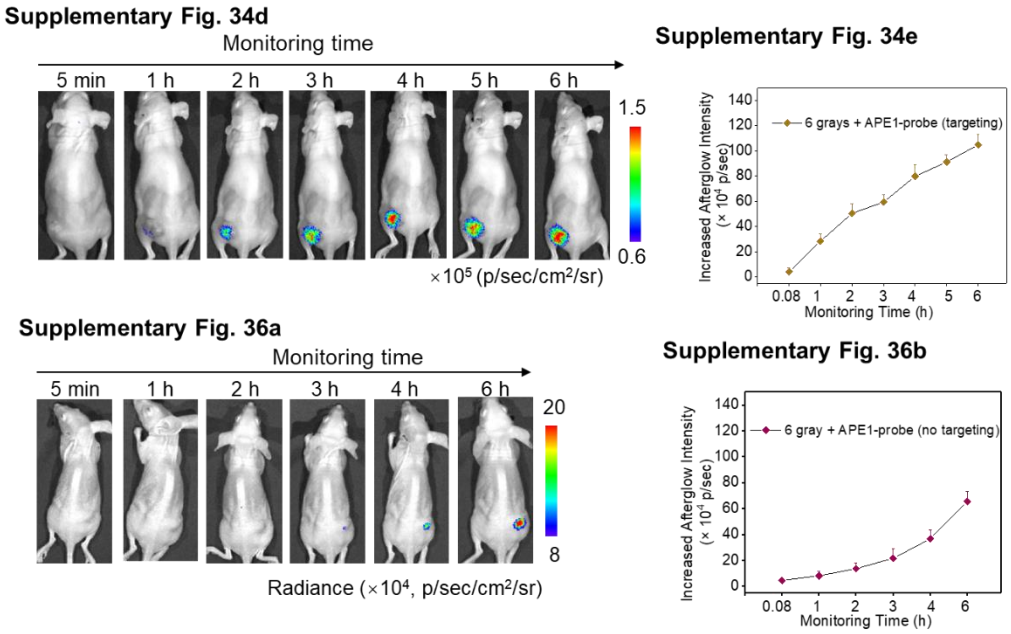

Supplementary Fig. 34d and 34e. Afterglow images and quantification of signal intensity of the mice with injection of APE1-probe (targeting) after radiation treatment (6 grays). **Supplementary Fig. 36a and 36b.** Afterglow images and quantification of signal intensity of the mice with injection of APE1-probe (no targeting) after radiation treatment (6 grays) (n = 3). Afterglow imaging was obtained with white light irradiation (10 mW/cm^2) time of 10 s and acquisition time of 60 s. Data denote mean ± SD.

Related experimental methods:

Afterglow and fluorescence imaging for tumor with injection of APE1-probe (targeting and no targeting) in vivo. To evaluate the targeting imaging of the probe in vivo, mice bearing subcutaneous HeLa xenograft tumors were treated with various doses of radiation in situ (6 grays). After 2 hours, the mice were intravenously injected with APE1-probe (containing tumor-targeting AS1411 aptamer) or APE1-probe (no targeting, un-containing the tumor-targeting AS1411 aptamer) (120 μL, containing 80 μg/mL TA NPs). Afterglow imaging of the mice was performed using an IVIS Spectrum imaging system (Lumina XR) with no excitation wavelength, light irradiation of 10 s (10 mW/cm^2), and acquisition time of 60 s.

24). *For APE1-activated afterglow/MRI imaging for cancer cells experiments, whether cells were collected by trypsinization? A data with or without washing should be shown.*

Response: Thank you for your suggestion regarding the afterglow/MRI imaging protocol for cancer cells. Those cells were indeed digested by trypsinization. Upon your recommendation, we have included an additional step in our experimental procedure to compare the afterglow imaging results of APE1-probe-incubated cells with and without a washing step.

For this comparison, HeLa cells were cultured in a 6-well plate for 24 hours and subjected to a 6 grays radiation dose. Two hours post-irradiation, the cells were treated with the APE1-probe (containing 10 μg/mL of TA NPs) for specified durations of 0 and 4 hours. Subsequently, the cells were harvested via trypsinization. One set of cells was washed three times with PBS, pelleted, and resuspended to a concentration of 1.0×10^7 cells/mL for afterglow imaging. The control set consisted of cells that, after incubation with the probe for 4 hours, were also trypsinized but were not subjected to the DPBS wash.

According to **Supplementary Fig. 28**, the imaging results indicated that the cells which underwent the DPBS washing displayed an increase in afterglow signal ratio compared to the unwashed cells. This suggests that the washing step effectively removes unbound probes, which could otherwise contribute to background signal and potentially confound the imaging analysis. These findings have been incorporated into the revised manuscript, providing a clearer depiction of the probe's specificity and enhancing the overall robustness of the imaging results.

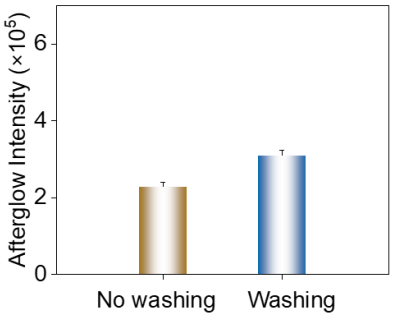

Supplementary Fig. 28 Afterglow imaging and quantification of signal intensity of the cell (1×10^7 cells/mL) treated with APE1-probe (10 μg/mL) for 4 hours and then with washing or not after radiation (6 grays) (n =4). Afterglow signal was obtained with white light irradiation (10 mW/cm^2) time of 10 s and acquisition time of 60 s. Data are means ± SD.

Related experimental methods:

Afterglow imaging comparison of APE1-probe-incubated HeLa cells before and after washing. To compare the afterglow imaging difference from APE1-probe-incubated cells with washing or not, HeLa cells were seeded into a 6-well plate for 24 hours, and then the cells were treated with radiation (6 grays). After 2 hours, the treated cells were incubated with APE1-probe (containing 10 μg/mL TA NPs) for 4 hours. The cells were collected after DPBS washing, and counted to specific concentrations (1.0×10^7 cells/mL) for afterglow imaging. In contrast, the cells were collected without DPBS washing, counted to specific concentrations (1.0×10^7 cells/mL) for afterglow imaging was used as the controls.

25). *A time kinetics of update of NP in cells and suitable control should be shown.*

Response: Thank you for addressing the request for kinetic data on the uptake of nanoparticles (NPs). In response to the comment, we performed a time-course study to investigate the uptake kinetics of the APE1-probe by HeLa cells, which had been exposed to a radiation dose of 6 grays. We employed Inductively Coupled plasma mass spectrometry (ICP-MS) to accurately measure the internalization of $FeMnO_x$ over several time points. The data, which are presented in **Supplementary Fig. 31**, reveal that the uptake of the APE1-probe by the cells increases progressively from 0 to 3h. This suggests a rapid and efficient internalization process.

Furthermore, to establish a meaningful comparison, we included HEK-293 cells, a non-cancerous cell line, to serve as a control group. The results demonstrated that the uptake of NPs in the cancerous HeLa cells was significantly higher than that in the normal HEK-293 cells. This differential uptake not only underscores the APE1-probe's preferential internalization by cancer cells but also reinforces its potential as a targeted imaging agent.

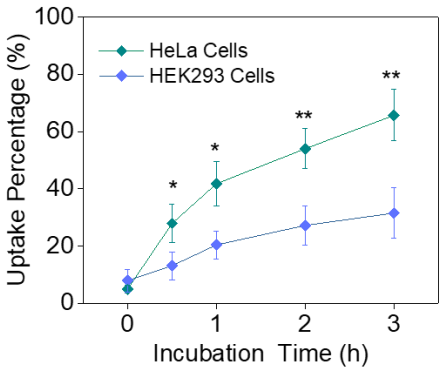

Supplementary Fig. 31 Quantification of uptake percentage of APE1-probe into two types of cells after radiation (6 gray) (n = 3). Afterglow signal was obtained with white light irradiation (10 mW/cm^2) time of 10 s and acquisition time of 60 s. Data are means ± SD. Statistical differences were analyzed by student's t test, *p < 0.05, **p < 0.01.

Related experimental methods:

Determination of the time kinetics of update of probe in cells. To detect the time kinetics of update of nanoparticle in cells, HeLa cells and HEK293 cells were seeded into a 48-well plate for 24 hours, and then the cells were treated with 6 grays of radiation. After 2 hours, the treated cells were incubated with APE1-probe (containing 10 μg/mL TA NPs) for various time (0, 0.5, 1, 2 3, and 4 hours, respectively). The cells from different time were collected, counted, and diluted for Inductively Coupled Plasma Mass Spectrometry (ICP-MS) measurement to detect the internalization of $FeMnO_x$ over several time points.

26)*. How radiation treatment was given, which irradiator type of radiation, energy and dose rate should be mentioned. For local irradiation whether any shielding devise was used.*

Response: Thank you for raising these essential points about our radiation treatment protocols.

In our study, radiation treatments were meticulously delivered using an RS 2000 X-ray Biological Irradiator (225 KV, 8 mA), which allowed for precise dose rate control. The settings used were calibrated to administer specific doses: 121 seconds for 2 grays, 241 seconds for 4 grays, and 363 seconds for 6 grays, with these durations confirmed by radiation dosimetry to ensure accuracy.

For the experiments involving afterglow/MRI imaging and tumor radiotherapy, the X-ray energy was carefully adjusted to target the tumor sites directly with the designated doses of 0, 2, 4, and 6 grays, ensuring focused irradiation.

In the assessment of radiation-induced liver injury, we irradiated the liver region of mice, which did not have xenograft tumors, with X-ray energy doses ranging from 0 to 6 gray. During these procedures, we employed a lead shield to protect the rest of the body, thus isolating the liver region.

Moreover, to investigate the radiation-induced abscopal effect, we used a dual-sided subcutaneous HeLa xenograft tumor model in mice. Group 1 received a localized radiation treatment of 6 grays on the right tumor, while the contralateral left tumor was protected with a lead shield to observe any systemic effects of localized radiation.

27). *MEHPPV-based nanoparticles were used for comparison of formulation. What the rationale to select the same.*

Response: Thank you for your inquiry regarding our choice of MEHPPV-based nanoparticles for comparison in our study. MEHPPV, or poly[2-methoxy-5-(2'-ethylhexyloxy)-1,4-phenylene vinylene], is a widely recognized semiconducting polymer that has been extensively documented as an organic afterglow material in many seminal publications (*Nat. Biotechnol.* **2017**, 35, 1102-1110; *Nat. Commun.* **2020**, 11, 446; *Chem. Soc. Rev.* **2019**, 48, 38-71, *Nat Commun.* **2019**, 10, 2064. *Nat. Biomed. Eng.* **2023**, 7, 298–312). Its frequent utilization in research makes it a standardized reference, providing a benchmark for evaluating new afterglow materials.

The choice of MEHPPV-based nanoparticles as a comparator is further justified by their favorable properties for biomedical use. Their biocompatibility and potential for biodegradability align with the requirements for in vivo applications, making them an appropriate model for assessing the biological suitability of our TA-NPs.

Additionally, the optical properties of MEHPPV, including its absorption and fluorescence spectra, are closely aligned with those of our TA-NPs. This resemblance in spectral characteristics ensures that the comparison between MEHPPV-based nanoparticles and TA-NPs is relevant and meaningful, providing a direct assessment of afterglow performance under comparable conditions.

28). *How the synthesis of NPs and conjugation of bonds at different steps were characterized?*

Response: Thank you for your inquiry regarding the characterization of nanoparticle synthesis and bond conjugation at different stages of our study. We utilized a variety of analytical techniques to ensure that each step of the nanoparticle synthesis and subsequent bond conjugation was conducted successfully. Here is a more detailed account of the methods we employed:

We synthesized afterglow nanoparticles (TA NPs) through one-step nanoprecipitation (**Fig. 1a**). The as-prepared TA NPs had a mean diameter of 34 ± 8 nm, as determined by transmission electron microscopy (TEM) images (**Fig. 1b**). The average hydrodynamic size of TA NPs in water was measured to be 37.6 ± 3.1 nm with zeta potential of -18 ± 0.8 mV (**Supplementary Fig. 1**).

Fig. 1a

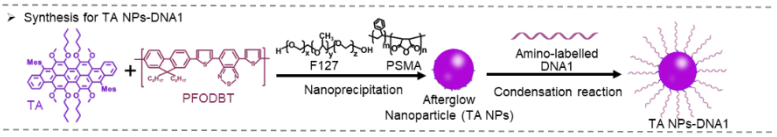

Fig. 1b

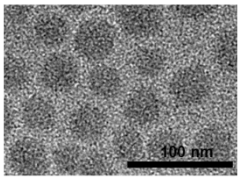

Supplementary Fig. 1a

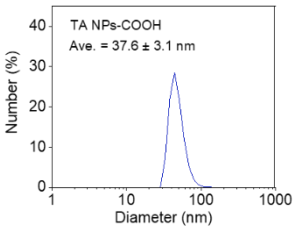

Supplementary Fig. 1b

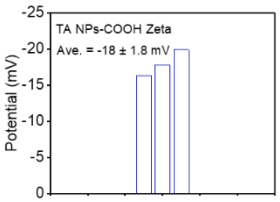

Fig.1a Schematic illustration for preparation of afterglow nanoparticles (TA NPs). **Fig.1b** TEM images of TA NPs. **Supplementary Fig. 1a** DLS measurement at water condition of TA NPs. **Supplementary Fig. 1b** Zeta potential of TA NPs. Data are means ± SD.

Next, we modified TA NPs with amino-labeled DNA1 through a cross-linking reaction involving amino and carboxyl groups (**Fig. 1a**). The successful preparation of TA NPs-DNA1 was confirmed by the enhanced absorption intensity of DNA1 at 260 nm compared to free TA NPs-COOH (**Supplementary Fig. 9**). Additionally, the dynamic light scattering (DLS) analysis revealed an increase in the diameter to 49.1 nm ± 3.7 nm (**Supplementary Fig. 10**).

Supplementary Fig. 9

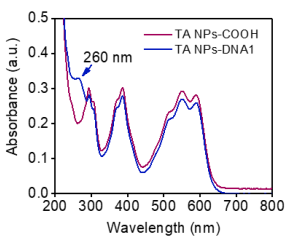

Supplementary Fig. 10a

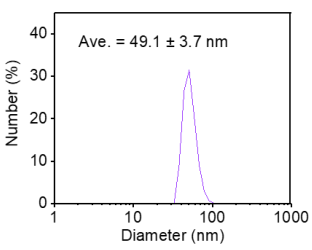

Supplementary Fig. 10b

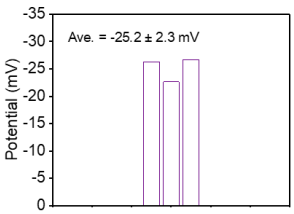

Supplementary Fig. 9 Absorption spectra of TA NPs before and after conjugating with DNA1. **Supplementary Fig. 10a** Characterization of (a) DLS measurement at water condition of TA NPs-DNA1. (Insert: photograph image). **Supplementary Fig. 10b** Zeta potential of TA NPs-DNA1. Data are means ± SD.

Ultrasmall $FeMnO_x$ was prepared through thermal decomposition using iron-eructate and manganese-oleate. The TEM images revealed that the as-synthesized $FeMnO_x$ had a mean diameter of 3.4 ± 0.9 nm (**Fig. 1i**). Subsequently, FeMnOx was modified with phosphorylated/azide-polyethylene glycol (p-PEG-N_3) and 2-bromo-2-methylpropanoic acid (BMPA) through a ligand exchange process to yield $FeMnO_x$-N_3, which was further modified with amino-modified BHQ_3 quencher molecules (H_2N-BHQ_3) to form FeMnOx@BHQ_3-N_3 (**Fig. 1a**). The successful preparation resulted in the transformation of hydrophobic $FeMnO_x$ (yellow color) into hydrophilic $FeMnO_x$@BHQ-N_3 (green color) (**Supplementary Fig. 13**). FeMnOx@BHQ_3-N_3 exhibited noticeable absorbance of BHQ_3 at the wavelength of 600 nm, with an average hydrodynamic diameter of 9.6 ± 0.8 nm and a potential of -14 ± 0.2 mV.

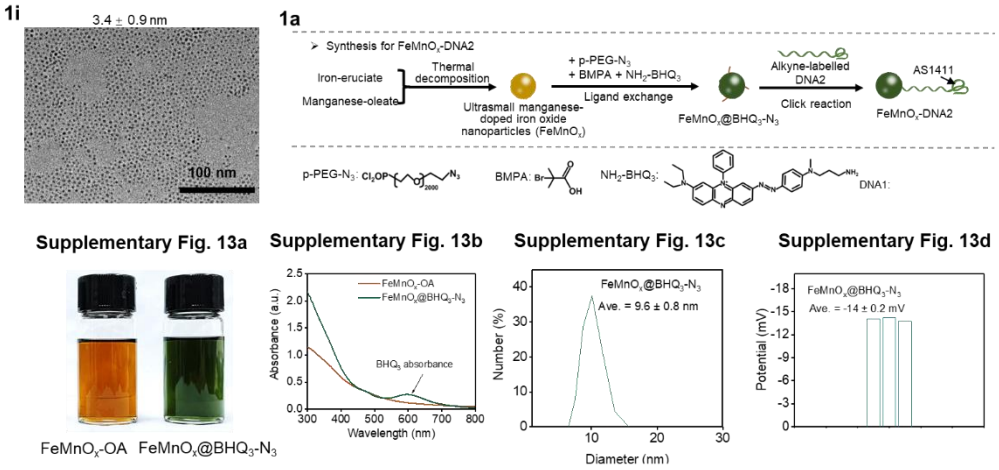

Fig. 1i TEM images of $FeMnO_x$. **Fig.1a** Schematic illustration for preparation of $FeMnO_x$-DNA2. **Supplementary Fig. 13a** Photographs images of $FeMnO_x$ (containing (0.31 mg/mL, Fe + Mn) before and after conjugating with NH_2-BHQ_3 and p-PEG-N_3. **Supplementary Fig. 13b** Absorbance spectra of FeMnOx and $FeMnO_x$@BHQ_3-N_3. **Supplementary Fig. 13c** DLS measurement of $FeMnO_x$@BHQ_3-N_3 at water condition. **Supplementary Fig. 13d** Zeta potential of FeMnOx@BHQ_3-N_3. Data are means ± SD.

Subsequently, FeMnOx@BHQ_3-N_3 was conjugated with alkyne-labeled DNA2 (alkyne-DNA2) through the click reaction, resulting in the formation of DNA2-functionalized $FeMnO_x$@BHQ_3-N_3 ($FeMnO_x$-DNA2) (**Fig. 1a**). The successful preparation of $FeMnO_x$-DNA2 was confirmed by an increase in the DLS size to 12.9 ± 1.1 nm and a decrease in zeta potential to -16.1 ± 1.4 mV (**Supplementary Fig. 14**).

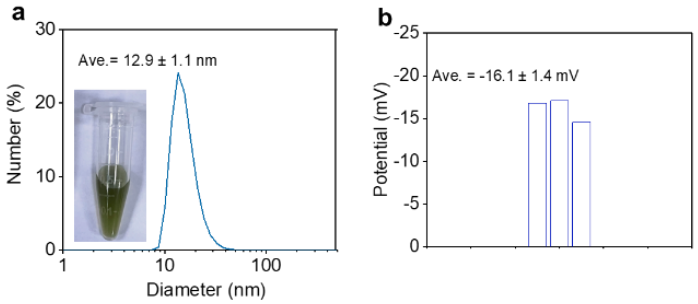

Supplementary Figure 14. Characterization of $FeMnO_x$ conjugation with DNA2 ($FeMnO_x$-DNA2). (a) DLS measurement (Insert:

photograph images, 0.25 mg/mL, Fe + Mn). (b) Zeta potential. Data are means ± SD.

Based on the hybridization of DNA1 and DNA2, we assembled TA NPs-DNA1 with $FeMnO_x$-DNA2 to form the core-satellite assembly of TA NPs and $FeMnO_x$, named APE1-probe (**Fig. 1a and Supplementary Fig. 15**). The successful preparation of APE1-probe was verified through TEM images, which revealed a core-satellite structure where afterglow NPs served as the core and multiple $FeMnO_x$ acted as satellites attached closely to the surface of TA NPs (**Fig. 1l**). The DLS analysis determined an average diameter of 83.0 ± 7.2 nm and a potential of -37 ± 2.6 mV (**Supplementary Fig. 16**).

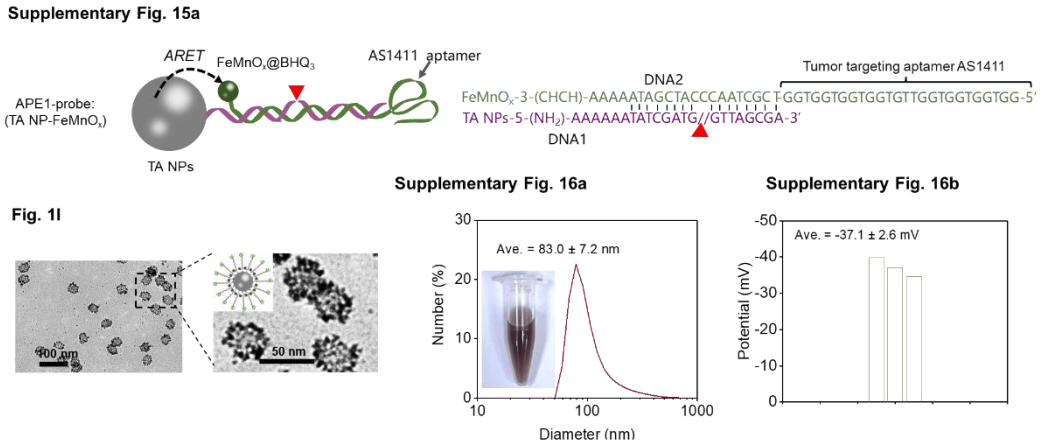

Supplementary Fig. 15a Schematic illustration for the structures and DNA sequence of TA NP-$FeMnO_x$ (APE1-probe). **Fig. 1l** TEM images of TA NPs-$FeMnO_x$ assembly (APE1-probe). **Supplementary Fig. 16a** DLS measurement of TA NPs-DNA1 and $FeMnO_x$-DNA2 assembly (APE1-probe) (Insert: photograph image, containing 50 μg/mL TA NPs) in DPBS (n = 3). **Supplementary Fig. 16b** Zeta potential of APE1-probe (n = 3). Data are means ± SD.

29). *Suppl Fig 17, quantification of images should be done and graphically represented. Whether Fig 1p is quantification of Suppl Fig 17. The ratio values shown in Suppl figure is different than Fig 1p. Clarify*

Response: Thank you for pointing out the discrepancy between the ratio values in **Supplementary Fig. 17** and those presented in **Fig. 1p**. Upon reevaluation of the data, we have ensured that the quantification of the images in **Supplementary Fig. 17** has been accurately reflected in the graphical representation provided in **Fig 1p**. We have revised our labeling method to maintain consistency across figures, thereby aligning the ratio values presented in the **supplementary Fig.17** with those in the main **Fig. 1p**. We believe this amendment clarifies the issue and we appreciate your attention to detail in this matter.

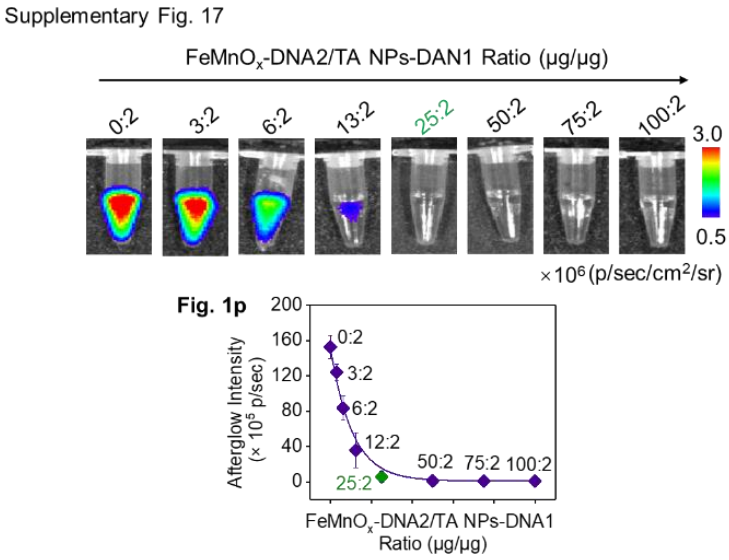

Supplementary Fig. 17 Afterglow images of TA NPs-DNA1 assembling with various ratios of $FeMnO_x$-DNA2. (10 μg/mL, 10 mW/cm^2, irradiation time: 10 s, acquisition time: 60 s, n = 3). **Fig. 1p** Afterglow signal intensity of TA NPs-DNA1 (10 μg/mL, n = 6) assembling with various ratio of FeMnOx-DNA2. Afterglow signal intensity was obtained with white light irradiation (10 mW/cm^2) time: 10 s and acquisition time: 60 s. Data are means ± SD.

30)*. Suppl Fig 23 Scheme the structure formed after programmed self-assembly is confusing. It is not clear from structure that APE site is from TA-NPs-DNA1 or FeOx-DNA2.*

Response: Thank you for your feedback regarding the clarity of the self-assembly structure depicted in **Supplementary Fig. 26** (previous *Suppl Fig 23*). In response to your comment, we have revised the figure to more clearly indicate the origin of the apurinic/apyrimidinic (AP) sites. In the updated figure, we have specifically annotated the AP sites to show that they are part of the DNA strands attached to the TA nanoparticles (TA-NPs-DNA1). The annotations now unambiguously highlight the AP sites within the schematic, ensuring that there is no confusion regarding their placement and origin in relation to the TA-NPs-DNA1 and FeO_x-DNA2 structures.

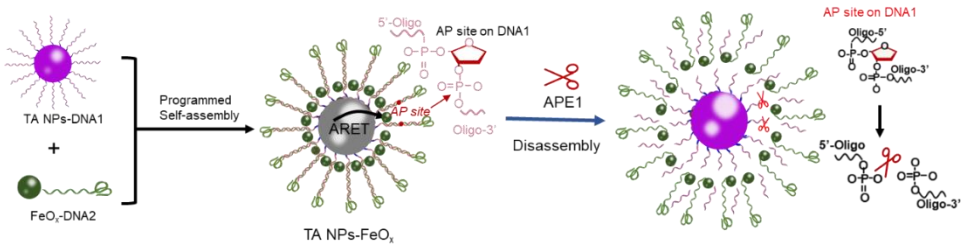

Supplementary Fig. 26 Schematic illustration for preparation and response process of APE1-activated TA NPs-FeO_x disassembly.

31)*. Results and discussion, line 244-247, What is basis of statement, is exp done or based on previous study ".. use of FeMnOx allows for an inverse change in contrast, facilitating the subtraction of the T1 MRI and T2 MRI intensity signal and providing larger dynamic ranges, compared to the use of iron oxide nanoparticles (FeOx)." Fig. 2a is scheme, however statement appears to stating result. " As a result, the sensitivity of the system was greatly enlarged, as depicted in Fig. 2a".*

Response: Thank you for your astute observation regarding the placement and basis of the statement in our manuscript. We acknowledge that the original phrasing may have inadvertently implied an assertion of results without providing immediate evidence within the text. To clarify:

The mentioned statement was indeed derived from experimental results and should be contextualized accordingly within the discussion of those findings. We have conducted a series of experiments comparing the contrast effects of $FeMnO_x$ and iron oxide nanoparticles (FeO_x) in MRI, which substantiate the claim about $FeMnO_x$'s capability to enable an inverse change in contrast and facilitate greater dynamic range in signal subtraction between T_1 and T_2 MRI modalities, as following.

We also compared the MRI contrast effect of FeO_x, commonly used as a T_1 contrast agent in MRI imaging studies. In this study, we utilized ultrasmall FeO_x nanoparticles (3.9 ±0.5 nm) as a control group to demonstrate the superior performance of $FeMnO_x$ in our designed system (**Supplementary Fig. 24**). We compared the MRI contrast effect of FeO_x to that of $FeMnO_x$ nanoparticles. As shown in **Supplementary Fig. 25**, FeO_x exhibited an increasing brightness in both T_1 and T_2 MRI images as the FeO_x concentration increased. We further explored the use of FeO_x as an MRI contrast agent in the synthesis of TA NPs- FeO_x, achieved by assembling FeO_x-DNA2 with TA NPs-DNA1, as illustrated in **Supplementary Fig. 15, 27**. Initially, TA NPs- FeO_x exhibited negative contrast in both T_1 and T_2 MRI models until activated by APE1. Following activation, TA NPs-FeO_x demonstrated positive imaging capability in both T_1 and T_2 MRI models (**Fig. 2m**). However, it is important to note that the MRI signal intensity increased simultaneously with increasing APE1 concentration (**Fig. 2n**), and thereby subtracting the T_1 MRI signal intensity from the T_2 MRI signal intensity (ΔT_1 - ΔT_2) would not expand the dynamic range of MRI, compared with that of TA NP-$FeMnO_x$ (**Fig. 2g**). Furthermore, the ΔT_1 - ΔT_2 values of TA NPs-FeO_x were not correlated with the concentration of APE1(**Fig. 2o**), suggesting that the ΔT_1 - ΔT_2 values of TA NPs-FeO_x cannot be used to quantify the concentration of APE1.

In light of this, we have revised the manuscript to relocate the statement to a section that directly follows the presentation of our experimental results. The revised text now reads:

"These experimental outcomes reveal that the utilization of $FeMnO_x$ contributes to an inverse variation in MRI contrast. This attribute is instrumental in the subtraction of T_1 and T_2 MRI intensity signals (**Fig. 2a**). The adoption of $FeMnO_x$ in the APE1-probe design enhances MRI contrast and dynamic range, expands detection limits, and increases the sensitivity for APE1 detection compared to probes using iron oxide nanoparticles (FeO_x) (**Fig. 2a**). Consequently, the APE1-probe delivers superior afterglow/MRI imaging performance in terms of both sensitivity and specificity, enabling effective monitoring of APE1 activity."

32)*. Suppl Fig 35, 36, statistical significance should be shown.*

Response: Thank you for your recommendation regarding the inclusion of statistical significance in Suppl Fig 35, 36. In response to your suggestion, we have now incorporated the statistical analysis into **Supplementary Fig. 43** and **Supplementary Fig.44** (previous Suppl Fig 35, 36). The p-values derived from appropriate statistical tests have been added to the figure caption to quantify the significance of the observed differences.

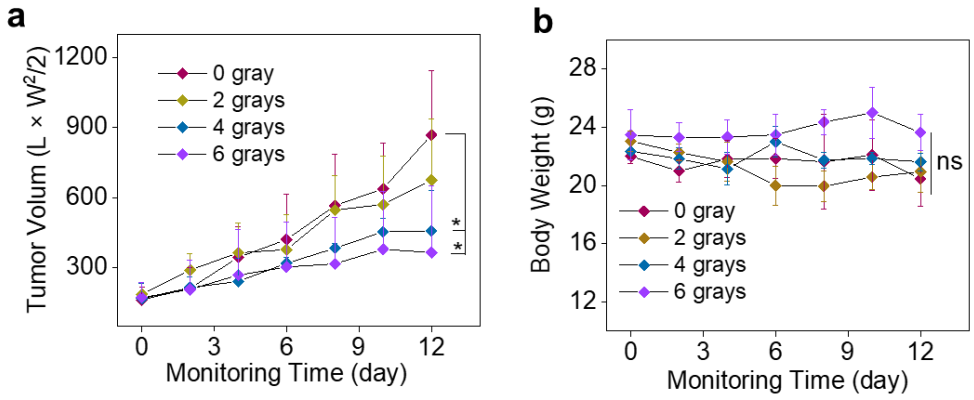

Supplementary Fig. 43 Radiotherapy for tumors of mice in vivo under various radiation intensities （n = 5). (a) Tumor growth curve. (b) Body weight. Data are means ± SD. Statistical differences were analyzed by student's t test, *p < 0.05, ns: no statistically significant difference.

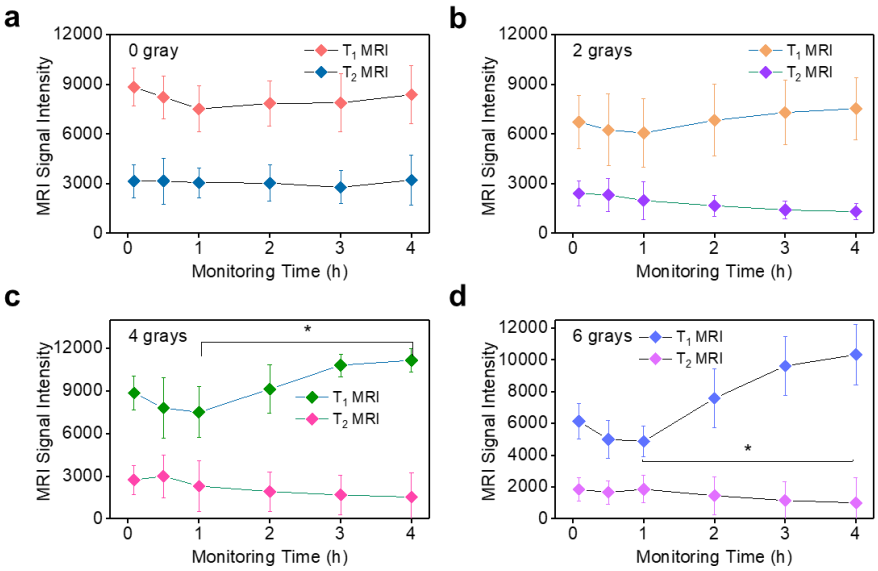

Supplementary Fig. 44 Quantified MRI signal intensity of the liver of mice after various radiation treatments and then intravenous injection of APE1-porbe (n = 3). (a) 0 gray treatments. (b) 2 grays treatments. (c) 4 grays treatments. (d) 6 grays treatments. Data are means ± SD. Statistical differences were analyzed by student's t test, *p < 0.05.

33). Line 529-530 and 569, the data shown Fig 5 is basically effect of radiation on afterglow effect and other parameters. Unless individual animals are monitored for these parameters and correlated with tumor growth and need of radiation dose needed, it is difficult to state its role in personalized dose description. It is too much claim!

Response: We appreciate your concern regarding the claims we made about the potential of our APE1-probe in personalized dose prescription based on the data presented in **Fig. 5.** Upon reflection, we agree that our initial assertion may have extended beyond the scope of the data we provided.

In response, we have carefully revised the manuscript to more accurately reflect the capabilities of the APE1-probe. We have removed references "to achieve personalized dose prescription, taking into account for individual differences and tumor heterogeneity." to ensure that our conclusions remain firmly grounded in the findings we have reported.

The updated manuscript now presents a more measured perspective on the implications of our research, focusing on the current evidence while acknowledging that further studies are necessary to fully realize the potential of the APE1-probe in individualized treatment planning.

In future studies, monitoring individual animals for these parameters and correlating them with APE1 levels, tumor growth, and the required radiation dose could refine the correlation between radiation dose and afterglow/MRI signal intensity. This approach would facilitate the determination of precise radiation doses for tailored treatment regimens, thereby enhancing the precision and efficiency of radiotherapy. By integrating MRI and afterglow imaging-guided diagnostics, this strategy promises to guide personalized radiotherapy dosage, accommodating individual variability and tumor heterogeneity.

34). Bystander effects are referred interaction from irradiated cells to neighboring cells. Since, in present study, effect was observed in distant tumors, which is systemic abscopal effect (Manuela et al, IJRB, Int J Radiat Biol. 2023;99(6):964-982. doi:

10.1080/09553002.2022.2078006). Hence, abscopal could be better terminology than bystander in the present manuscript. How much % of shielding was obtained compared to directly irradiated tumors.

Response: Thank you for pointing out the distinction between bystander and abscopal effects as it pertains to our study. We concur with your suggestion that "abscopal effect" is indeed the correct term to describe the systemic responses observed in non-irradiated tumors located at a distance from the irradiated site. We have updated our manuscript accordingly, replacing instances of "bystander effect" with "abscopal effect" to more accurately reflect the phenomena being described, in line with the reference you provided (*Int. J. Radiat. Biol.* **2023,** 99,964-982).

As for the quantification of shielding effectiveness, we used the imaging data obtained from MRI to calculate the differential in APE1 expression levels between irradiated and non-irradiated (shielded) tumors. Specifically, we analyzed the signal-to-noise ratios from MRI images **(Fig. 8i, j**) to assess the relative increase in APE1 levels. Our analysis revealed a significant increase in APE1 within the directly irradiated tumor (right tumor of Group 1, +X ray) when compared to its shielded counterpart (left tumor of Group 1, -X ray), indicating an effective systemic response. The percentage increase in APE1 expression in the irradiated tumor compared to the shielded tumor was 26.0 ± 8 %. In contrast, control tumors (both right and left tumors of Group 2, -X ray) showed no such increase, supporting the specificity of the observed abscopal effect.

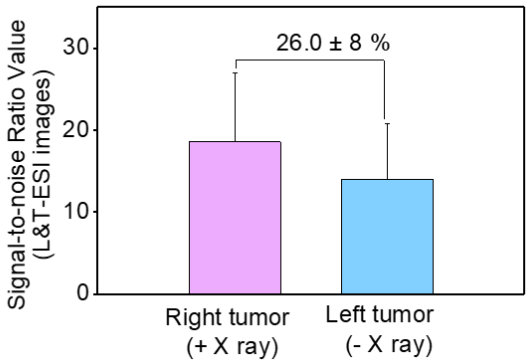

Fig. 8j. The analysis of shielding efficiency of the abscopal tumor compared to directly irradiated tumors (n = 3). Data are means ± SD.

35). In both tumor bearing legs after glow effect and its kinetics should be also monitored after radiation?

Response: Thank you for your suggestion regarding the monitoring of afterglow effects and kinetics in tumor-bearing legs after radiation treatment.

In response to your recommendation, we have conducted an experiment to examine the afterglow kinetics in both the irradiated and non-irradiated tumors of our mouse model. We used nude mice bearing subcutaneous HeLa tumors on both legs. We then selectively irradiated the right-leg tumor with a 6 grays dose of X-ray (right tumor, +X ray), while the left-leg tumor was protected from X-ray exposure (left tumor, -X ray). Two hours post-radiation, we injected the APE1-probe intravenously into the mice of Group 1 and performed afterglow imaging at multiple time points thereafter.

Upon analyzing the afterglow images, we noted a pronounced increase in the afterglow signal in the irradiated right-leg tumor, which was not observed in the non-irradiated left-leg tumor (**Supplementary Fig. 48**). This indicates that the afterglow effect correlates with the localized radiation exposure. Interestingly, we did not detect any significant change in afterglow signal in the legs themselves, suggesting that the afterglow effect is indeed tumor-specific under these experimental conditions.

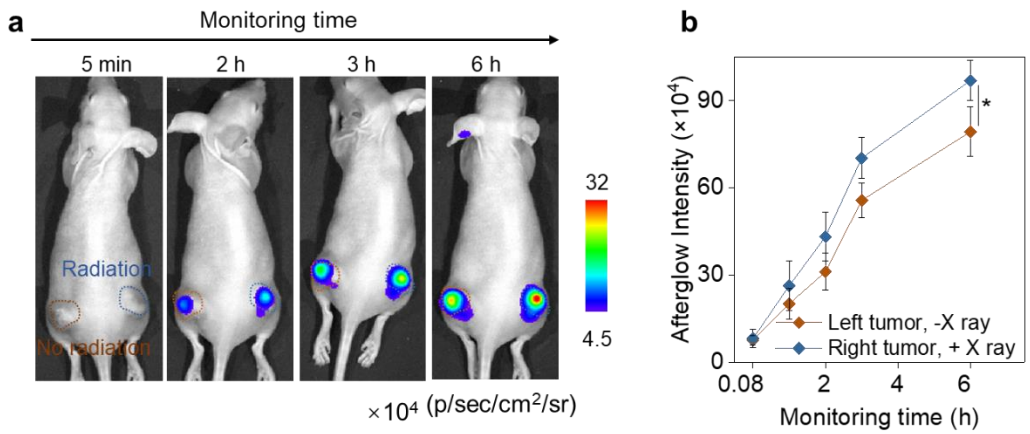

Supplementary Fig. 48 Afterglow imaging of the Group 1 mice with radiation treatment only in right tumor and then intravenous injection of APE1-probe (n = 3). (a) Afterglow images. (b) Quantification of afterglow signal intensity from (a). Afterglow imaging was obtained with light irradiation (10 mW/cm^2) of 10 s, acquisition time of 60 s. Data are means ± SD. Statistical differences were analyzed by student's t test, *p<0.05.

Related experimental methods:

APE1-probe for afterglow imaging of radiation-treated tumor and abscopal tumor. radiation-induced abscopal effect in vivo. We establish a subcutaneous xenograft dual-sided tumor model, 1 × 10^7 HeLa cells were inoculated on two sides of nude mice. The mice were then divided into two groups: Group 1 and Group 2. Group 1 consisted of mice with subcutaneous dual-sided Hela xenograft tumors, of which the right tumor was treated with 6 grays radiotion while the left tumor was shielded with a lead plate. After 2 hours, the mice received an intravenous injection of APE1-probe (150 μL, containing 80 μg/mL of TA NPs). Subsequently, afterglow imaging was recorded using an IVIS Spectrum imaging system (Lumina XR) with no excitation wavelength, 10 s of light irradiation (10 mW/cm^2), and 60 s of acquisition time at different time intervals.

36)*. Conclusions should be limited to observations made in the study. Most of the points like personalized medicine, biomarker etc are too tall claim with respect to observations made.*

Response: Thank you for your guidance. We understand the importance of ensuring that our conclusions are directly supported by the findings from our study. In light of your feedback, we have carefully revised the conclusions to more accurately reflect the observations made during our research. We have removed any assertions that could be perceived as overreaching beyond the scope of the empirical data. The revised conclusion focuses solely on the results obtained and their immediate implications, avoiding broader claims about personalized medicine and biomarker utility that are not explicitly substantiated by our current work. We hope that these adjustments address your concerns and improve the manuscript.

Reviewers' Comments:

Reviewer #1:
Remarks to the Author:
The authors have well addressed the concerns and thus I recommend its acceptance.
Minor comments: Supplementary table 3 should be carefully checked (there are some errors about the concentration, signal intensity, and the injection volume of TPP-DO), Besides, the authors forgot to provide the uncropped Western blot in the supplementary materials.

Reviewer #2:
Remarks to the Author:
All of my previous comments have been satisfactorily addressed, and therefore I am pleased to recommend publication in Nature Communication.

Reviewer #3:
Remarks to the Author:
Most of the comments have been addressed. But, still some comments/editorial corrections are required:
1. Since Gray is Unit of radiation absoorbed dose, it should be mentioned as "Gray" not as "gray or grays". The same should be corrected through the manuscript/Figures.
2. In previous comment no (34) How much % of shielding was obtained compared to directly irradiated tumors, is not mentioned. If you are getting effect in shielded tumorsm it is very impportant to mentioned that compared to directly irradiated how much dose shielded tumor received to understand that whether tumor shielded tumor received too high dose to show the effect. Physical dosimsters like TLD or ion chambers to both directly irradiated and shielded tumor at one typical dose is required.
3. Suppl Fig 48 b, quantification of directly irradited and shielded tumor showed marginal difference, however it is mentioned (line 72 Analysis of the afterglow images revealed a marked elevation") which should me mentioned as marginal increase.
4. How the synthesis of NPs and conjugation of bonds at different steps were characterized? Whether any method like FT-IRm, NMR etc is used?
5. Suppl Fig 28, after washing increase in after glow effect is explained due to decrease in background noise signal. Whether the value mentined are corrected value (background substracted)? If so the same should be mentioned in Fig legend
6. Line 723-725, "Additionally,
723 immunohistochemical fluorescence analysis corroborated a significant upregulation of APE1
724 expression in the irradiated tumor (Group 1, +X ray) in contrast to the non-irradiated tumor (Group
725 1, -X ray) (Supplementary Fig. 49)." This Fig could not be lacated in original suppl fig.
7. In Fig 8 j, the difference between + and - xray seems to be not signficant. Whether Fig i, j bring out some major conclusion? If not major conclusion, they may be removed.

Response Letter (NCOMMS-23-55361A)

Reviewer #1:

The authors have well addressed the concerns and thus I recommend its acceptance.

Minor comments: Supplementary table 3 should be carefully checked (there are some errors about the concentration, signal intensity, and the injection volume of TPP-DO), Besides, the authors forgot to provide the uncropped Western blot in the supplementary materials.

Response: Thank you for bringing this to our attention. We have rectified the information pertaining to TPP-DO in **Supplementary table 3.** Additionally, we have conducted a comprehensive review to ensure the accuracy of all other information. Related revisions have been highlighted within table

Organic afterglow particle	Excitation source	Minimum excitation powder density in solution	Maximum emission wavelength or range	Emission lifetime	Afterglow intensity in solution and in vivo imaging of subcutaneous tumor	References
TA NPs	White light source	60 μW/cm^2	640 nm	$t_{1/2}$ ≈600 s	In 1×NeBuffer: ~1.6× 10^6 (p/s/cm^2 /sr)/(5 μg/mL) with white light irradiation (10 mW/cm^2) of 10 s and acquisition time of 60 s; In vivo imaging: ~1× 10^6 (p/s/cm^2 /sr)/(80 μg/mL, 120 μL) with white light irradiation (10 mW/cm^2) of 10 s and acquisition time of 60 s	This work
P1–P5 polymers	365 nm UV light	20 mW/cm^2	508 nm	$t_{1/2}$ ≈869 ms	None	*J. Am. Chem. Soc.* **2023**, 145, 13, 7343–7351
MAS-pH/AL/Cu/GSH	660 nm laser	0.5-1.0 W/cm^2	510-570 nm	$t_{1/2}$ ≈30 s	In PBS buffer: ~8× 10^5 (p/s/cm^2/sr)/(50 μg/mL) with 660 nm laser irradiation (0.5 W/cm^2) of 30 s, and acquisition time of 10 s; In vivo imaging: ~ 10^4 (p/s/cm^2/sr)/(100 μg/mL, 25 μL) with 660 nm laser irradiation (1.0 W/cm^2) of 30 s, and acquisition time of 30 s	*J. Am. Chem. Soc.* **2023**, 145, 24386-24400
MAP-pH /$O_2^{\bullet-}$ /LAP	660 nm laser	0.8-1.0 W/cm^2	510-570 nm	$t_{1/2}$ ≈60 s	In PBS buffer: ~2-6× 10^5 (p/s/cm^2/sr)/(50 μg/mL) with 660 nm laser irradiation (0.8 W/cm^2) of 30 s and acquisition time of 30 s; In vivo imaging: ~4 ×10^5 (p/s/cm^2/sr)/((50 μg/mL, 25 μL) with a 660 nm laser irradiation (1.0 W/cm^2) of 30 s and acquisition time of 30 s	*J. Am. Chem. Soc.* **2023**, 145, 9, 5134–5144
Chlorin Nanoparticle	Halogen lamp, 808 nm laser	0.1 W/cm^2 or 1 W/cm^2	660-680 nm	$t_{1/2}$ ≈1.5 h	In PBS buffer: ~1.5 × 10^6 (p/s/cm^2/sr)/(50 μM) with Halogen lamp irradiation of 60 s and acquisition time of 10 s; In vivo imaging:~3×10^3 (p/s/cm^2/sr)/(25 μg/mL, 50 μL) with Halogen lamp irradiation of 60 s and acquisition time of 10 s.	*J. Am. Chem. Soc.* **2022**, 144, 15, 6719
P-TNP	White LED lamp, xenon lamp	2 W/ cm^2	630 nm	$t_{1/2}$ ≈120 s	In H_2O solution: ~800 (cps/mm^2)/(100 mg/mL) with white LED lamp irradiation (2 W/cm^2) of 60 s, and acquisition time of 60 s; In vivo imaging:~1.5×10^4 (p/s/cm^2/sr)/(0.1 mg/mL, 200 μL) with white LED lamp irradiation (2 W/cm^2) of 120 s, and acquisition time of 60 s	*Chem. Sci.*,**2020**, 11, 419
Nat. Commun.,**2020**, 11, 446	808 nm laser	1 W/cm^2	775 nm	$t_{1/2}$ ≈396 s	In PBS buffer: ~6×10^6 (p/s/cm^2/sr)/(58/28/2.2 μg/mL F12*(BF^{4-})$_2$/MEH-PPV/NIR775) with 808 nm laser irradiation (1W/cm^2) of 60 s, and acquisition time of 60 s; In vivo imaging: ~3×10^5 (p/s/cm^2/sr)/(211/100/8 μg F12*(BF^{4-})$_2$/MEH-PPV/NIR775, 200 μL) with 808 nm laser irradiation (1W/cm^2) of 60 s, and acquisition time of 60 s.	*Nat. Commun.*,**2020**, 11, 446
OSN1-T	365 nm UV light	10 mW/cm^2	530 nm and 570 nm	$t_{1/2}$ ≈10s	In PBS buffer: ~6×10^{10} (p/s/cm^2/sr)/(1.6 μM) with handheld UV lamp irradiation (12 W) of 60 s, and acquisition time of 10 s; In vivo imaging:~1.5×10^4 (p/s/cm^2/sr)/(16 μM)with UV light irradiation (18 mW/cm^2) of 60 s, and acquisition time of 10 s	*Adv. Mater.* **2017,** 29, 1606665
SPN-NCBS; SPN-thiol	808 nm laser	1 W/cm^2	780 nm	$t_{1/2}$ ≈396 s	In water: ~1×10^6 (p/s/cm^2/sr)/(1.25 μg/mL) with 808 nm laser irradiation (1 W/cm^2) of 60 s, and acquisition time of 30 s; In vivo imaging:~5.7×10^5 (p/s/cm^2/sr)/(μg/mL), 0.25 mg/mL, 2 μL) with 808 nm laser irradiation (0.5 W/cm^2) of 60 s, and acquisition time of 180 s	*Nat. Biotechnol.* **2017**, 35, 1102-1110
APtN	808 nm laser	0.25 W/cm^2	550 nm	$t_{1/2}$ ≈960 s	In PBS buffer: ~1.5×10^6 (p/s/cm^2/sr)/(1 mg/mL) with 808 nm laser irradiation (0.25 W/cm^2) of 10 s, and acquisition time of 60 s; In vivo imaging:~1.5×10^4 (p/s/cm^2/sr)/(400 μg/mL, 200 μL) with 808 nm laser irradiation (0.25 W/cm^2) of 20 s, and acquisition time of 60 s	*Adv. Mater.* **2019,** 31, 1902672
mTPA-N	365 nm UV light	95 mW/cm^2	515 – 640 nm	$t_{1/2}$ ≈13 ms	In aqueous solution: ~7×10^4 (p/s/cm^2/sr)/(300 μg/mL) with UV irradiation (95 mW/cm^2) of 5 s and exposure time of 5 s; In vivo imaging:~9×10^5 (p/s/cm^2/sr)/(600 μg/mL, 50 μL) with UV irradiation (95 mW/cm^2) of 5 s, and exposure time of 5 s	*Adv. Mater.* **2020,** 32, 2006752
Q-SNAP	Ultrasound	1.5 W/cm^2	780 nm	$t_{1/2}$ ≈ 90 s	In PBS buffer:~2×10^6 (p/s/cm^2/sr)/(10 μg/mL) with ultrasound irradiation (1.5 W/cm^2) of 30 s, and acquisition time of 1 s; In vivo imaging: ~7×10^4 (p/s/cm^2/sr)/(2 mg/kg mice) with ultrasound irradiation (1.5 W/cm^2) of 30 s and acquisition time of 10 s	*Adv. Mater.* **2023**, *35*, 2211651
TPP-DO	Halogen lamp	50 mW/cm^2	650 nm	$t_{1/2}$ ≈120 s	In PBS buffer;~4.0×10^8 (p/s/cm^2/sr)/(25 μM) with halogen lamp irradiation (50 mW/cm^2) of 10 s, and acquisition time of 5 s; In vivo imaging: ~4.0×10^6 (p/s/cm^2/sr)/(200 μg/mL, 200 μL) with halogen lamp irradiation (50 mW/cm^2) of 10 s, and acquisition time of 10 s for;	*Angew. Chem. Int. Ed.* **2024,** 63, e202313117

Supplementary table 3 Luminescence characterization comparison of reported organic afterglow materials.

Moreover, we have provided the uncropped images of Western blot for **supplementary Fig. 34,** as the original data to support Fig.3n.

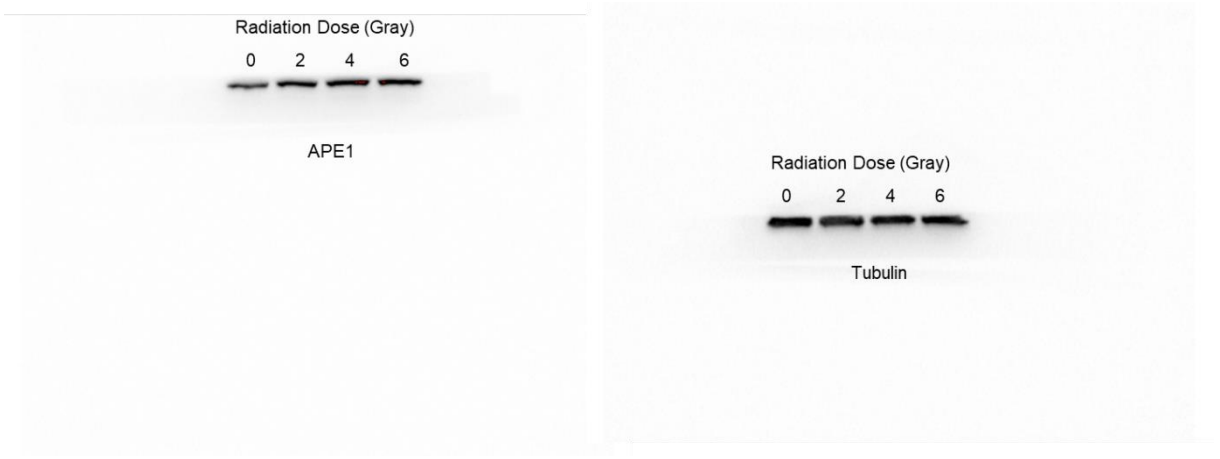

Supplementary Fig. 34 Uncropped Western bolting images for APE1 level of the HeLa cells at post-treatment of 2 hours under various radiation doses (n = 2).

Reviewer #3:

Most of the comments have been addressed. But, still some comments/editorial corrections are required:

***1**. Since Gray is Unit of radiation absorbed dose, it should be mentioned as "Gray" not as "gray or grays". The same should be corrected through the manuscript/Figures.*

Response: We appreciate your guidance in clarifying the proper unit of measurement for radiation dose, which is Gray. We have made the required revisions in our manuscript and figures, substituting "gray or grays" with "Gray" to ensure greater accuracy. The corrected instances have been highlighted for your convenience.

***2**. In previous comment no (34) How much % of shielding was obtained compared to directly irradiated tumors, is not mentioned. If you are getting effect in shielded tumors it is very important to mentioned that compared to directly irradiated how much dose shielded tumor received to understand that whether tumor shielded tumor received too high dose to show the effect. Physical dosimsters like TLD or ion chambers to both directly irradiated and shielded tumor at one typical dose is required.*

Response: We appreciate your suggestion regarding comparison of the shielding effect on tumors with and without direct radiation. We measured the shielding efficiency to be nearly 100 % for the lead plate (thickness = 1 cm) against X-ray radiation of 6 Gray, based on the dosimeter.

***3**. Suppl Fig 48 b, quantification of directly irradiated and shielded tumor showed marginal difference, however it is mentioned (line 72 Analysis of the afterglow images revealed a marked elevation") which should me mentioned as marginal increase.*

Response: We greatly appreciate your precise description of the "marginal increase" observed in the afterglow signal difference between directly irradiated and shielded tumors, as it aligns perfectly with our intended expression. We have made the necessary adjustments in our manuscript, substituting "marked elevation" with "marginal increase" to more accurately portray the phenomenon being discussed. The corrected instances have been highlighted in line 72.

***4**. How the synthesis of NPs and conjugation of bonds at different steps were characterized? Whether any method like FT-IRm, NMR etc is used?*

Response: Thanks for your inquiry about the synthesis of NPs and characterization of bond conjugation at different stages. We employed a diverse range of techniques to ensure the successful execution of each step in the nanoparticle synthesis and subsequent bond conjugation.

We characterized the $FeMnO_x$-OA and their conjugation with NH_2-BHQ_3/PEG-N_3 for $FeMnO_x$@BHQ-N_3 using FT-IR spectra analysis. According to **supplementary Figure 14c**, R-N=N=N stretching vibration at 2116 cm^{-1}, N-H stretching vibration at 1105 cm^{-1}, and aromatic C-H bending vibration at 960-690 cm^{-1} indicated a successful conjugation of H_2N-BHQ_3 with $FeMnO_x$ for $FeMnO_x$@BHQ-N_3.

Supplementary Fig. 14c

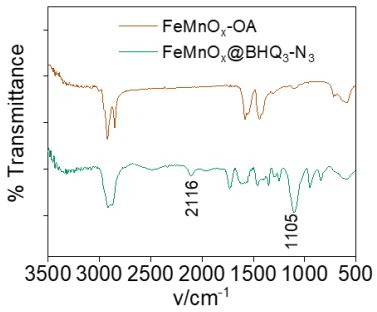

Supplementary Figure 14c the FT-IR spectra of $FeMnO_x$-OA and $FeMnO_x$@BHQ-N_3.

We further determined the relaxation time of $FeMnO_x$ before and after conjugating with TA NPs using NMR analysis. According to **Supplementary Fig. 22a and 22b**, after conjugating with TA NPs, the relaxation time of $FeMnO_x$, both T_1 and T_2 were increased, suggesting the successful assembly between $FeMnO_x$ and TA NPs.

Supplementary Fig. 22a

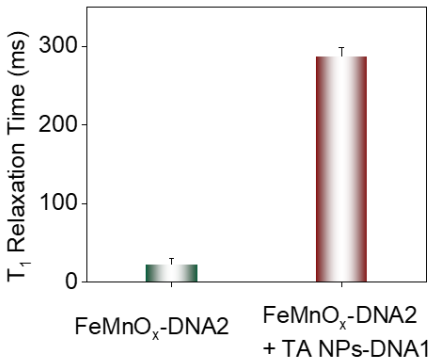

Supplementary Fig. 22b

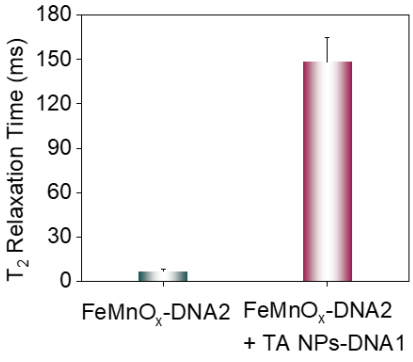

Supplementary Figure 22a T_1 relaxation time of $FeMnO_x$ before and after conjugating with TA NPs. **Supplementary Figure 22b** T_2 relaxation time of $FeMnO_x$ before and after conjugating with TA NPs.

In previous characterization, we synthesized afterglow nanoparticles (TA NPs) through one-step nanoprecipitation (**Fig. 1a**), and the as-prepared TA NPs had a mean diameter of 34 ± 8 nm, as determined by transmission electron microscopy (TEM) images (**Fig. 1b**). The average hydrodynamic size of TA NPs in water was measured to be 37.6 ± 3.1 nm with zeta potential of -18 ± 0.8 mV (**Supplementary Fig. 2**).

Fig. 1a

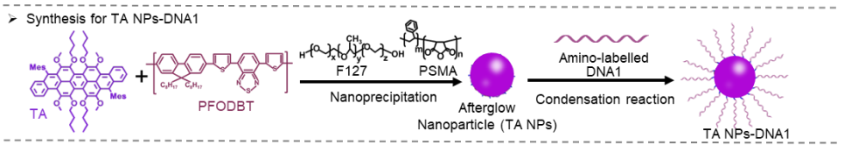

Fig. 1b

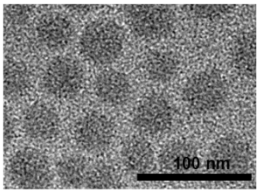

Supplementary Fig. 2a

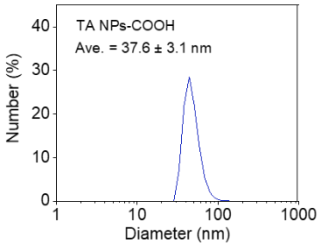

Supplementary Fig. 2b

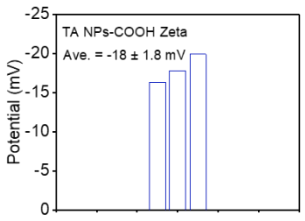

Fig.1a Schematic illustration for preparation of afterglow nanoparticles (TA NPs). **Fig.1b** TEM images of TA NPs. **Supplementary Fig. 2a** DLS measurement at water condition of TA NPs. **Supplementary Fig. 2b** Zeta potential of TA NPs. Data are means ± SD.

Next, we modified TA NPs with amino-labeled DNA1 through a cross-linking reaction involving amino and carboxyl groups (**Fig. 1a**). The successful preparation of TA NPs-DNA1 was confirmed by the enhanced absorption intensity of DNA1 at 260 nm compared to free TA NPs-COOH (**Supplementary Fig. 10**). Additionally, the dynamic light scattering (DLS) analysis revealed an increase in the diameter to 49.1 nm ± 3.7 nm with zeta potential of -25.2 ± 2.3 mV (**Supplementary Fig. 11**).

Supplementary Fig. 10

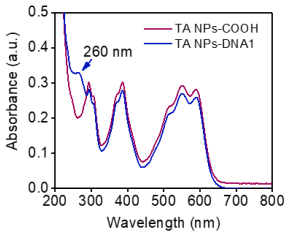

Supplementary Fig. 11a

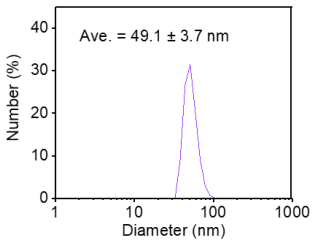

Supplementary Fig. 11b

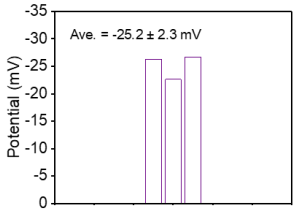

Supplementary Fig. 10 Absorption spectra of TA NPs before and after conjugating with DNA1. **Supplementary Fig. 11a** Characterization of (a) DLS measurement at water condition of TA NPs-DNA1. (Insert: photograph image). **Supplementary Fig. 11b** Zeta potential of TA NPs-DNA1. Data are means ± SD.

Ultrasmall $FeMnO_x$ was prepared through thermal decomposition using iron-eructate and manganese-oleate. The TEM images revealed that the as-synthesized $FeMnO_x$ had a mean diameter of 3.4 ± 0.9 nm (**Fig. 1i**). Subsequently, FeMnOx was modified with phosphorylated/azide-polyethylene glycol (p-PEG-N_3) and 2-bromo-2-methylpropanoic acid (BMPA) through a ligand exchange process to yield $FeMnO_x$-N_3, which was further modified with amino-modified BHQ_3 quencher molecules (H_2N-BHQ_3) to form FeMnOx@BHQ_3-N_3 (**Fig. 1a**). The successful preparation resulted in the transformation of hydrophobic $FeMnO_x$ (yellow color) into hydrophilic $FeMnO_x$@BHQ-N_3 (green color) (**Supplementary Fig. 14**). FeMnOx@BHQ_3-N_3 exhibited noticeable absorbance of BHQ_3 at the wavelength of 600 nm, with an average hydrodynamic diameter of 9.6 ± 0.8 nm and a potential of -14 ± 0.2 mV.

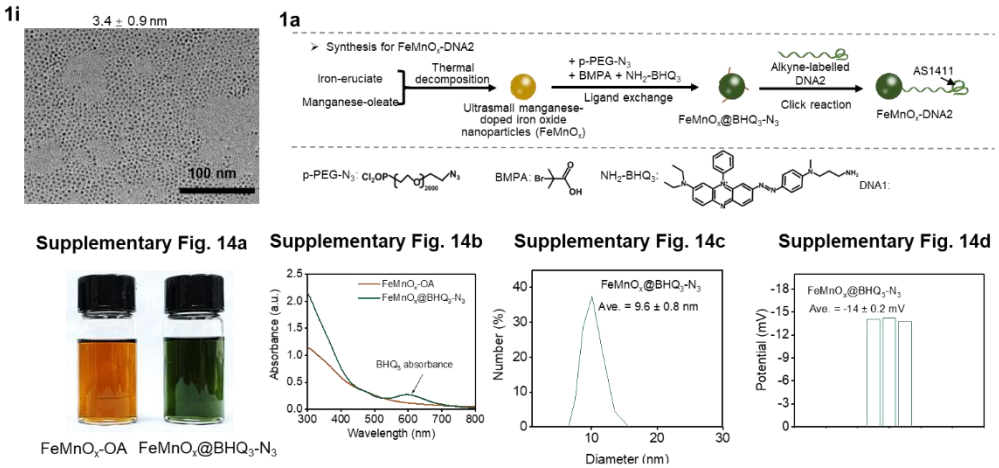

Fig. 1i TEM images of $FeMnO_x$. **Fig.1a** Schematic illustration for preparation of $FeMnO_x$-DNA2. **Supplementary Fig. 14a** Photographs images of $FeMnO_x$ (containing (0.31 mg/mL, Fe + Mn) before and after conjugating with NH_2-BHQ_3 and p-PEG-N_3. **Supplementary Fig. 14b** Absorbance spectra of FeMnOx and $FeMnO_x$@BHQ_3-N_3. **Supplementary Fig. 14c** DLS measurement of $FeMnO_x$@BHQ_3-N_3 at water condition. **Supplementary Fig. 14d** Zeta potential of FeMnOx@BHQ_3-N_3. Data are means ± SD.

Subsequently, $FeMnO_x$@BHQ_3-N_3 was conjugated with alkyne-labeled DNA2 (alkyne-DNA2) through the click reaction, resulting in the formation of DNA2-functionalized $FeMnO_x$@BHQ_3-N_3 ($FeMnO_x$-DNA2) (**Fig. 1a**). The successful preparation of $FeMnO_x$-DNA2 was confirmed by an increase in the DLS size to 12.9 ± 1.1 nm and a decrease in zeta potential to -16.1 ± 1.4 mV (**Supplementary Fig. 15**).

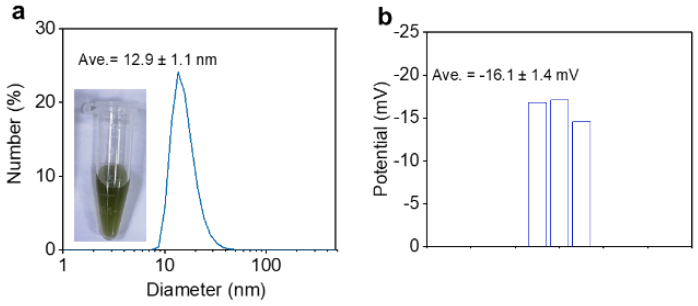

Supplementary Figure 15. Characterization of $FeMnO_x$ conjugation with DNA2 ($FeMnO_x$-DNA2). (a) DLS measurement (Insert: photograph images, 0.25 mg/mL, Fe + Mn). (b) Zeta potential. Data are means ± SD.

Based on the hybridization of DNA1 and DNA2, we assembled TA NPs-DNA1 with $FeMnO_x$-DNA2 to form the core-satellite assembly of TA NPs and $FeMnO_x$, named APE1-probe (**Fig. 1a and Supplementary Fig. 16**). The successful preparation of APE1-probe was verified through TEM images, which revealed a core-satellite structure where afterglow NPs served as the core and multiple $FeMnO_x$ acted as satellites attached closely to the surface of TA NPs (**Fig. 1l**). The DLS analysis determined an average diameter of 83.0 ± 7.2 nm and a potential of -37 ± 2.6 mV (**Supplementary Fig. 17**). All characterization *at different steps were verified the successful synthesis of NPs and conjugation of bonds.*

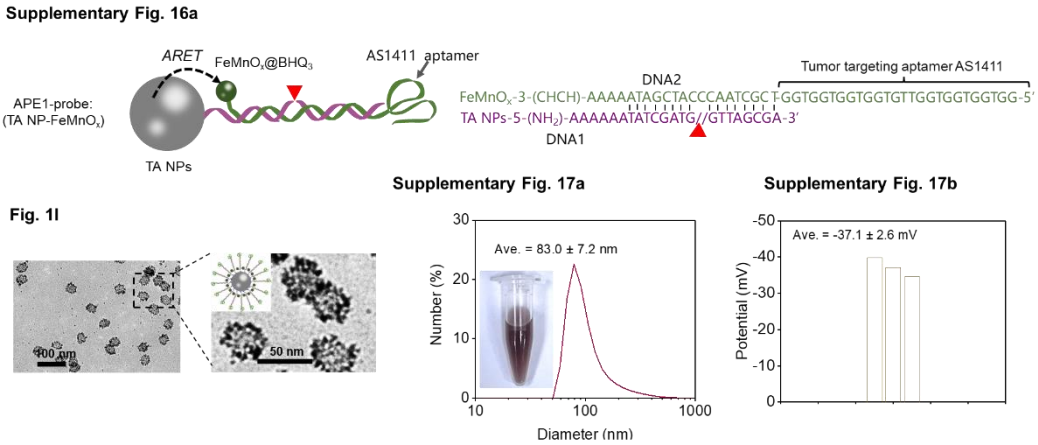

Supplementary Fig. 16a Schematic illustration for the structures and DNA sequence of TA NP-$FeMnO_x$ (APE1-probe). **Fig. 1l** TEM images of TA NPs-$FeMnO_x$ assembly (APE1-probe). **Supplementary Fig. 17a** DLS measurement of TA NPs-DNA1 and $FeMnO_x$-DNA2 assembly (APE1-probe) (Insert: photograph image, containing 50 μg/mL TA NPs) in DPBS (n = 3). **Supplementary Fig. 17b** Zeta potential of APE1-probe (n = 3). Data are means ± SD.

5. *Suppl Fig 28, after washing increase in afterglow effect is explained due to decrease in background noise signal. Whether the value mentioned are corrected value (background substracted)? If so, the same should be mentioned in Fig legend*

Response: In response to the reviewer's comment regarding Supplementary Fig. 29 (previous Supplementary Fig. 28), we acknowledge the observation that the increase in afterglow effect post-washing is attributed to the reduction in background noise. Indeed, the signals presented are corrected values, with the background noise subtracted. We have explicitly mentioned and clarified this aspect in the figure legends to ensure transparency and accuracy in the data interpretation.

Supplementary Fig. 29. Afterglow imaging comparison of APE1-probe-incubated HeLa cells before and after washing. HeLa cells were treated with radiation (6 Gray). After 2 hours, those treated cells were incubated with APE1-probe for 4 hours. The cells were collected after DPBS washing for afterglow imaging (10 mW/cm^2, irradiation time: 10 s, acquisition time: 60 s, n = 4). The cells were collected without DPBS washing for afterglow imaging was used as the controls. The signals presented are corrected values. Data are means ± SD.

6. *Line 723-725, "Additionally,*
723 immunohistochemical fluorescence analysis corroborated a significant upregulation of APE1
724 expression in the irradiated tumor (Group 1, +X ray) in contrast to the non-irradiated tumor (Group
725 1, -X ray) (Supplementary Fig. 49)." This Fig could not be located in original suppl fig.

Response: We highly appreciate your meticulous attention to detail and apologize for the unclear marking regarding APE1 expression information. Following you, we have now added the pertinent information regarding APE1 expression in the immunohistochemical fluorescence images and highlighted it in *Supplementary Fig. 51 (previous Supplementary Fig. 49)*.

Supplementary Fig. 51

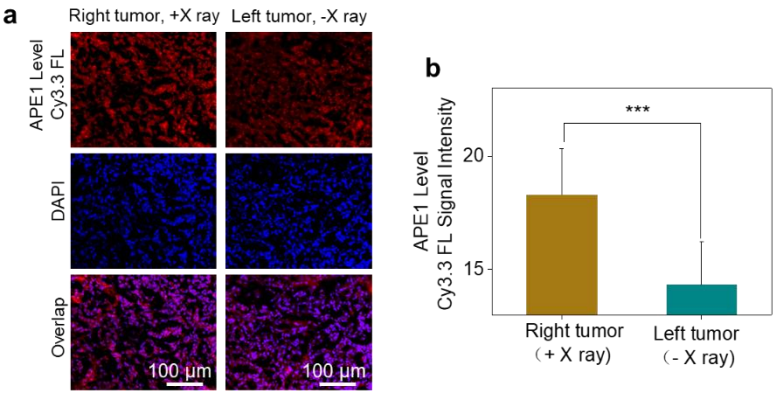

Supplementary Fig. 51 Fluorescence confocal images and signal intensity for immunofluorescence of tumors slice from the Group 1 mice with radiation treatment (6 Gray) only in the right tumor while no radiation by incubating with anti-APE antibody and Cy3-labeled IgG for testing APE1 level treatment in left tumor (n = 3 slice × 10). (a) Fluorescence confocal images. (b) Mean fluorescence signal intensity. Data are means ± SD. Statistical differences were analyzed by student's t test, *p<0.001.

7. *In Fig 8 j, the difference between + and – x ray seems to be not signficant. Whether Fig i, j bring out some major conclusion? If not major conclusion, they may be removed it.*

Response: The significant difference between the positive and negative X-ray images presented in Figure 8j serves as a crucial conclusion. It indicated that MRI subtraction by longitudinally and transversely subtracting the T_1 and T_2 MRI images can efficiently remove background signal interference, resulting in a substantial enhancement of MRI contrast between the radiation-treated tumor and the untreated tumors, which lead to a significant improvement in signal-to-noise ratio (tumor to normal tissue).

Reviewers' Comments:

Reviewer #1:
Remarks to the Author:
The authors have well addressed the concerns and thus I recommend its acceptance.

Reviewer #3:
Remarks to the Author:
2. In previous comment no (34) How much % of shielding was obtained compared to directly irradiated tumors, is not mentioned. If you are getting effect in shielded tumors it is very important to mentioned that compared to directly irradiated how much dose shielded tumor received to understand that whether tumor shielded tumor received too high dose to show the effect. Physical dosimsters like TLD or ion chambers to both directly irradiated and shielded tumor at one typical dose is required.
Response: We appreciate your suggestion regarding comparison of the shielding effect on tumors with and without direct radiation. We measured the shielding efficiency to be nearly 100 % for the lead plate (thickness = 1 cm) against X-ray radiation of 6 Gray, based on the dosimeter.

Further comment: Mention the shielding and thickness of lead in materials and methods

5. Suppl Fig 28, after washing increase in afterglow effect is explained due to decrease in background noise signal. Whether the value mentioned are corrected value (background substracted)? If so, the same should be mentioned in Fig legend
Response: In response to the reviewer's comment regarding Supplementary Fig. 29 (previous Supplementary Fig. 28), we acknowledge the observation that the increase in afterglow effect post-washing is attributed to the reduction in background noise. Indeed, the signals presented are corrected values, with the background noise subtracted. We have explicitly mentioned and clarified this aspect in the figure legends to ensure transparency and accuracy in the data interpretation.

Further comment: In Figure legend, instead of corrected value clearly mention how correction was done (as there are mupltiple ways corrections can be done) i.e. substarction of background.

REVIEWER COMMENTS

Reviewer #1 (Remarks to the Author):

The authors have well addressed the concerns and thus I recommend its acceptance.

Reviewer #3 (Remarks to the Author):

2. In previous comment no (34) How much % of shielding was obtained compared to directly irradiated tumors, is not mentioned. If you are getting effect in shielded tumors it is very important to mentioned that compared to directly irradiated how much dose shielded tumor received to understand that whether tumor shielded tumor received too high dose to show the effect. Physical dosimsters like TLD or ion chambers to both directly irradiated and shielded tumor at one typical dose is required.

Response: We appreciate your suggestion regarding comparison of the shielding effect on tumors with and without direct radiation. We measured the shielding efficiency to be nearly 100 % for the lead plate (thickness = 1 cm) against X-ray radiation of 6 Gray, based on the dosimeter.

Further comment: Mention the shielding and thickness of lead in materials and methods.

Response: We thank you for your suggestion. We have provided the relevant information about shielding and the thickness of lead in materials and methods.

5. Suppl Fig 28, after washing increase in afterglow effect is explained due to decrease in background noise signal. Whether the value mentioned are corrected value (background substracted)? If so, the same should be mentioned in Fig legend

Response: In response to the reviewer's comment regarding Supplementary Fig. 29 (previous Supplementary Fig. 28), we acknowledge the observation that the increase in afterglow effect post-washing is attributed to the reduction in background noise. Indeed, the signals presented are corrected values, with the background noise subtracted. We have explicitly mentioned and clarified this aspect in the figure legends to ensure transparency and accuracy in the data interpretation.

Further comment: In Figure legend, instead of corrected value clearly mention how correction was done (as there are mupltiple ways corrections can be done) i.e. substarction of background.

Response: We thank you for your suggestion. We have mentioned whether the cell was washed or not before the afterglow measurement in the corresponding legends.